UNIVERSIDADE FEDERAL DO RIO DE JANEIRO

INSTITUTO DE FÍSICA

Superconducting properties of some strongly correlated fermionic systems

Rodrigo Alves Fontenele

Rio de Janeiro

May 2025

UNIVERSIDADE FEDERAL DO RIO DE JANEIRO

INSTITUTO DE FÍSICA

Superconducting properties of some strongly correlated fermionic systems

Rodrigo Alves Fontenele

Presenting this Ph.D. thesis to the Postgraduate Program in Physics at the Physics Institute of the Federal University of Rio de Janeiro (UFRJ) fulfills the necessary requirements for obtaining the title of Doctor of Science (Physics).

Advisor: Raimundo Rocha dos Santos

Co-Advisor: Natanael de Carvalho Costa

Rio de Janeiro

May 2025

Superconducting properties of some strongly correlated fermionic systems

Rodrigo Alves Fontenele

Advisor: Raimundo Rocha dos Santos

Co-Advisor: Natanael de Carvalho Costa

Tese de Doutorado submetida ao Programa de Pós-Graduação em Física, Instituto de Física, da Universidade Federal do Rio de Janeiro – UFRJ, como parte dos requisitos necessários à obtenção do título de Doutor em Ciências (Física).

Aprovada por:

Prof. Dr. Raimundo Rocha dos Santos, IF-UFRJ
(Presidente e Orientador)

Prof. Dr. Natanael de Carvalho Costa, IF-UFRJ
(Coorientador)

Prof. Dr. Marcello Barbosa da Silva Neto, IF-UFRJ

Prof. Dra. Maria Carolina de Oliveira Aguiar, UFMG

Prof. Dr. Hermann Freire Ferreira Lima e Silva, UFG

Prof. Dr. Fernando Iemini de Rezende Aguiar, UFF

Rio de Janeiro, RJ – Brasil

Maio de 2025

CIP - Catalogação na Publicação

A683s

Alves Fontenele, Rodrigo
Superconducting properties of some strongly correlated fermionic systems / Rodrigo Alves Fontenele. -- Rio de Janeiro, 2025.
163 f.

Orientador: Raimundo Rocha dos Santos.
Coorientador: Natanael de Carvalho Costa.
Tese (doutorado) - Universidade Federal do Rio de Janeiro, Instituto de Física, Programa de Pós Graduação em Física, 2025.

1. Supercondutividade. 2. modelo de Hubbard atrativo. 3. Monte Carlo Quântico. 4. modelo de Holstein. 5. acoplamento spin-orbita Rashba. I. Rocha dos Santos, Raimundo , orient. II. de Carvalho Costa, Natanael, coorient. III. Título.

Elaborado pelo Sistema de Geração Automática da UFRJ com os dados fornecidos pelo(a) autor(a), sob a responsabilidade de Miguel Romeu Amorim Neto - CRB-7/6283.

Resumo

Superconducting properties of some strongly correlated fermionic systems

Rodrigo Alves Fontenele

Advisor: Raimundo Rocha dos Santos

Co-Advisor: Natanael de Carvalho Costa

Resumo da Tese de Doutorado apresentada ao Programa de Pós-Graduação em Física do Instituto de Física da Universidade Federal do Rio de Janeiro - UFRJ, como parte dos requisitos necessários à obtenção do título de Doutor em Ciências (Física).

Ao longo desta tese, investigamos as propriedades de alguns sistemas fermiônicos fortemente correlacionados, com foco nas transições de fase supercondutoras e na ordenação de carga. Em vista dos recentes experimentos com átomos fermiônicos ultrafrios em redes óticas, que renovaram o interesse no estudo do modelo de Hubbard atrativo (AHM), realizamos extensivos estudos livres do problema do sinal utilizando o método de Monte Carlo Quântico Determinantal (DQMC) para este modelo em uma rede quadrada. Obtivemos um diagrama de fases detalhado para a temperatura crítica supercondutora, T_c, em função do preenchimento da banda, $\langle n \rangle$, e da intensidade da interação atrativa, U, a partir do qual identificamos uma região relativamente ampla $|U|/t \approx 5 \pm 1$ (t é a amplitude de hopping) e $\langle n \rangle \approx 0.79 \pm 0.09$, levando a um máximo de $T_c \approx 0.16t$. Destacamos ainda duas escalas adicionais de temperatura: a de formação de pares, T_p, e a de degenerescência, T_d. A primeira define a escala de formação dos pares (acreditando-se estar intimamente relacionada à escala da abertura de gap para excitações de spin nos cupratos), enquanto

a segunda estabelece a escala dos efeitos quânticos dominantes.

Nossos dados de DQMC para a distribuição de sítios duplamente ocupados, para a função de distribuição de momento e para o peso de quase-partícula exibem características distintas em ambos os lados do cruzamento BCS-BEC, além de sugerirem um possível cruzamento subjacente entre comportamentos de líquido de Fermi e não-Fermi. No entanto, as temperaturas críticas supercondutoras (ou superfluidas), T_c, ainda são um pouco menores do que as menores temperaturas alcançadas nos experimentos. Assim, analisamos como a supercondutividade pode ser aprimorada por empilhamento, estudando geometrias de bicamada e de rede cúbica tridimensional para identificar as condições sob as quais T_c pode aumentar. Descobrimos que, com uma escolha adequada do preenchimento e da intensidade da atração local, um bicamada pode apresentar valores de T_c entre 1.5 e 1.7 vezes superiores aos da monocamada; já para a rede cúbica simples, o aumento pode ser até 30% maior do que o máximo observado na monocamada.

Também verificamos a precisão de uma estimativa do tipo BCS para T_c no modelo de Hubbard atrativo, bem como de um limite superior para T_c baseado no peso superfluido. Além disso, avaliamos o papel do hopping de segundos vizinhos, t', no ajuste da densidade de estados no nível de Fermi, o que afeta as propriedades supercondutoras. Nossos resultados indicam que uma escolha criteriosa de t' pode aumentar T_c em até 50% em comparação com o caso em que há apenas hopping de primeiros vizinhos. Em contrapartida, T_p diminui com o aumento de $|t'/t|$, o que deve representar uma redução da região de pseudogap, favorecendo um comportamento mais próximo ao BCS no regime de acoplamento intermediário. Analisamos ainda a densidade de estados interagente para caracterizar a transição de um regime de pseudogap para um estado supercondutor com um *gap* completamente aberto. Esses achados sugerem que o hopping para segundos vizinhos pode ser uma rota viável para aumentar T_c a valores mais próximos das escalas de temperatura acessíveis experimentalmente.

Por fim, investigamos o impacto do acoplamento spin-órbita Rashba nas fases de or-

denamento de carga em um modelo tipo Holstein em uma rede quadrada em banda semi-preenchida, utilizando a teoria de campo médio, teoria de perturbação em clusters e o método DQMC. Como resultado, mostramos que a fase de onda de densidade de carga no estado fundamental não é destruída conforme o parâmetro de acoplamento spin-órbita de Rashba, α, aumenta. Além disso, no regime de acoplamento spin-órbita puro, onde o termo de hopping está ausente, encontramos um diagrama de fases rico, apresentando um estado de semicondutor para baixos valores do acoplamento elétron-fônon e uma consequente transição para estados de onda de densidade de carga em altas intensidades desse acoplamento. Além disso, identificamos a coexistência de estados supercondutores e de onda de densidade de carga para altas frequências de fônon.

Palavras-chave: Supercondutividade, modelo de Hubbard atrativo, Monte Carlo Quântico, modelo de Holstein, acoplamento spin-orbita Rashba.

Abstract

Superconducting properties of some strongly correlated fermionic systems

Rodrigo Alves Fontenele

Advisor: Raimundo Rocha dos Santos

Co-Advisor: Natanael de Carvalho Costa

Abstract da Tese de Doutorado apresentada ao Programa de Pós-Graduação em Física do Instituto de Física da Universidade Federal do Rio de Janeiro - UFRJ, como parte dos requisitos necessários à obtenção do título de Doutor em Ciências (Física).

Throughout this thesis, we investigate the properties of some strongly correlated fermionic systems, focusing on the superconducting phase transitions and Charge ordering. In view of recent experiments with ultracold fermionic atoms in optical lattices, which have renewed interest in the study of the attractive Hubbard model (AHM), we have performed an extensive minus-sign–free Determinant Quantum Monte Carlo (DQMC) studies of this model on a square lattice. We have obtained a detailed phase diagram for the critical superconducting temperature, T_c, in terms of the band filling, $\langle n \rangle$, and interaction strength, U, from which we pinpoint a somewhat wide region $|U|/t \approx 5 \pm 1$ (t is the hopping amplitude) and $\langle n \rangle \approx 0.79 \pm 0.09$ leading to a maximum $T_c \approx 0.16t$. Two additional temperature scales, namely pairing, T_p, and degeneracy, T_d, have been highlighted: the former sets the scale for pair formation (believed to be closely related to the scale for the gap of spin excitations in cuprates), while the latter sets the scale for dominant quantum effects. Our DQMC data for the distribution of doubly occupied sites, for the momentum

distribution function, and for the quasiparticle weight show distinctive features on both sides of the BCS-BEC crossover, being also suggestive of an underlying crossover between Fermi- and non-Fermi liquid behaviors. However, the superconducting (superfluid) critical temperatures T_c's are still somewhat smaller than the lowest temperatures achieved in experiments. We then analyze how superconductivity can be enhanced by layering, studying bilayer and three-dimensional cubic lattice geometries to identify conditions under which T_c increases. We have found that by a judicious choice of fillings and intensity of on-site attraction, a bilayer can exhibit T_c's between 1.5 and 1.7 times those of the single layer; for the simple-cubic lattice the enhancement can be 30% larger than the maximum for the single layer. We also check the accuracy of both a BCS-like estimate for T_c in the attractive Hubbard model as well as of an upper bound for T_c based on the superfluid density. Additionally, we assess the role of next-nearest neighbor hopping, t', in tuning the density of states at the Fermi level, which affects superconducting properties. Our results show that a judicious choice of t' can increase T_c by up to 50% compared to the case with only nearest-neighbor hopping. In contrast, T_p decreases with increasing $|t'/t|$, which should represent a reduction of the pseudogap region, favoring a more BCS-like behavior at intermediate coupling. We further analyze the interacting density of states to characterize the transition from a pseudogap regime to a fully gapped superconducting state. These findings suggest that NNN hopping could be a viable route to increase T_c to values closer to experimentally accessible temperature scales. Finally, we investigate the impact of Rashba spin-orbit coupling on charge-ordered phases in a Holstein-like model on a square lattice at half-filling band, within a mean-field, cluster perturbation theory and DQMC approach. As result, we show that the ground state charge density wave phase is not destroyed when the Rashba spin-orbit coupling parameter α is increasing. In addition, in a pure Rasbha spin-orbit coupling regime, where the hopping parameter is absent, we found a rich phase diagram with semimetal for low values of electron-phonon coupling and consequent transition to change density wave states for high intensities of

electron-phonon coupling. Furthermore, there is a coexistence of superconducting and charge density wave states for a high phonon frequency and electron-phonon coupling.

Keywords: Superconductivity, Ultracold Atoms, Optical Lattices, Attractive Hubbard Model, Quantum Monte Carlo, Holstein Model, Rashba Spin-Orbit Coupling.

Agradecimentos

Gostaria de expressar meus mais sinceros agradecimentos, primeiramente à minha família: aos meus pais, Florentino Vieira Fontenele e Lucilene Alves Costa, pelo apoio incondicional, especialmente nos momentos em que mais precisei. À minha esposa, Lucinete Maria, que sempre esteve ao meu lado nas batalhas diárias, mantendo-me firme em meus objetivos e lembrando-me do que realmente importa; ela foi minha luz nos momentos mais difíceis. À minha querida irmã, Maria Isadora, pessoa por quem tenho o mais profundo respeito e admiração, por cuidar de nossos pais quando eu não pude estar presente. Também a minha querida amiga Gildete Souza, por seu zelo e cuidado para com minha família. À minha prima, Girleny Fontenele, e seu esposo, Helisdenny Castro, por serem companheiros e amigos constantes. E, por fim, a todos os meus familiares que sempre estiveram presentes de forma positiva em minha vida, aos quais presto aqui meu reconhecimento e gratidão.

Na longa e, por vezes, solitária jornada acadêmica, tive a honra de conviver com pessoas maravilhosas, como tal, não poderia deixar de agradecer aos meus queridos amigos: Sebastião Júnior, que considero como um irmão; Natanael Costa, por quem tenho profunda admiração profissional e que acima de tudo é um grande amigo. Aos amigos e companheiros de todas as horas: Willian, Lucas Jadson, Lucas Lima, Julian, Kennedy, Thales, Eduarda Gonçalves, Andressa Raquel, João Pedro e Rubens Quirino. De maneira geral, sou grato a todos os colegas da pós-graduação, que tornaram os dias de trabalho mais leves e agradáveis. Agradeço também aos amigos do futebol, aos amigos da academia e, em especial, ao Carlos Guimarães e a sua esposa Karin Suzana. Aos meus vizinhos Edmilson, Marcia, Júnior e Sr. Djalma, juntamente com seu filho João, pelos momentos de conversa e descontração que tanto me fizeram bem ao longo desses anos.

No âmbito profissional preciso expressar minha gratidão, em primeiro lugar, ao meu orientador Raimundo Rocha dos Santos, por sua orientação paciente, por confiar na minha capacidade de executar o projeto de pesquisa e, ainda mais, pelos "puxões de orelha" necessários ao meu crescimento. Agradeço à professora Thereza Paiva pela imensa contribuição nos trabalhos que compõem esta tese, bem como ao professor Natanael de Carvalho Costa, que me coorientou e esteve presente em cada etapa da minha caminhada na pós-graduação. Não poderia deixar de mencionar também o professor José Pimentel, figura essencial em minha formação profissional e pessoal, hoje um colaborador e amigo por quem tenho grande estima. Agradeço ainda ao CNPq pelo apoio financeiro e à UFRJ pela infraestrutura disponibilizada.

Este trabalho representa a conclusão de um ciclo e dessa forma faço questão de lembrar daqueles que me ajudaram a iniciar essa trajetória. Agradeço aos meus professores do Ensino Médio Augustinho Brandão, em minha cidade, Cocal dos Alves, em especial ao professor Antônio Cardoso do Amaral. O esforço de todos eles foi fundamental para minha formação de base, e sei que sem isso nada seria possível em minha carreira acadêmica posterior ao ensino médio.

Por fim, esta tese é fruto de um esforço conjunto, e faço questão de expressar aqui, ainda que brevemente, meu reconhecimento a todos que contribuíram para essa jornada. A vocês, meu MUITO OBRIGADO!

Contents

List of Figures

Chapter 1

Introduction

Superconductivity (SC) is a phenomenon known since 1911, when Heike Kamerlingh Onnes conducted resistivity measurements while cooling samples of mercury to temperatures around $T \approx 4K$. Onnes observed a sharp drop in the resistivity of mercury when a critical temperature was reached. It wasn't until decades later that a theory for this phenomenon was formulated by Bardeen, Cooper, and Schrieffer - BCS - in 1957 [3]. In the BCS theory, superconductivity arises from an attractive interaction between electrons with opposite spins and momenta (s-wave), mediated by lattice vibrations (phonons). This attractive interaction is effective within an energy shell around the Fermi level, of the order of the Debye energy, $\hbar\omega_D$, characteristic of the material. As a result, conduction electrons form bound pairs, known as Cooper pairs [4], leading to the opening of a gap in the energy band, thus changing the ground state properties.

Despite the success of the BCS theory in explaining the phenomenology of conventional low-temperature superconductors, many questions about SC are still open, especially those related to unconventional superconductors. The high-temperature (T_c) superconductors [5, 6, 7, 8, 9], the recently discovered magic-angle twisted bilayer graphene [10, 11, 12, 13], and Nickelates under high-pressure [14, 15] exhibit behaviors which deviate significantly from the BCS paradigm. These materials display anomalous behavior as phase competition, pseudogap phenomena, and unconventional pairing mechanisms. Thus, addressing these phenomena requires going beyond the traditional theoret-

ical framework.

In this scenario, alternative models have been proposed to describe superconductivity in different systems. Amongst these, the attractive Hubbard model (AHM) has been playing a crucial role in describing many aspects related to SC. In its simplest form, the AHM comprises of fermions moving on a lattice, subject to a local fermionic attractive interaction, with strength U, which favors the formation of local singlet pairs. A hallmark of this model is, for instance, the possibility of naturally contemplating Cooper pair formation within a certain temperature scale, $T_p \gtrsim T_c$, where T_c is the critical temperature for superconductivity, when pairs actually condense [16, 17, 18]. This behavior, absent in the BCS pairing theory [3], is thought to be relevant to pseudogap phenomena in high-temperature cuprate superconductors [19]. Additionally, another important feature of the AHM is the possibility of smoothly interpolating between two limits: from weak coupling, where one has BCS behavior, with large pair coherence length, to strong coupling, where pairs are tightly-bound, with short coherence length, and undergo Bose-Einstein condensation (BEC) [20, 21, 22, 23]. Figure 1.1 (a) shows a qualitative phase diagram of the AHM, for band filling $\langle n \rangle \approx 0.8$.

In addition, a new class of recent experimental setups, namely cold atoms in optical lattices, has offered an alternative way to study interacting Hamiltonians, within a controlled environment and away from some of the complicating factors of real materials such as impurities and lattice defects. The continuing development of optical lattices experiments (OLE) has renewed the interest in this model due to its experimental realization in tightly controlled condition. Accordingly, ultracold fermionic atoms are loaded into a trap created by counter-propagating Gaussian laser beams, forming a periodic potential analogous to crystalline lattices. In this sense, two of the most commonly used atomic species in OLE are ^{6}Li and ^{40}K, whose hyperfine structure allows the atoms to be separated into two anti-symmetric states, analogous to $|\uparrow\rangle$ and $|\downarrow\rangle$ fermionic states, thereby creating a gas of fermionic atoms confined in the optical trap.

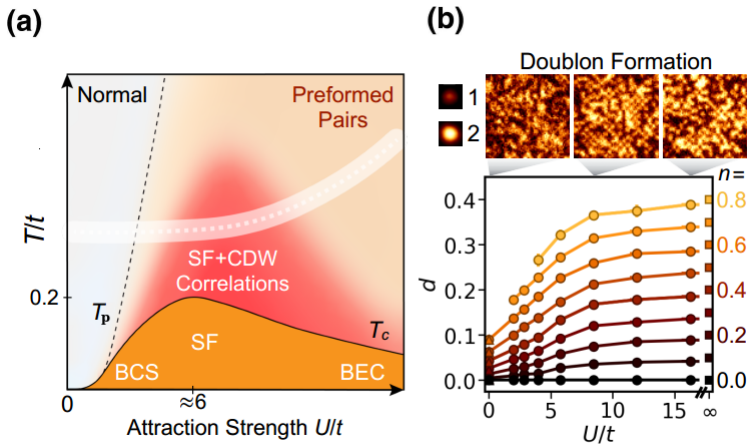

Fig. 1.1: (Color online) Atom-resolved detection of an attractive Fermi-Hubbard gas. (a) Phase diagram of the attractive Hubbard model vs. U/t and T/t at $\langle n\rangle \approx 0.8$, showing superfluid (SF) and pseudo-gap regimes. The experiment probes the pairing region ($T_c < T < T_p$) with emerging CDW and SF correlations, highlight by gray line. (b) Doublon density d vs. U/t at fixed $\langle n\rangle$, from the non-interacting ($d = (n/2)^2$) to fully-paired ($d = n^2$) limits, with sample density images above. Adapted from Ref. [1].

The composition of counter-propagating lasers in OLE enables full control over the periodic trapping potential. For instance, adjusting the amplitude and the directions of the interfering laser beams, experimentalists can precisely control the geometries and dimensionality of the lattice [24, 25, 26] (see Fig. 1.2). This flexibility is crucial for studying a wide range of phenomena in interacting systems, e.g. Kosterlitz-Thouless (KT) transition and BCS-BEC crossover [27, 23, 21]. Moreover, the interactions can be tuned via Feshbach resonances (FR), through external magnetic fields, or by quenching of kinetic energy when using deeper lattices [28, 2, 29], which makes possible the simulation of interacting quantum states.

The use of Feshbach resonances, in particular, offers a direct route to strong interaction regimes in ultracold atom gases by controlling the scattering length, a, through an external magnetic field. The idea behind this process is tuning the magnetic field, so that the energy of a bound molecular state can be brought into resonance with the energy of a state of scattering of two free atoms. This resonance occurs due to molecular and scattering states having different magnetic moments, making their relative energies field-

dependent. As a result, atoms can temporarily form virtual bound states during collisions, significantly altering their scattering properties; this enables the scattering length to be tuned to large positive ($a > 0$) or negative ($a < 0$) values, depending on the field. In particular, a can be made much larger than the average interparticle spacing, allowing access to strongly interacting regimes [30, 2, 29].

The interaction mechanism relies on the fact that atoms can occupy different quantum states, such as singlet and triplet spin configurations, which interact differently with an external magnetic field. A bound molecular state exists in one of these configurations, and its energy shifts under the influence of a magnetic field due to its distinct magnetic moment. By carefully tuning the magnetic field, the energy of the molecular state aligns with the scattering state of free atoms, creating a resonant enhancement of interactions. Thus, the scattering length $a(B)$ as function of a external magnetic field, B, near a Feshbach resonance can be given by [31, 2, 29],

$$a(B) = a_{bg}\left(1 - \frac{\Delta}{B - B_0}\right), \tag{1.1}$$

where a_{bg} is the background scattering length (away from resonance), B_0 is the magnetic field at which the resonance occurs, and Δ is the resonance width, typically $\Delta \gtrsim 1$G [29]. At resonance ($B \approx B_0$), the scattering length diverges, enabling control over strongly repulsive or attractive interactions. For example, a large positive a favors BEC, while a large negative a favors the formation of Cooper pairs and allows the study of BCS pairing.

Experimentally, this control is achieved by applying a static magnetic field to a gas of ultracold atoms. Feshbach resonances have enabled groundbreaking studies of quantum many-body phenomena, including BEC in species such as e. g. ^{85}Rb and ^{7}Li [2, 32, 33], superfluidity ad superconductivity [34, 35, 36, 27, 1], and the BCS-BEC crossover [37, 23]. This tunability also underpins experiments in optical lattice systems and pairing mechanisms in strongly correlated fermions.

In general, the OLE allow us to simulate a large variety of interactions between par-

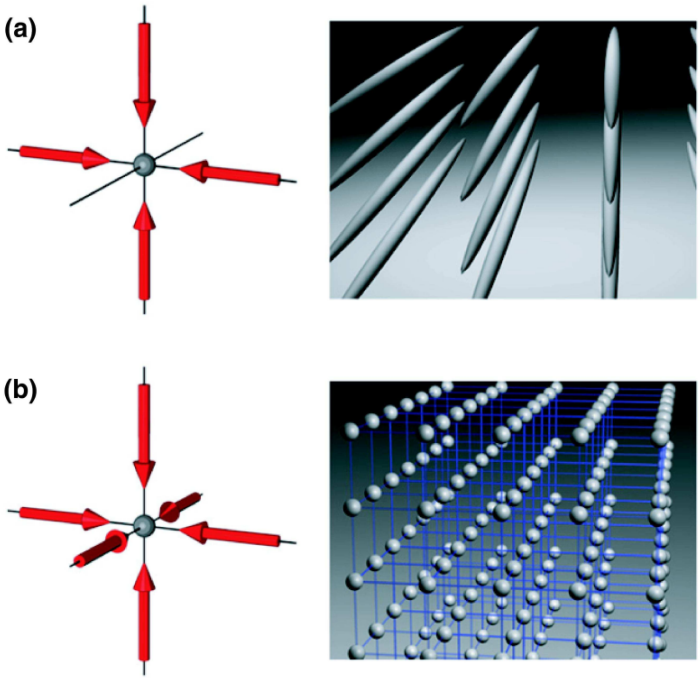

Fig. 1.2: (Color online) Two-dimensional (a) and three-dimensional (b) optical lattice potentials formed by superimposing two or three orthogonal standing waves. For a two-dimensional optical lattice, the atoms are confined to an array of tightly confining one-dimensional potential tubes, whereas in the three-dimensional case the optical lattice an be approximated by a three-dimensional simple cubic array of tightly confining harmonic oscillator potentials at each lattice site. Figure reproduced from Ref. [2].

ticles, in several lattice geometries. However, what kind of information can we extract from these experiments? OLE can provide us the correlation among particles, which are crucial to understand the many-body quantum state of the system. A widely used technique to obtain this quantities in optical lattices is time-of-flight (TOF) detection, where the optical potential is suddenly turned off, allowing the trapped atoms to expand freely. During this expansion, the momentum distribution of the atoms in the trap is captured via absorption or fluorescence imaging. These images are taken at different time intervals during the expansion, providing a direct measurement of the momentum distribution. The data obtained from TOF measurements can then be analyzed and compared with theoretical models or simulations, e. g. Monte Carlo simulations, offering relevant insights into the quantum dynamics of the atoms within the optical lattice.

Furthermore, another possibility is to explore the correlation between interacting particles in real space through the atom-resolved detection methods (ARDM). In this technique, individual atoms on the optical lattice are imaged with single-site resolution, allowing the measure spatial correlations at the level of single atoms. ARDM provide unprecedented access to the microscopic structure of many-body quantum states, making it possible to directly observe phenomena such as fermion pairing, spin and charge ordering, and local quantum correlations. Fig. 1.1 (b) shows typical results of OLE in the region of preformed pairs as expected from AHM simulations. So, TOF and ARDM are complementary techniques. While TOF is suited for capturing momentum space information, atom-resolved detection offers direct access to real-space correlations.

Although OLE are an exceptional tool in the study of interacting systems, providing an experimental route to a variety of effective interacting Hamiltonians, such as the Hubbard model (attractive and repulsive), the typical temperature scales involved in the experiments are of the order of a few tens of nano-Kelvins, which makes adequate thermometry difficult. In this way, the experiments are complemented through theoretical modeling, in several cases Quantum Monte Carlo (QMC) simulations. Since the theoretical model has a direct parallel with the quantum system built on optical lattices, QMC simulations provide the temperature dependence of correlation functions, as a function of adjustable parameters in OLE, usually the hopping amplitude t. Figure 1.1 (b) shows the characteristic results obtain from OLE, in this case the number of doubly occupied sites (doublons) on a square lattice; see Reference [1] for experimental details.

Advances in optical lattices have allowed the study of the AHM in an unprecedented way. Notwithstanding the progress achieved so far, several issues still need attention, both theoretically and experimentally. In this work, we will address some of these questions, using Determinantal Quantum Monte Carlo (DQMC) simulations to obtain the behavior of several quantities, such as critical temperature and correlation functions, which should provide a rough guide for cold atom experimentalists.

In Chapter 2, we consider the AHM on a square lattice. We use DQMC simulations to obtain accurate estimates for the critical temperature $T_c(n, U)$, which, so far, was only available for limited sets of either band filling, n, or U. Typically, the maximum T_c obtained from DQMC is about $T_c \approx 0.15\, t/k_B$ (k_B is the Boltzmann constant, which from here on will be omitted) for $U = -4t$ [38]. These estimates should be compared with the lowest temperatures reached so far in experiments on the AHM, namely $T \approx 0.4t \approx 22\,\mathrm{nK}$ [27]. Thus, the search for an AHM 'sweet spot' (i.e. a range of combinations of n and U giving rise to the maximum T_c) is of crucial importance to guide experimental studies of the phase transition on a square optical lattice; see Ref. [39].

Another aspect demanding a more quantitative description is that of temperature scales such as the degeneracy temperature and the pairing temperature. The former sets the scale below which quantum effects dominate, while the latter is usually associated with pair formation and gap opening in spin excitations [16, 17, 40, 41, 42, 43, 44]. Placing these temperature scales on a $T_c \times U$ phase diagram should therefore provide interesting insights. In addition, a third point needing attention, which we address here, concerns the characterization of the BCS-BEC crossover.

One of the main difficulties in studying the SC phase through OLE is the fact that, currently, the lowest temperatures achieved are still higher than theoretical predictions for T_c [39]. This makes the direct study of the coherent SC phase unfeasible, so that it is important to investigate scenarios which could lead to higher T_c's, closer to an experimentally accessible range.

As a rough guide to this quest, we recall that the BCS behavior of the AHM at weak coupling allows us to expect [20]

$$T_c^{\mathrm{BCS}} = \widetilde{W} \exp\left(-1/D(0)|U|\right), \tag{1.2}$$

where $\widetilde{W}$ is proportional to the bandwidth, W, and $D(0)$ is the density of states (DOS) at the Fermi level; throughout this paper we take $\widetilde{W} = W$ since the proportionality constant

is immaterial to pinpoint the maximum critical temperatures. According to Eq. (1.2), one possibility to enhance T_c is to increase $D(0)$, while keeping fixed both the fermionic density and attractive interaction strength U. As we will see, for two-dimensional systems this may be achieved by adding a second layer and adequately tuning the hopping, t_z, between the layers. Similar arguments apply to a simple cubic lattice, where a tunable t_z could benefit from the fact that $T_c \neq 0$ for $t_z = t$ even at half filling [17]. By varying t_z between 0 and 1, we follow a dimensional crossover between two- and three dimensions.

In view of these possibilities, a systematic study of T_c for the anisotropic AHM both in the bilayer and in three dimensions is of interest. Thus, in Chapter 3 we perform DQMC simulations to investigate the AHM with an anisotropic hopping between layers; see Ref. [45].

Still with the purpose of enhancing T_c through an increase in $D(0)$, in Chapter 4 we explore an alternative route, namely the addition of second-neighbor hopping, t', to the attractive Hubbard Hamiltonian. This causes a shift in the van Hove singularity, opening the possibility to tune t' to generate larger values of $D(0)$; see Refs. [46] and [47].

Here we also focus on the origin of the pairing interaction. It is known that s-wave superconductivity can be understood in a framework where phonons couple to conduction electrons in a material, leading to a coherent state of Cooper pairs. This electron-phonon coupling (EPC), is the basis of the BCS theory for conventional superconductors. However, EPC can also give rise to strong charge interactions, which create instabilities in the metallic system, leading to a ground state with a spatially-modulated charge order [48, 49]. Such a state is characterized by a gapped single-particle charge spectrum.

Interestingly, both CDW and superconducting phases have been observed in Transition Metal Dichalcogenides (TMDs). These phases emerge in compounds which stabilize in either centrosymmetric (1T) [50] or non-centrosymmetric (2H) [51] structures. Additionally, due to the high atomic number of the transition metal atoms, TMD compounds typically exhibit strong intrinsic spin-orbit coupling (SOC). However, the interplay be-

tween SOC and EPC, particularly how SOC influences CDW formation, remains a less explored issue. To address this, in Chapter 5, we investigate the impact of SOC on charge correlations on a square lattice with EPC. Using the Holstein model framework combined with Rashba spin-orbit coupling, we set up an effective Hamiltonian, which we study through Mean Field Theory (MFT), Cluster Perturbation Theory (CPT), and Quantum Monte Carlo (QMC) simulations, to extract key insights into the relevant physical quantities; see Refs. [52] and [53].

Finally, in Chapter 6 we summarize the main findings of this work, and discuss perspectives and open questions which merit further exploration in future research.

Chapter 2

Two-dimensional attractive Hubbard model and the BCS-BEC crossover

2.1 Introduction

As already highlighted in the Chapter 1, the Attractive Hubbard Model (AHM) [20] has played an important role in elucidating many aspects of s-wave superconductivity, or superfluidity, in two-dimensional systems. For instance, this model enables a smooth interpolation between the weak attractive interaction limit, BCS-like, and tightly bound pairs limit, BEC-like. Additionally, the AHM naturally accounts for the presence of a preformed pair region, often associated to the pseudogap phase observed in cuprates.

Advances in ultracold atom experiments in optical traps [29, 54, 2, 55, 56, 27, 57] have renewed interest in AHM, offering direct experimental applicability of this model. However, despite the extensive literature, both experimental and theoretical questions remain, such as accurate estimates for the critical temperature, T_c, on the square lattice, for a wide range of band fillings, $\langle n \rangle$, and attractive interaction strength, U [38, 18], as well as identifying the optimal critical temperature for a given set of parameters. Furthermore, a quantitative description of the pairing temperature and the degeneracy temperature is also needed [16, 17, 40, 41, 42, 43, 44].

The BCS-BEC crossover also demands attention. On an optical lattice one has at our disposal very accurate imaging techniques [2, 58] which can provide quantitative measures

of double occupancy distribution; it would be helpful to gain further quantitative insight into this crossover. On the solid state front, the BCS-BEC crossover has been recently studied by gate-controlled doping the layered material ZrNCl with Li^+ intercalation [59], thus allowing for measurements of both critical and pseudogap temperatures.

In actual fact, one may envisage yet another crossover: while at weak coupling the normal phase may be described by a Fermi liquid, one should not expect such a simple behavior at strong coupling. The existence of tightly bound pairs, whose interactions may be thought of as being mediated by the unpaired fermions, may be indicative of a non-Fermi liquid regime [60, 61, 62, 63].

To address these issues, we resort to DQMC simulations of the AHM. This chapter is organized as follows: Section 2.2 introduces the model and DQMC methodology, highlighting key observables. Section 2.3 presents and discusses phase diagrams for critical, degeneracy, and pairing temperatures. The BCS-BEC crossover is discussed in Section 2.4, with conclusions in Section 2.5.

2.2 Model and Methodology

The attractive Hubbard Hamiltonian reads

$$\mathcal{H} = -t \sum_{\langle \mathbf{i},\mathbf{j}\rangle,\,\sigma} (c^{\dagger}_{\mathbf{i},\sigma} c_{\mathbf{j},\sigma} + \text{H.c.}) - \mu \sum_{\mathbf{i},\sigma} n_{\mathbf{i},\sigma} - |U| \sum_{\mathbf{i}} (n_{\mathbf{i}\uparrow} - 1/2)(n_{\mathbf{i}\downarrow} - 1/2), \tag{2.1}$$

where the sums run over sites of a square lattice, with $\langle \mathbf{i}, \mathbf{j} \rangle$ denoting nearest-neighbor sites. $c^{\dagger}_{\mathbf{i}\sigma}$ ($c_{\mathbf{i}\sigma}$) is a creation (annihilation) operator of an electron on a given site $\mathbf{i}$ with spin σ, and $n_{\mathbf{i}\sigma} \equiv c^{\dagger}_{\mathbf{i}\sigma} c_{\mathbf{i}\sigma}$ being fermionic number operator in the conventional second quantization formalism. The first term on the right hand side of Eq. (2.1) describes particle hopping, with H.c. denoting hermitian conjugate, while the second term controls the band filling through the chemical potential, μ. The last term corresponds to the local attractive interaction between electrons, with coupling strength $|U|$. Here, the hopping integral t sets the energy scale.

In the DQMC simulations (see Appendix A for a brief description) for the AHM, a discrete Hubbard-Stratonovich transformation is used to deal with the quartic terms, such that it leads to positive 'Boltzmann factors'; this renders the simulations free from the infamous 'minus-sign problem' [64, 65, 66, 67]. We take $\beta = M\Delta\tau$, with M the number of imaginary slices, and $\Delta\tau$ being the grid of the imaginary-time coordinate axis. This decomposition leads to an error proportional to $(\Delta\tau)^2$, which can be systematically reduced as $\Delta\tau \to 0$. Here, we choose $\Delta\tau \leq 0.1$ (depending on the temperature), which is small enough so that systematic errors are comparable to the statistical ones (from the Monte Carlo sampling).

We collect DQMC data for several quantities probing superconductivity. The s-wave pair correlation function is defined as

$$C^{\Delta}_{\mathbf{ij}} \equiv \langle b^{\dagger}_{\mathbf{i}} b_{\mathbf{j}} + \text{H.c.} \rangle, \tag{2.2}$$

where

$$b_{\mathbf{i}} \equiv c_{\mathbf{i}\downarrow} c_{\mathbf{i}\uparrow} \quad \text{and} \quad b^{\dagger}_{\mathbf{i}} \equiv c^{\dagger}_{\mathbf{i}\uparrow} c^{\dagger}_{\mathbf{i}\downarrow} \tag{2.3}$$

respectively annihilates and creates a pair at site $\mathbf{i}$. The decay of $C^{\Delta}_{\mathbf{ij}}$ with the distance, $r_{\mathbf{ij}} \equiv |\mathbf{i} - \mathbf{j}|$, probes the resilience of pair coherence at a given temperature. The Fourier transform of $C^{\Delta}_{\mathbf{ij}}$ at $\mathbf{q} = 0$ defines the s-wave pair-field structure factor,

$$P_s = \langle \Delta^{\dagger}\Delta + \Delta\Delta^{\dagger} \rangle, \tag{2.4}$$

with

$$\Delta^{\dagger} = \frac{1}{\sqrt{N}} \sum_{\mathbf{i}} b^{\dagger}_{\mathbf{i}} \tag{2.5}$$

being the pair-field operator.

At a Kosterlitz-Thouless transition the finite-size scaling (FSS) behavior of P_s may be obtained upon integration of $C^{\Delta}_{\mathbf{ij}}$ over a two-dimensional system of linear dimension L [68, 38],

$$P_s = L^{2-\eta(T_c)} f(L/\xi), \quad L \gg 1,\ T \to T_c^{+}, \tag{2.6}$$

where $\eta(T_c) = 1/4$ [69, 70], and

$$\xi \sim \exp\left[\frac{A}{(T-T_c)^{1/2}}\right], \tag{2.7}$$

with A being a constant independent of temperature.

As discussed previously [38], estimates for the critical temperature obtained through an exponential correlation length, Eq. (2.7), must be supplemented by an analysis of the superfluid density, ρ_s, for accuracy; the latter can be expressed in terms of the current-current correlation functions as [71, 72],

$$\rho_s = \frac{D_s}{4\pi e^2} = \frac{1}{4}[\Lambda^L - \Lambda^T], \tag{2.8}$$

where D_s is the superfluid weight, and

$$\Lambda^L \equiv \lim_{q_x \to 0} \Lambda_{xx}(q_x, q_y = 0, \omega_n = 0), \tag{2.9}$$

and

$$\Lambda^T \equiv \lim_{q_y \to 0} \Lambda_{xx}(q_x = 0, q_y, \omega_n = 0), \tag{2.10}$$

are, respectively, the limiting longitudinal and transverse responses, with

$$\Lambda_{xx}(\mathbf{q}, \omega_n) = \sum_{\boldsymbol{\ell}} \int_0^\beta d\tau \, e^{i\mathbf{q}\cdot\boldsymbol{\ell}} e^{i\omega_n \tau} \Lambda_{xx}(\boldsymbol{\ell}, \tau), \tag{2.11}$$

where $\omega_n = 2n\pi T$;

$$\Lambda_{xx}(\boldsymbol{\ell}, \tau) = \langle j_x(\boldsymbol{\ell}, \tau) j_x(0,0) \rangle, \tag{2.12}$$

where

$$j_x(\boldsymbol{\ell}, \tau) = e^{\mathcal{H}\tau} \left[it \sum_\sigma \left(c^\dagger_{\boldsymbol{\ell}+\hat{\mathbf{x}},\sigma} c_{\boldsymbol{\ell},\sigma} - c^\dagger_{\boldsymbol{\ell},\sigma} c_{\boldsymbol{\ell}+\hat{\mathbf{x}},\sigma} \right) \right] e^{-\mathcal{H}\tau} \tag{2.13}$$

is the x-component of the current density operator; see Ref. [71] and Appendix B.1 for details.

At the KT transition, the following universal-jump relation involving the helicity modulus holds [73]:

$$T_c = \frac{\pi}{2} \rho_s^-, \tag{2.14}$$

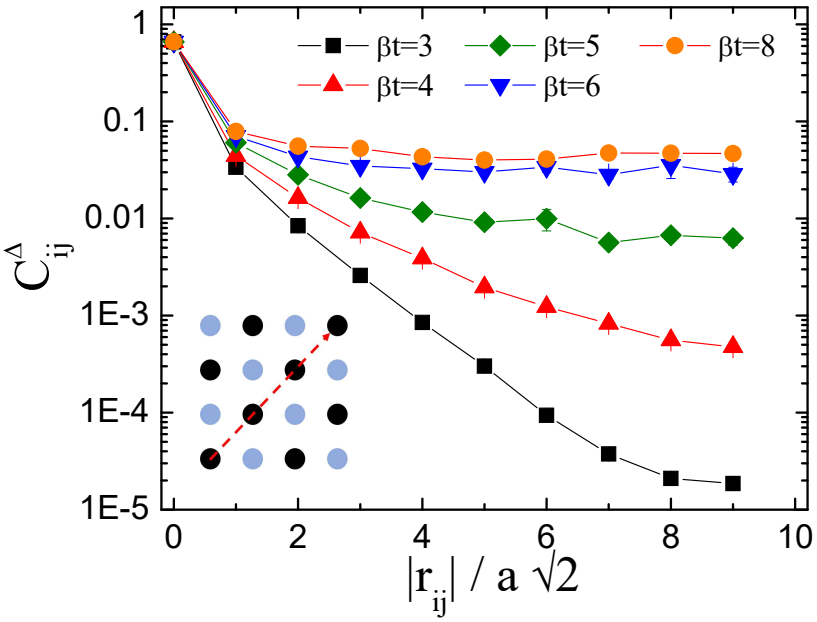

Fig. 2.1: (Color online) Pairing correlation function as a function of distance along the diagonal direction (see inset) on an 18×18 lattice, for different inverse temperatures, β, with $U/t = -5$ and electronic density $\langle n \rangle = 0.5$. PBC limits the farthest distance to $La/\sqrt{2}$, where a is the lattice spacing.

where ρ_s^- is the value of the helicity modulus just below the critical temperature. We therefore calculate both Λ^L and Λ^T by DQMC simulations to obtain ρ_s through Eq. (2.8). T_c is then determined by plotting $\rho_s(T)$, and looking for the intercept with $2T/\pi$ [74, 75, 76, 38]; see below.

For our purposes here, the magnetic properties are probed by the uniform susceptibility. This is obtained through the fluctuation-dissipation theorem, which leads to $\chi_s = \beta\langle S^2 \rangle$, with $\langle S^2 \rangle$ being the uniform spin structure factor,

$$\langle S^2 \rangle = \frac{1}{N} \sum_{\mathbf{ij}} \langle \mathbf{S_i} \cdot \mathbf{S_j} \rangle, \tag{2.15}$$

where $\mathbf{S_i} \equiv (1/2)\mathbf{m_i}$, with the components of the magnetization operator being

$$m_{\mathbf{i}}^x \equiv c_{\mathbf{i}\uparrow}^\dagger c_{\mathbf{i}\downarrow} + c_{\mathbf{i}\downarrow}^\dagger c_{\mathbf{i}\uparrow}, \tag{2.16a}$$

$$m_{\mathbf{i}}^y \equiv -i \left(c_{\mathbf{i}\uparrow}^\dagger c_{\mathbf{i}\downarrow} - c_{\mathbf{i}\downarrow}^\dagger c_{\mathbf{i}\uparrow} \right), \tag{2.16b}$$

$$m_{\mathbf{i}}^z \equiv n_{\mathbf{i}\uparrow} - n_{\mathbf{i}\downarrow}. \tag{2.16c}$$

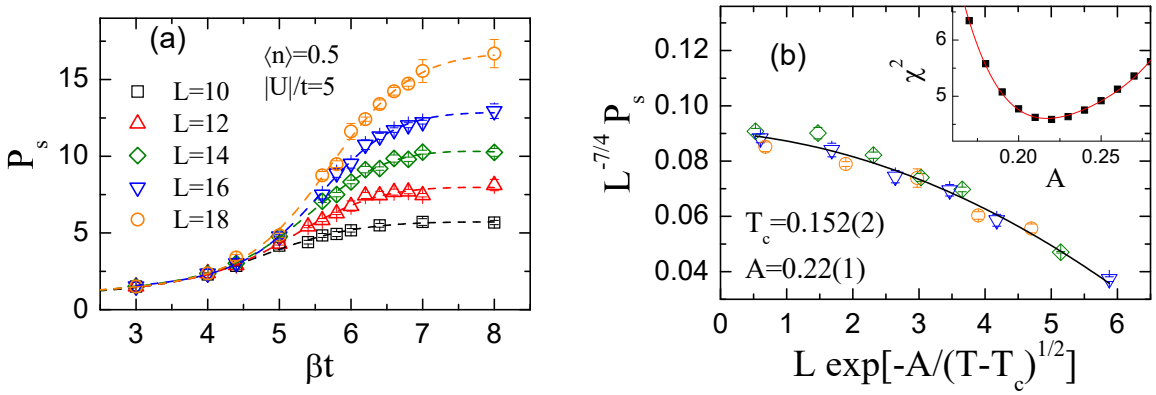

Fig. 2.2: (Color online) (a) Pair structure factor as a function of the inverse of temperature β, for different lattice sizes, and fixed $\langle n \rangle = 0.5$ and $U/t = -5$. (b) The data collapse of P_s according to the Kosterlitz-Thouless FSS analysis. Inset: the chi-squared values of a polynomial fit to the data collapse, for fixed $T = 0.152$ (in units of t). The curves are guides to the eye.

Throughout this Chapter our simulations were carried out on $L \times L$ square lattices with periodic boundary conditions (PBC), such that $L \leq 18$. Typically our data have been obtained after 5-10$\times 10^3$ warming-up steps followed by $2-6 \times 10^5$ sweeps for measurements, depending on the temperature, interaction strength and electronic density.

2.3 Results

2.3.1 Critical temperature

In discussing the critical temperature, we first recall that charge-density wave (CDW) and singlet superconducting (SS) correlations are degenerate at half filling, thus leading to a three-component order parameter: by virtue of the Mermin-Wagner theorem, there is no long-range order at finite temperatures, and $T_c = 0$ for any U. As one dopes away from half filling, CDW correlations are suppressed but the two-component SS correlations remain, so that a Kosterlitz-Thouless (KT) transition at finite temperatures, T_c, takes place.

Let us then consider the behavior of the pairing correlation functions away from half filling, as the temperature is varied. Figure 2.1 presents $C^{\Delta}_{\mathbf{ij}}$ along the diagonal direction

of the lattice, for fixed $\langle n \rangle = 1/2$, and $U/t = -5$. At high temperatures the steady decay of $C_{\mathbf{ij}}^{\Delta}$ reflects the lack of pair coherence along the lattice, as expected. The situation changes completely at low temperatures, $\beta t \gtrsim 5$, with the correlations now reaching a finite value at large distances, compatible with long-range order in the ground state. This long-range behavior is also manifested in the pairing structure factor, Eq. (2.4), as displayed in Fig. 2.2 (a): P_s stabilizes at low temperatures as a result of the range of correlations being limited by the finite size of the lattice, but nonetheless experiencing a steady increase with L.

As mentioned in Sec. 3.2, we may use the FSS ansatz for P_s at finite temperatures, Eq. (2.6), to determine T_c. Figure 2.2 (b) shows the collapse of the data appearing in panel (a), in which T_c and A are considered as independent variables, adjusted through a least squares fit. The inset of Fig. 2.2 (b) illustrates this process, from which, by minimizing the χ^2 function for a polynomial fit of the data collapse, we are able to find the most appropriate value for A, while keeping T_c fixed. When this procedure is performed recursively for T_c and A, we obtain the best data collapse.

The helicity modulus provides an alternative way to estimate the critical temperature, using Eq. (2.14), as illustrated in Fig. 2.3 for the same filling and U as in Fig. 2.2: the intersection of ρ_s for each lattice size with the straight line $2T/\pi$ yields estimates for T_c. We note that the position of the intersections are not too sensitive to L – whether we take into account the scatter of all intersections shown, or just the data for the largest lattice size, the final estimate will hardly differ from $T_c = 0.150 \pm 0.003$ (in units of t), which is in agreement with the value obtained from the data collapse.

We map out the critical temperature for other values of U and $\langle n \rangle$, making use of the weak dependence of the superfluid density with L: in what follows, most of the results for T_c have been determined from simulations on lattices with linear size $L = 14$ or 16. Figure 2.4 (a) shows the critical temperature as a function of U/t, for different fermionic densities, and we note that it displays a maximum, $T_c^{\max}$, at some value, U_m,

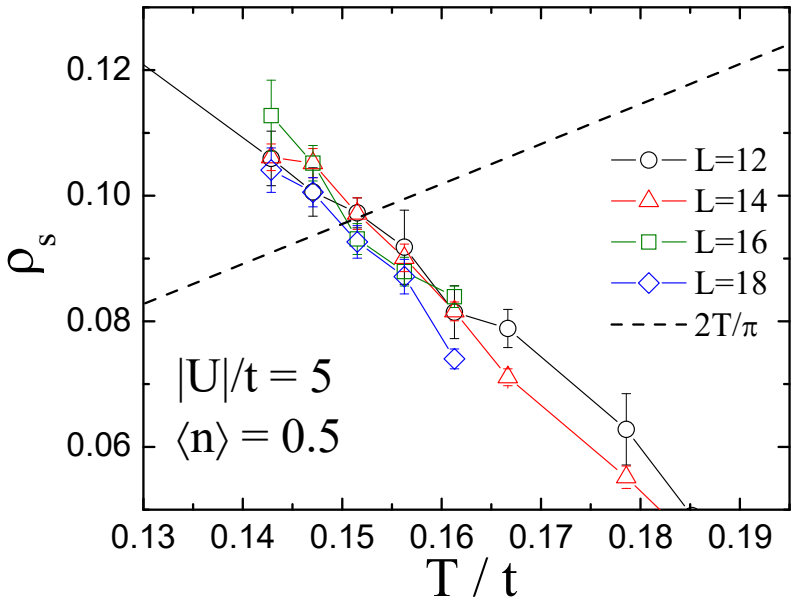

Fig. 2.3: (Color online) Temperature behavior of the superfluid density, ρ_s, at fixed $\langle n\rangle = 0.5$ and $U/t = -5$, and for several lattice sizes.

scale	$\langle n\rangle$	$U/t=-3$	$U/t=-4$	$U/t=-5$	$U/t=-6$	$U/t=-8$
T_c	0.20	0.061 ± 0.002	0.077 ± 0.006	0.091 ± 0.003	0.089 ± 0.003	0.077 ± 0.006
	0.35	0.067 ± 0.004	0.106 ± 0.007	0.130 ± 0.005	0.128 ± 0.003	0.11 ± 0.01
	0.50	0.079 ± 0.001	0.133 ± 0.002	0.152 ± 0.002	0.153 ± 0.002	0.130 ± 0.002
	0.70	0.105 ± 0.006	0.149 ± 0.002	0.164 ± 0.003	0.161 ± 0.005	0.139 ± 0.004
	0.87	0.114 ± 0.003	0.152 ± 0.002	0.164 ± 0.003	0.157 ± 0.001	0.137 ± 0.002
T_p	0.35	0.40 ± 0.05	0.73 ± 0.06	1.34 ± 0.09	1.6 ± 0.1	2.6 ± 0.1
	0.50	0.54 ± 0.03	0.73 ± 0.03	1.25 ± 0.09	1.7 ± 0.2	2.7 ± 0.1
	0.70	0.44 ± 0.05	0.84 ± 0.08	1.2 ± 0.1	1.89 ± 0.07	2.8 ± 0.3
	0.87	0.50 ± 0.05	0.76 ± 0.03	1.4 ± 0.3	2.0 ± 0.2	2.8 ± 0.5
T_d	0.35	1.18 ± 0.07	1.06 ± 0.06	0.95 ± 0.05	0.87 ± 0.04	0.61 ± 0.06
	0.50	1.5 ± 0.1	1.5 ± 0.1	1.34 ± 0.09	1.18 ± 0.07	1.06 ± 0.06
	0.70	2.4 ± 0.1	2.22 ± 0.05	2.13 ± 0.05	2.13 ± 0.05	1.96 ± 0.04
	0.87	3.03 ± 0.09	3.03 ± 0.09	3.03 ± 0.09	3.03 ± 0.09	3.03 ± 0.09

Table 2.1: Superconducting critical temperature, T_c, pairing temperature, T_p, and degeneracy temperature, T_d, (all in units of t) for different fermionic densities (rows) and different strengths of attraction (columns).

which depends very weakly on $\langle n\rangle$ within the range considered here; we will return to this point below, in connection with the BCS-BEC crossover. It is also instructive to examine the dependence of T_c with the electronic density, for fixed values of U, with the

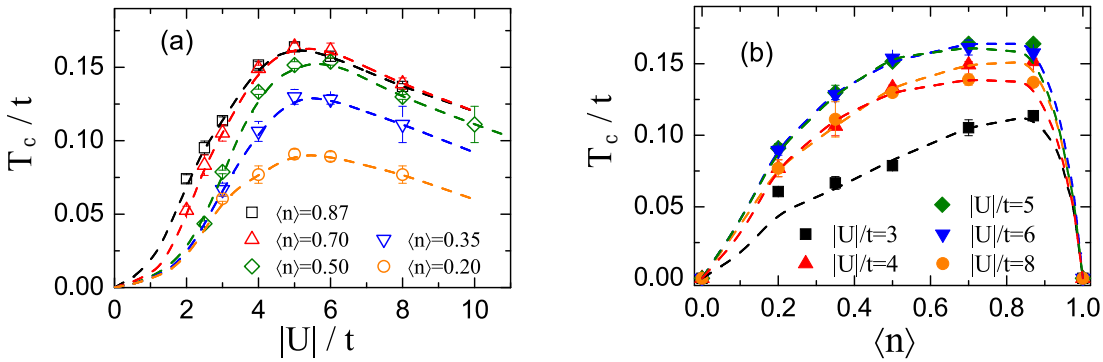

Fig. 2.4: (Color online) Critical temperatures as function of (a) the interaction strength $|U|/t$, and (b) the electronic density $\langle n \rangle$. The curves are guides to the eye.

results shown in Fig. 2.4 (b). We see that for each fixed U, T_c displays a broad maximum for $0.7 \lesssim \langle n \rangle \lesssim 0.9$, and it drops sharply to zero at half filling by virtue of the Mermin-Wagner theorem; accordingly, in three dimensions $T_c(\langle n \rangle)$ for fixed U displays a maximum around $\langle n \rangle \approx 0.9$, but reaches a finite value at $\langle n \rangle = 1$ [17]. We also provide the estimates for the critical temperature in tabular form (see Table 2.1), while the location of the 'sweet spot' for T_c is highlighted in Figure 2.5. Our results for T_c are in good agreement with estimates for T_c using different methods on lattices, and for the specific sets of $\langle n \rangle$ and U available; see, e.g. Refs. [20, 60, 77, 78].

2.3.2 Pairing temperature

As mentioned in the Introduction, the pairing temperature provides a temperature scale around which Cooper pairs are formed; the pair-breaking gap is therefore expected to be related to a gap in spin excitations, which, in turn, may be detected as a downturn in the uniform magnetic susceptibility, χ_s, as the temperature is lowered [16, 17, 40, 41, 42, 43].

Accordingly, Fig. 2.6 shows our DQMC data for the temperature dependence of the uniform susceptibility, χ_s [see Eq. (2.15)], at quarter filling and for different strengths of the attractive interaction. We first note that the magnitude of χ_s decreases with increasing $|U|$, following the trend predicted within RPA, $\chi^{\mathrm{RPA}} = \chi_0/(1 + |U|\chi_0)$. In addition, for fixed U we see that χ_s drops steadily below some temperature, whose location depends on

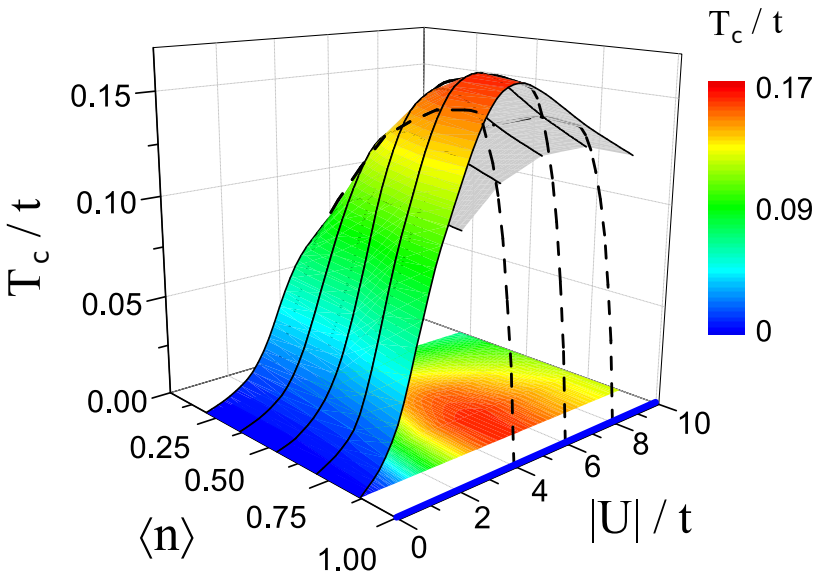

Fig. 2.5: (Color online) Finite temperature phase diagram of the attractive Hubbard model in the square lattice.

U. In line with the idea that this downturn in χ_s signals the formation of local pairs within some temperature scale [16, 17, 40, 41, 42, 43], we adopt the position of the maximum in χ_s as the pairing scale, $T_p(U)$. As Fig. 2.6 shows, at strong coupling the maxima can be quite broad, so that their position are determined by inspection of the actual numerical output for χ_s, taking into account its error bars; this yields a range of temperatures in which the maximum lies. This somewhat flexible definition is in line with the fact that we are dealing with a crossover, hence a temperature scale, not with a sharp transition.

By repeating this procedure for different band fillings, we generate the plots $T_p(U, \langle n \rangle)$ shown in blue in Figs. 2.7(a)-(d); these data are also displayed in Table 2.1. For comparison of trends, we also include $T_c(U, \langle n \rangle)$ in each panel of Figs. 2.7(a)-(d). We see that the difference between T_p and T_c gets smaller as U decreases, which is a manifestation of the fact that in the BCS regime Cooper pairs are formed and condense at the same temperature. By contrast, for large $|U|$, pairs are formed at temperatures much higher than the condensation temperature: $T_p \sim |U|$, while $T_c \sim |U|^{-1}$. Whenever comparison

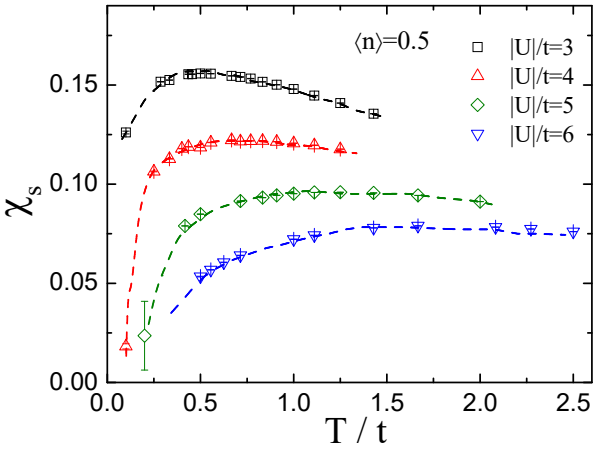

Fig. 2.6: The uniform spin susceptibility as a function of temperature, for different values of the on-site attraction, $|U|$, and at quarter filling, $\langle n\rangle = 0.5$, for a linear lattice size $L = 14$. The curves are guides to the eye.

is available, our results for T_p follow trends expected from other methods [20, 78].

2.3.3 Degeneracy temperature

At high temperatures, the fugacity of a Fermi gas is small, $z \ll 1$, while deep in the degenerate regime, fully dominated by quantum effects, one has $z \gg 1$. We may therefore define a temperature scale for degeneracy, T_d, as the one in which $\ln z \sim 1$, i.e. $\mu = k_B T$. However, we note that in dealing with tight-binding fermions on a lattice, the bandwidth is finite and shifted from the continuum parabolic band. Therefore, in order to keep the analogy with the Fermi gas, one should shift the bottom of the band to zero, i.e. $\mu \to \mu + 4t$. Similarly, due to the Hubbard term in the Hamiltonian, the Hartree shift must be taken into account when defining T_d [16] which leads to $\mu \to \mu + |U|\big[(\langle n\rangle - 1\big]/2$. Thus, the degeneracy temperature is given by the solution of

$$\mu(T) = k_B T - 4t - \frac{|U|}{2}\big[\langle n\rangle - 1\big] \ , \tag{2.17}$$

for fixed $\langle n\rangle$ and U. For instance, the data points in Fig. 2.8 represent the temperature dependence of the chemical potential giving rise to $\langle n\rangle = 0.5$, for different values of U, while the (blue) dashed line is the right-hand side of Eq. (2.17) for fixed $|U|/t = 10$. Thus,

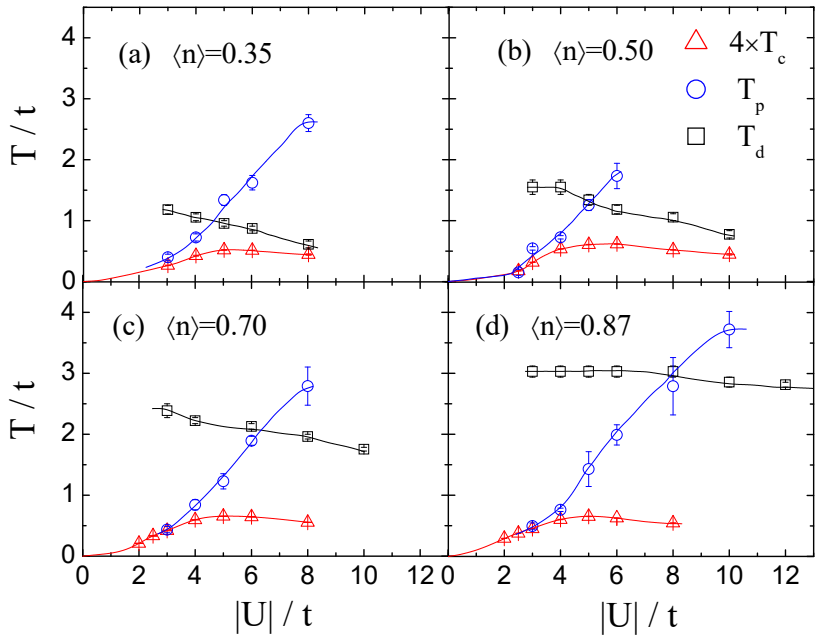

Fig. 2.7: Critical (T_c), pairing (T_p), and degeneracy (T_d) temperatures (in units of t) as functions of the interaction strength $|U|/t$, obtained from DQMC simulations on a lattice with linear size $L = 14$, and different band fillings. The curves are guides to the eye.

the degeneracy temperature as a function of $|U|$ for a given $\langle n \rangle$ is obtained by extracting the points of intersection between the dashed curves (one for each value of $|U|$) and the corresponding $\mu(T)$ curves; the final outcome for this filling is displayed as the (black) dash-dotted line in Fig. 2.8.

The results for the degeneracy temperature appear in Figs. 2.7(a)-(d), as well as in Table 2.1. For fixed $\langle n \rangle$, we see that T_d decreases with $|U|$, while for fixed $|U|$ it increases with $\langle n \rangle$. The relative positions between T_d and T_p in the different regimes of the pairing interaction allows us to form an intuitive picture of the mechanisms at play. First, we note that as the temperature is lowered in the weaker coupling part of the diagrams, fermionic particles first enter into a degenerate Fermi liquid regime, then they pair up, and finally condense into a superfluid at lower temperatures. By contrast, in the strong coupling region the strength of the interaction forces fermions to first pair up forming bosonic particles before they enter into the degenerate regime at a lower temperature. In this regime, the effective density of unpaired fermions is smaller than the nominal $\langle n \rangle$, so

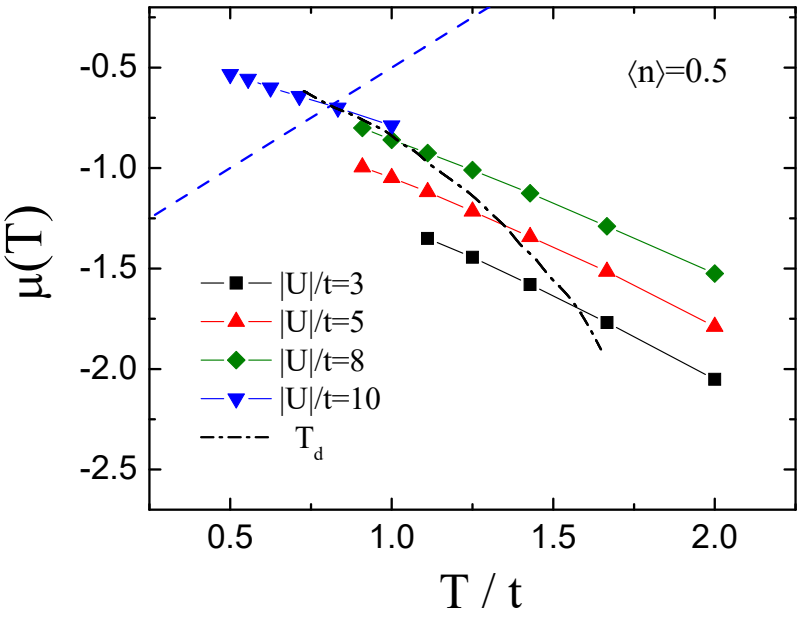

Fig. 2.8: Each set of data points represents the temperature dependence of the chemical potential required to keep a constant fermionic density, $\langle n \rangle = 0.5$, for a given U. The (blue) dashed line is the right-hand side of Eq. (2.17) for $|U|/t = 10$, whose intersection with the $|U|/t = 10$ data points determines T_d for this particular U. The (black) dash-dotted line is the locus of the intersections for different values of $|U|$.

that a smaller temperature is required to make their wave packets overlap. At a given temperature, the unpaired fermions act mostly as glues mediating the formation of the superfluid condensate (more on this below).

2.4 Characterization of the BCS-BEC crossover

While there is consensus over the main qualitative differences between the BCS and BEC regimes, a quantitative characterization is still lacking, especially highlighting quantities accessible through quantum gas microscope measurements in optical lattices. Having established the different temperature scales, we now discuss some quantities which could be followed throughout the crossover.

The average double occupancy on a given site is defined as

$$d_{\mathbf{i}} = \langle n_{\mathbf{i}\uparrow} n_{\mathbf{i}\downarrow} \rangle, \tag{2.18}$$

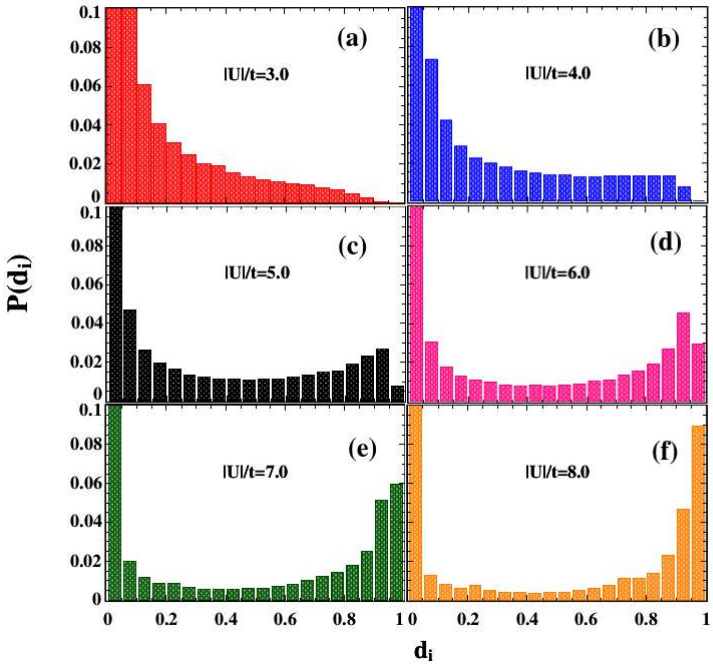

Fig. 2.9: (Color online) Histograms of the normalized statistical weight of the double occupancy, for different values of the attractive interaction U/t, for fixed fermionic density, $\langle n \rangle = 0.5$, temperature, $T/t = 0.2$, and lattice size, $L = 14$.

.

and ranges from 0 to 1. We note that in the extreme limit of $|U| \to \infty$ and $T \to 0$, sites would be either doubly occupied by fermions or empty: a distribution of $d_{\mathbf{i}}$ would be peaked at both $d_{\mathbf{i}} = 0$ and $d_{\mathbf{i}} = 1$. In the opposite limit of weak coupling, $d_{\mathbf{i}}$ should be strongly peaked at $d_{\mathbf{i}} = 0$. Accordingly, Figs. 2.9 and 2.10 follow the evolution of the double-occupancy distribution with the strength of attraction, at a fixed temperature, but for different band fillings. For $n = 0.5$, a peak near $d_{\mathbf{i}} = 1$ starts developing at $|U|/t \approx 4.5 \pm 0.5$, and as $|U|$ increases this peak becomes more pronounced while moving towards $d_{\mathbf{i}} = 1$. For $n = 0.87$, the $d_{\mathbf{i}} = 1$ peak starts developing at smaller values of $|U|$, namely at $|U|/t \approx 3.5 \pm 0.5$. The reason for this decrease in $|U|$ must be attributed to the larger number of fermions available to pair up. This also explains the fact that for a given $|U|$, it is more likely to find doubly occupied sites at larger fermionic densities.

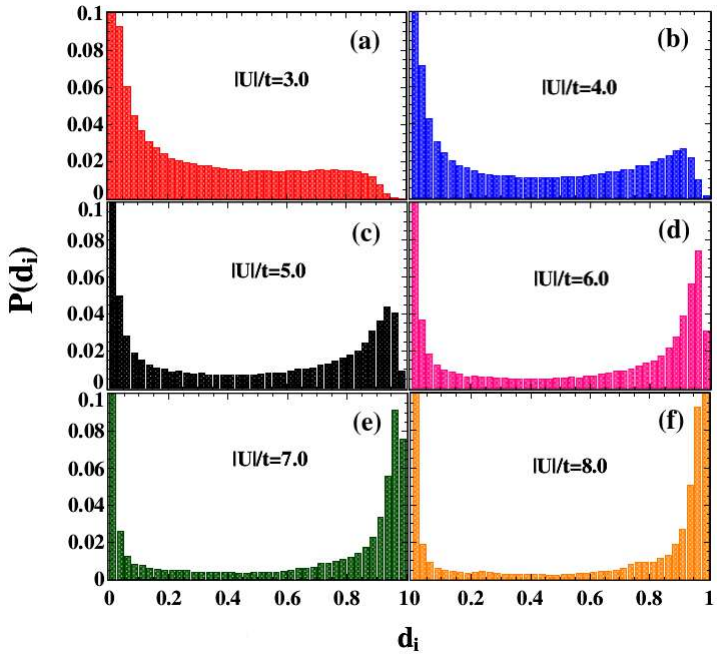

Fig. 2.10: (Color online) Same as Fig. 2.9, but for density, $\langle n \rangle = 0.87$.

Another interesting crossover probe is the density distribution in momentum space,

$$n_{\mathbf{k}} \equiv \langle c^{\dagger}_{\mathbf{k}\sigma} c_{\mathbf{k}\sigma} \rangle, \tag{2.19}$$

where, for brevity, the spin index was omitted in $n_{\mathbf{k}}$, since $n_{\mathbf{k}\uparrow} = n_{\mathbf{k}\downarrow}$ in the absence of a symmetry-breaking magnetic field. The results are displayed in Fig. 2.11 for $\langle n \rangle = 0.5$ and for increasing values of $|U|/t$. We see that while on the weak coupling side of the crossover the distribution bears some resemblance with one with a Fermi surface, on the strong coupling side the fermions are distributed way beyond the non-interacting Fermi surface. One may therefore regard this as a crossover between a Fermi liquid (FL) at weak coupling and a non-Fermi liquid (NFL) at strong coupling. Interestingly, the NFL regime seems to appear when the occurrence of double occupancy is significant: this can be interpreted as indicating that unpaired fermions are also strongly tied to the tightly bound bosonic quasiparticles, which renders the FL framework inapplicable.

This can be put in a more quantitative way, by calculating the quasi-particle weight,

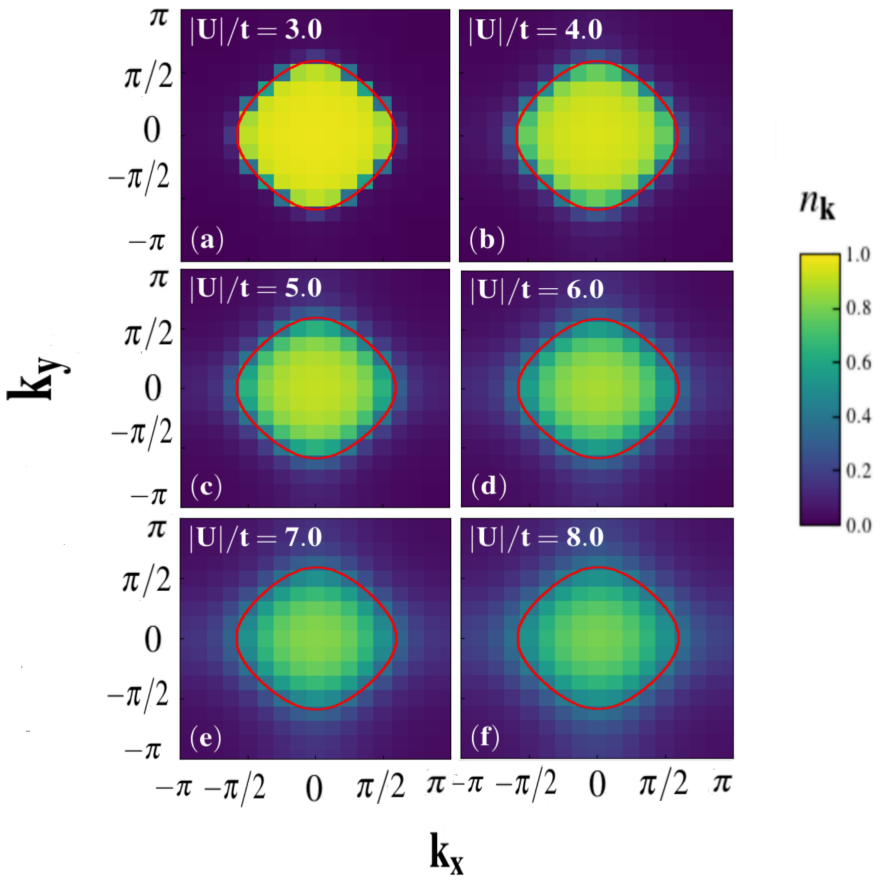

Fig. 2.11: Contour plot of momentum distribution for different values of $|U|/t$. Data are for density $\langle n \rangle = 0.5$, temperature $T/t \approx 0.42$, and linear lattice size $L = 16$. The red curve is the non-interacting Fermi surface for the same electronic density.

given in a form amenable to DQMC simulations [79, 80, 81, 82, 83],

$$\begin{aligned} Z &= \left(1 - \frac{\partial \Sigma'(\omega)}{\partial \omega}\bigg|_{\omega \to 0}\right)^{-1} \\ &\approx \left(1 - \frac{\mathrm{Im}\left[\Sigma(i\omega_n)\right]}{\omega_n}\bigg|_{\omega_n \to 0}\right)^{-1}, \end{aligned} \tag{2.20}$$

where Σ' is the real part of the self-energy, Σ, and $\omega_n = (2n+1)\pi T$ are the Matsubara frequencies. Here, we obtain the self-energy by performing $\Sigma^{-1}(\mathbf{k}, ß\omega_n) = G^{-1}(\mathbf{k}, ß\omega_n) - ß\omega_n - \left[\epsilon(\mathbf{k}) - \mu\right]$, with $\epsilon(\mathbf{k})$ being the noninteracting dispersion, and $G^{-1}(\mathbf{k}, ß\omega_n)$ directly calculated through a Fourier transform with respect to the imaginary time [79].

Figure 2.12 shows the temperature dependence of the quasiparticle weight for $\langle n \rangle = 0.5$. The locus of critical temperatures, $T_c(U)$, for the different values of U/t reminds

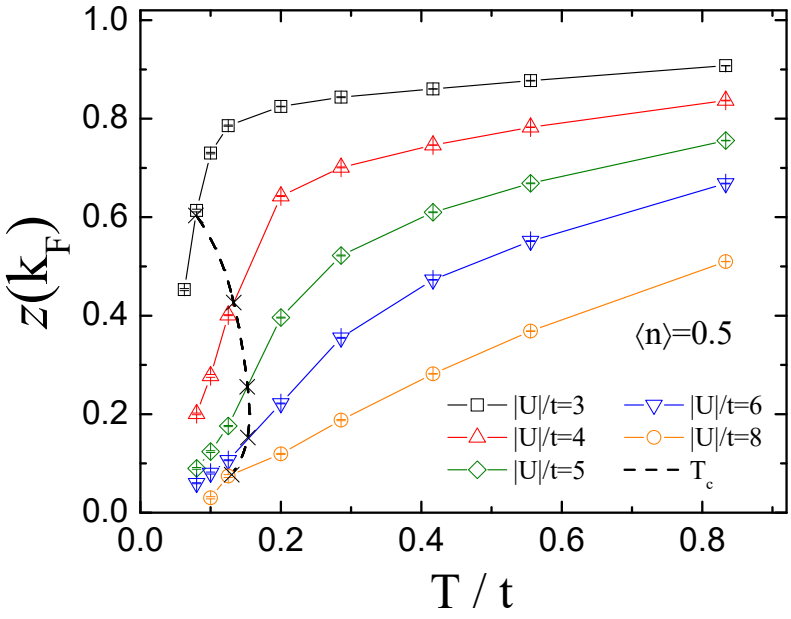

Fig. 2.12: Quasiparticle weight as a function of temperature for different values of $|U|/t$ at quarter filling. The crosses define the values of $z(k_F)$ at the respective critical temperatures, with the dashed line being a guide to the eye.

us that any attempt to identify a FL behavior for $T < T_c$ is doomed to failure, due to the opening of a superconducting gap. Nonetheless, we may draw some interesting conclusions from the behavior at $T > T_c(U)$: the decrease of the quasiparticle weight with decreasing temperature is steeper at strong coupling than at weak coupling, in line with the crossover FL-NFL alluded to in relation to Fig. 2.11. Indeed, since the effective quasiparticle mass $m^* \simeq m/z(k_F)$, where m is the bare fermionic mass, heavy quasiparticles are more strongly interacting, hence farther from the FL paradigm than light ones, or closer to NFL behavior.

2.5 Conclusions

Motivated by experimental attempts to investigate the superfluid transition of ultracold atoms in optical lattices with attractive on-site interactions, we have studied the region of optimal critical temperatures in terms of strength of interactions and fermionic density. By means of determinant quantum Monte Carlo simulations (DQMC), we have

been able to pinpoint a somewhat wide region around $|U|/t \approx 5 \pm 1$ and $\langle n \rangle \approx 0.79 \pm 0.09$ with a critical temperature $T_c \approx 0.16t$, which, under the experimental conditions reported in Ref [27], amounts to $T_c \approx 8.8$ nK. We have also examined two other temperature scales, namely the degeneracy temperature and the pairing temperature. While the degeneracy temperature describes the region below which quantum effects dominate, the pairing temperature, T_p, sets the scale for the pair formation, which is believed to be closely related to the temperature for gapped spin excitations. The fact that $T_p(U)$ does not show a strong dependence with $\langle n \rangle$ adds credence to its association with spectral properties. We have also discussed possible scenarios for a breakdown of Fermi liquid (FL) theory across the BCS-BEC crossover, through analyses of DQMC data for the distribution of double occupancy, for the momentum distribution function, and for the quasiparticle weight. The picture that emerges is that of a FL at weak coupling, which progressively breaks down when the dominant role played by unpaired fermions becomes that of mediating the interaction between tightly bound bosonic pairs. The possibility of both BCS-BEC and FL-NFL crossovers taking place within the same range of interaction strengths, though appealing, cannot be ascertained at this point.

The contents of this Chapter has already appeared as Ref. [39].

Chapter 3

Increasing superconducting T_C by layering in the attractive Hubbard model

3.1 Introduction

As much as OLE constitute an important experimental setup for studying strongly correlated phenomena, the current lowest temperatures achieved are still higher than theoretical predictions for T_c. As discussed in Chapter 2, $T_c(\langle n\rangle, U)$ display a maximum $T_c \approx 0.15t/k_B$ around $\langle n\rangle \approx 0.87$, with k_B being the Boltzmann constant, which we set to unity from now on. This corresponds to a few tens of nanokelvin, which is still about a third of the current lowest temperatures experimentally accessible in OLE [1, 27]. Hence, it is important to investigate scenarios which could lead to higher T_c's, closer to an experimentally accessible range.

As discussed in the Introduction, we may use the BCS mean-field estimate for the AHM,

$$T_c^{\mathrm{BCS}} = \widetilde{W} \exp\left(-1/D(0)|U|\right) \ , \tag{3.1}$$

as a rough guide to increase T_c. Therefore, one possibility to enhance T_c is to increase $D(0)$, while keeping fixed both the fermionic density and U. For two-dimensional systems this may be achieved by adding a second layer and adequately tuning the hopping, t_z, between the layers; see below. Note, however, that in two dimensions this is only applicable

to the doped case, since the degeneracy between charge-density wave and superconductivity suppresses T_c to zero at half-filling, by virtue of the Mermin-Wagner theorem [84]. Physically, the presence of a second layer offers another hopping channel, thus allowing pre-formed pairs to be less scattered throughout the lattice. This possibility has been explored recently by means of DQMC simulations in a metal-superconducting bilayer in Ref. [85]. We note that this degeneracy at half filling may be broken by considering a band insulating bilayer with attractive on-site interactions, thus allowing for a finite T_c [86, 87].

The possibility of a bilayer inducing a behavior different from the monolayer has been considered in the *repulsive* Fermi-Hubbard model: it was found that interplane antiferromagnetic correlations tend to enhance d-wave pairing [88, 89].

Similar arguments apply to a simple cubic lattice, where a tunable t_z could benefit from the fact that $T_c \neq 0$ for $t_z = t$ even at half filling [17]. By varying t_z between 0 and 1, we follow a dimensional crossover between two- and three dimensions. Recent OLE on Bose-Einstein condensates with Rubidium-87 atoms allowed the study of dynamical properties crossing over between 2D and 3D behavior [90]; this system can be modeled by a Bose-Hubbard model with anisotropic hopping. At this point, we note that the minimum experimentally accessible temperature in OLE is dictated by the cooling protocols used, e.g. adiabatic cooling and sympathetic cooling [91, 92, 56], and not by the dimensionality of the optical trap (2D or 3D) [93, 94, 95, 96]. Nonetheless, given that in strong-coupling the half filled (attractive or repulsive) Hubbard model can be mapped onto a Heisenberg model with antiferromagnetic exchange coupling $J = 4t^2/|U|$, a mean-field argument leads to a critical temperature $T_c \sim zJ/2$, with $z = 2d$ for d-dimensional hypercubic lattices; hence, T_c for superconductivity is expected to increase with d. Indeed, QMC simulations on the three-dimensional anisotropic repulsive Hubbard model at half-filling have found that a finite hopping between layers can enhance the magnetic structure factor relative to the 2D case, and produce a slight increase in the critical temperature [97]. In addition, a

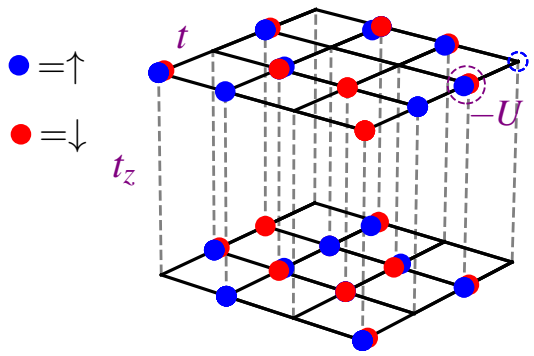

Fig. 3.1: Fermionic atoms trapped in a bilayer. Each atom can be in either an $|\uparrow\rangle$ state (blue) or a $|\downarrow\rangle$ state (red). An atom may hop to its neighboring site at a rate t within a plane, and t_z between planes. When two atoms in opposite spin states occupy the same site, the energy is lowered by $|U|$.

perturbative cluster approach to the AHM suggests that the order parameter is enhanced relative to the two-dimensional case [98].

In view of these possibilities, a systematic study of T_c for the anisotropic AHM both in the bilayer and in three dimensions is of interest. With this in mind, we have used DQMC simulations to investigate the AHM on these geometries.

The layout of this chapter is as follows. In Section 3.2 we discuss the model and highlight the main aspects of DQMC, including the quantities used to probe the physical properties of the system. In Section 3.3 we present estimates for the critical temperature as a function of interlayer hopping on a square bilayer, followed by a discussion on the pairing temperature scale. In Section 3.4, we consider the simple cubic lattice with variable interlayer hopping, t_z. In both cases we analyze the superconducting properties at different band fillings and strengths of the on-site attraction. Finally, in Section 3.5 we present our conclusions.

3.2 Model and Methodology

We write the anisotropic attractive Hubbard Hamiltonian adjusting the hopping Hamiltonian in the Hamiltonian (2.1), named here as $\mathcal{H}_{t,t_z}$,

$$\mathcal{H}_{t,t_z} = -t \sum_{\langle \mathbf{i},\mathbf{j}\rangle_{\parallel},\sigma} \left(c^{\dagger}_{\mathbf{i}\sigma} c_{\mathbf{j}\sigma} + \text{h.c.} \right) - t_z \sum_{\langle \mathbf{i},\mathbf{j}\rangle_{\perp},\sigma} \left(c^{\dagger}_{\mathbf{i}\sigma} c_{\mathbf{j}\sigma} + \text{h.c.} \right) \ , \tag{3.2}$$

where $\langle \mathbf{i}, \mathbf{j} \rangle_{\parallel}$ represents nearest-neighbor sites within a layer, and t is the intralayer hopping amplitude; t_z is the hopping energy between neighboring sites in adjacent layers $\langle \mathbf{i}, \mathbf{j} \rangle_{\perp}$ (see Fig. 3.1).

We have obtained physical quantities of interest through an unbiased DQMC numerical approach [99, 64, 65, 66, 67] (see Appendix A). In order to probe the emergence of superconductivity, we analyze the s-wave pair correlation functions,

$$C^{\Delta}_{\mathbf{ij}} \equiv \frac{1}{2}\langle b^{\dagger}_{\mathbf{i}} b_{\mathbf{j}} + \text{H.c.} \rangle, \tag{3.3}$$

with $b^{\dagger}_{\mathbf{i}} \equiv c^{\dagger}_{\mathbf{i}\uparrow} c^{\dagger}_{\mathbf{i}\downarrow}$ ($b_{\mathbf{i}} \equiv c_{\mathbf{i}\downarrow} c_{\mathbf{i}\uparrow}$) corresponding to creation (annihilation) of a pair of fermions at a given site $\mathbf{i}$. Further, the Fourier transform of $C^{\Delta}_{\mathbf{ij}}$ at $\mathbf{q} = 0$ defines the s-wave pair structure factor,

$$P_s(\mathbf{q} = 0) = \frac{1}{N} \sum_{\mathbf{i},\mathbf{j}} C^{\Delta}_{\mathbf{ij}} \tag{3.4}$$

with $N = L \times L \times L_z$ being the number of sites of the lattice, where L is the linear dimension of the 2D layers. For the bilayer, $L_z = 2$, and for the cubic lattice, $L_z = L$; periodic boundary conditions (PBC) are assumed in both cases. One should keep in mind that in Eq. (3.4) the dependence of P_s on L, U, t_z, $\langle n \rangle$, and β has been omitted, to simplify the notation.

We obtain the inverse critical temperature, $\beta_c \equiv 1/T_c$, through the correlation ratio,

$$R_c(L, \beta) = 1 - \frac{P_s(\mathbf{q} + \delta\mathbf{q})}{P_s(\mathbf{q})} \ , \tag{3.5}$$

where $\mathbf{q} = 0$, and $\delta\mathbf{q} = 2\pi/L$. As highlighted in Appendix B.2, this quantity is a renormalisation-group invariant at the critical point [100, 101, 102]; that is, crossings of curves for $R_c(L, \beta)$ for different system sizes provide estimates for β_c, which improve as L increases.

Magnetic properties are probed by the uniform susceptibility, which is given by fluctuation-dissipation theorem, $\chi_s = \beta \langle S^2 \rangle$, where $\langle S^2 \rangle$ was defined in Eqs. (2.15) and (2.16a - 2.16c).

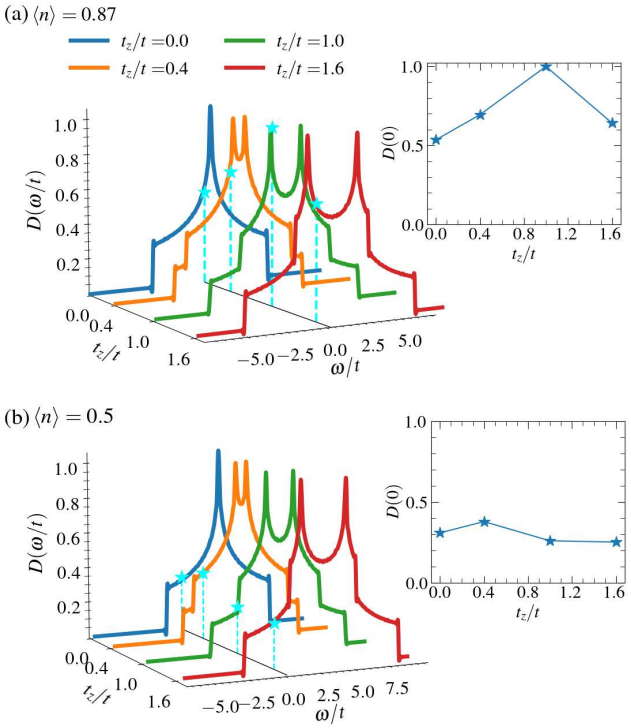

Fig. 3.2: Density of states (DOS) for the non-interacting bilayer as a function of energy, $\omega = \varepsilon - \mu(t_z)$, and interlayer hopping, t_z/t; the Fermi energy for a given electronic density is located at the origin, for (a) $\langle n \rangle = 0.87$ and (b) $\langle n \rangle = 0.5$. The cyan stars in the main panels mark $D(0)$, as plotted in the insets as functions of t_z/t.

In what follows, we separate the discussion in two parts: First, we consider a bilayer, in which case our simulations were carried out for $L \leq 16$. Subsequently, we study the actual dimensional crossover in cubic systems with $L \leq 10$. Typically our data have been obtained after $2 - 4 \times 10^4$ warming-up steps, followed by $8 - 16 \times 10^4$ sweeps for measurements, depending on the temperature, interaction strength, and electronic density. We have performed 10 to 20 realizations for each set of parameters to ensure the best accuracy for our results.

3.3 The bilayer

3.3.1 Critical temperature

We start the discussion with the non-interacting bilayer. The single-particle energies are given by

$$\varepsilon_{\mathbf{k}} = -2t \left[\cos k_x + \cos k_y\right] \pm t_z \ , \tag{3.6}$$

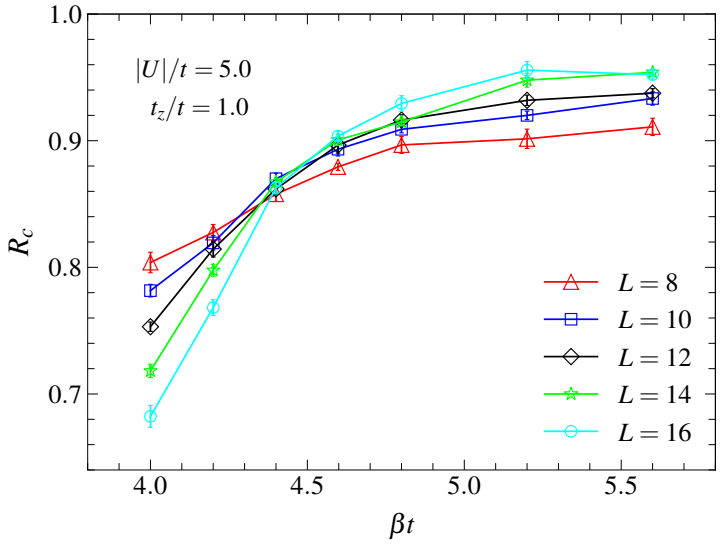

Fig. 3.3: Correlation ratio for the AHM on a bilayer, as a function of the inverse temperature, β, for isotropic hopping and $\langle n \rangle = 0.87$. Different curves are labelled by their corresponding linear lattice sizes, L.

whose DOS's are displayed in Fig. 3.2, for different densities and several values of t_z/t. For $t_z \neq 0$ the DOS may be thought of as two square lattice densities of states, displaced from each other by $2t_z$, as it can be seen from the positions of the van Hove singularities (VHS's). For instance, the insets of Fig. 3.2 (a) and (b) show the DOS at the Fermi level as a function t_z, for $\langle n \rangle = 0.87$ and 0.5, respectively: a substantial increase is found in some cases. As discussed in Chapter 1, the fine tuning of the VHS's with a single parameter opens the possibility of increasing critical temperatures.

Recalling that the global maximum T_c for the single layer lies near $\langle n \rangle = 0.87$ [39], we compare the effect of t_z on T_c both for this density and for $\langle n \rangle = 0.5$. Similarly, the maximum T_c over a wide range of densities occurs at $U = -5t$ [39], so that most of our simulations will be in the range $|U|/t = 3 - 5$. In this way, starting from the global maximum T_c one can investigate possible paths in parameter space leading to larger slopes.

A typical behavior of $R_c(L, \beta)$ is shown in Fig. 3.3 for $U = -5t$, $\langle n \rangle = 0.87$ and $t_z = t$. We clearly distinguish two regimes of β: one in which R_c decreases with increasing L,

and another in which R_c increases. The inversion takes place at the common crossing point, $\beta_c t \approx 4.5 \pm 0.1$, or $T_c/t = 0.217 \pm 0.005$; for $\langle n \rangle = 0.5$, we get $T_c/t \approx 0.217 \pm 0.009$. These values should be compared with those for the single layer, $T_c/t = 0.147 \pm 0.004$ and $T_c/t = 0.126 \pm 0.003$, respectively, with corresponding increases of 48% and 72%. Simulations for $t_z = 0.4t$ yield $T_c/t = 0.185 \pm 0.003$ and 0.200 ± 0.008, respectively for $\langle n \rangle = 0.87$ and 0.5, while for $t_z = 1.6t$, one gets $T_c/t = 0.189 \pm 0.007$ and 0.208 ± 0.008. Figure 3.4 shows these data, and we see that the maximum T_c occurs at $t_z = t$ for both fillings. Note that we have allowed interlayer hoppings to be greater than intralayer ones, i.e., $t_z > t$, to broaden the search for maximum T_c; while in OLE this would simply demand adjustments in the relative intensity or frequency of the laser beams, in materials this could be achieved by changing the pressure from hydrostatic to uniaxial. The decrease in T_c beyond the isotropic case may be attributed to an effective dimensional reduction, since hopping along the z direction becomes more favorable than hopping within the planes, thus restricting particle movement. This, in turn, may increase pair-scattering effects by lattice sites, thereby lowering the critical temperature. Note that a similar effect has been observed in a bilayer made up from a superconducting layer and a metallic layer; see, e.g. Ref. [103].

It is also instructive to compare T_c both with the BCS estimate, Eq. (1.2), and with a suggested upper bound [104]; see below. At first sight, Fig. 3.4 seems to indicate that $T_c^{\rm BCS}$ tracks T_c. However, a closer look reveals that $T_c^{\rm BCS}$ does not capture the position of maximum T_c for either densities. In addition, given that the (non-interacting) bandwidth varies with t_z, if one rescales $T_c^{\rm BCS}$ by $W = 8t + 2t_z$, the discrepancies with respect to the location of maximum T_c/t are significantly enhanced. Therefore, one cannot take $T_c^{\rm BCS}$ at face value to pinpoint actual maxima.

In order to further understand the enhancement of T_c presented in Fig. 3.4, it is worth analyzing its upper bounds, $T_c^{\rm bound}$, as proposed in Ref. [104]; see also Refs. [105, 106]. We start by recalling that the superfluid density (or helicity modulus) may be obtained

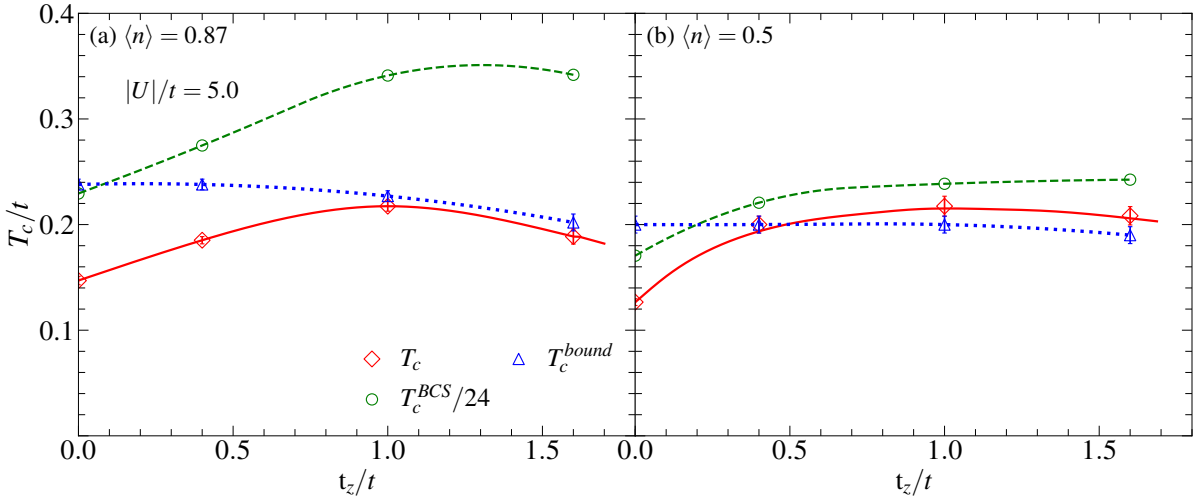

Fig. 3.4: Critical temperature, T_c/t, for the AHM on a bilayer (red diamonds), upper bound for T_c (up blue triangles) and the BCS estimate (green circles), Eq. (1.2) as a function of interlayer hopping, t_z/t, for different fermionic densities, $\langle n \rangle$, and fixed U. We have arbitrarily divided $T_c^{\rm BCS}$ [Eq. (1.2)] by 24 just to lie closer to the other curves. All lines are guides to the eye.

through [71, 72]

$$\rho_s = \frac{D_s}{4\pi e^2} = \frac{1}{4}\left[\Lambda^L - \Lambda^T\right], \tag{3.7}$$

which is proportional to the superfluid stiffness D_s. The limiting longitudinal and transverse responses are

$$\Lambda^L \equiv \lim_{q_x \to 0} \Lambda_{xx}(q_x, q_y = 0, \omega_n = 0) \tag{3.8}$$

and

$$\Lambda^T \equiv \lim_{q_y \to 0} \Lambda_{xx}(q_x = 0, q_y, \omega_n = 0), \tag{3.9}$$

with

$$\Lambda_{xx}(\mathbf{q}, \omega_n) = \sum_{\boldsymbol{\ell}} \int_0^\beta d\tau \, e^{i\mathbf{q}\cdot\boldsymbol{\ell}} e^{i\omega_n \tau} \Lambda_{xx}(\boldsymbol{\ell}, \tau), \tag{3.10}$$

where $\omega_n = 2n\pi T$ is the Matsubara frequency, and

$$\Lambda_{xx}(\boldsymbol{\ell}, \tau) = \langle j_x(\boldsymbol{\ell}, \tau) j_x(0,0) \rangle, \tag{3.11}$$

where

$$j_x(\boldsymbol{\ell}, \tau) = e^{\mathcal{H}\tau} \left[it \sum_\sigma \left(c^\dagger_{\boldsymbol{\ell}+\hat{\mathbf{x}},\sigma} c_{\boldsymbol{\ell},\sigma} - c^\dagger_{\boldsymbol{\ell},\sigma} c_{\boldsymbol{\ell}+\hat{\mathbf{x}},\sigma} \right) \right] e^{-\mathcal{H}\tau} \tag{3.12}$$

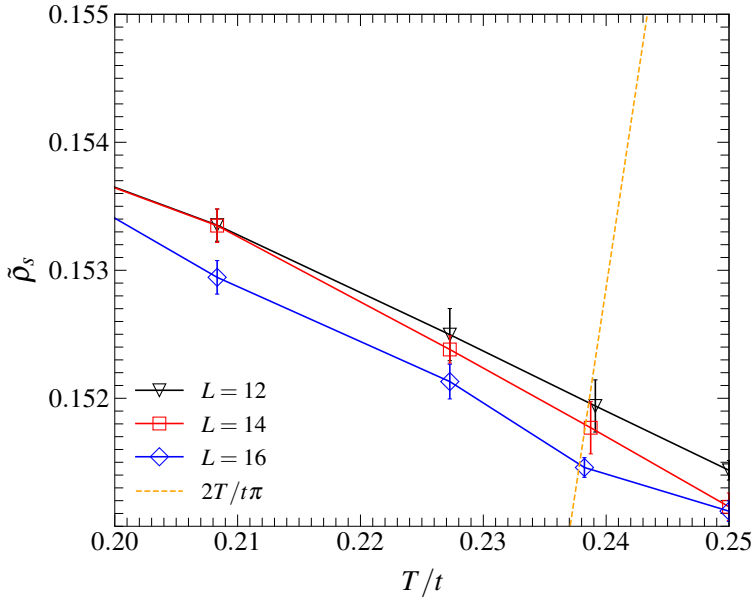

Fig. 3.5: Temperature behavior of the upper bound for the superfluid density, $\widetilde{\rho}_s$, at fixed $\langle n \rangle = 0.87$, $U/t = -5$ and $t_z/t = 0.4$, and for different lattice sizes. The intercept with the (dotted) straight line $2T/t\pi$ provides an estimate for $T_c^{\rm bound}$; see text.

is the x-component of the current density operator; see Ref. [71] for details.

Further, for a Berezinskii-Kosterlitz-Thouless (BKT) transition, a universal-jump relation involving the helicity modulus holds [73],

$$T_c = \frac{\pi}{2}\rho_s^- \tag{3.13}$$

where ρ_s^- is the value of the helicity modulus just below the critical temperature. Thus, by plotting ρ_s as a function of temperature, the intercept with $2T/\pi$ provides an estimate for T_c, as discussed in Ref. [38]. By the same token, a rigorous upper bound for the superfluid density (or, equivalently, for the superfluid stiffness) is given by [104]

$$\tilde{\rho}_s = \frac{\tilde{D}_s}{4\pi e^2} = \frac{1}{4}\Lambda^L, \tag{3.14}$$

given that Λ^T is a positive quantity [72].

Since a bilayer is topologically a two-dimensional system, the above calculational strategy used for a single layer is equally applicable to the present case. Figure 3.5 shows typical data for $\tilde{\rho}_s(T)$ obtained from our DQMC simulations, for fixed $\langle n \rangle$ and U, and different

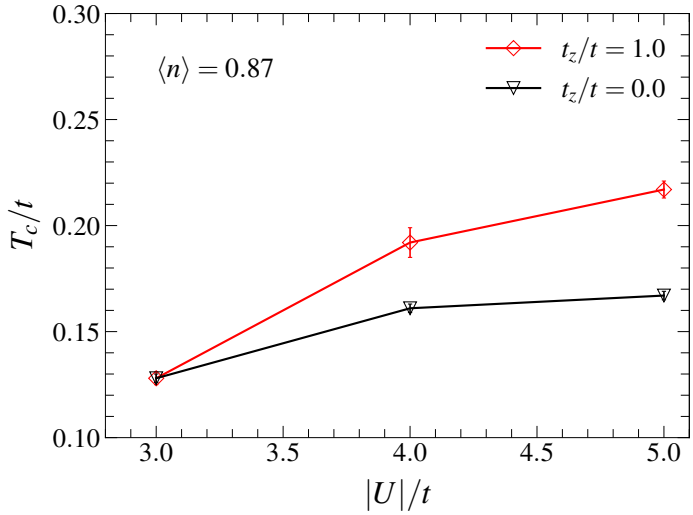

Fig. 3.6: Critical temperature as a function of the magnitude of the attractive interaction at fixed fermionic density for both the monolayer and the isotropic (i.e., $t_z = t$) bilayer. Lines are guides to the eye.

system sizes. Since $\tilde{\rho}_s \geq \rho_s$, and the superfluid density is a monotonically decreasing function of the temperature, at least near T_c (see Ref. [38]), the intercept of $\tilde{\rho}_s(T)$ with $2T/\pi$ will take place at some $T_c^{\text{bound}} \gtrsim T_c$. Figure 3.4 shows our estimates for T_c^{bound} based on this procedure, from which we see that indeed there is not much room for T_c to increase any further, in particular for $t_z \gtrsim t$.

Let us now compare how $|U|$ influences the increase in T_c in both a monolayer and an isotropic bilayer. Figure 3.6 shows T_c as a function of $|U|$, for a fixed $\langle n \rangle = 0.87$, where one may notice that the critical temperature increases faster for the bilayer ($t_z = 1$) than for the monolayer ($t_z = 0$). That is, these two curves act as lower and upper bounds for $T_c(U)$ when $0 < t_z/t < 1$. The observed increase in T_c as a function of $|U|/t$ reflects the fact that the critical temperature has not yet reached its maximum value, T_c^{max}, for the specific band filling considered. This behavior is consistent with results shown in Fig. 2.4, where for a density $\langle n \rangle = 0.87$, T_c increases with $|U|/t$ up to around $|U|/t = 5.0$, at which point T_c reaches a maximum, beyond which decreases steadily. It is also interesting to

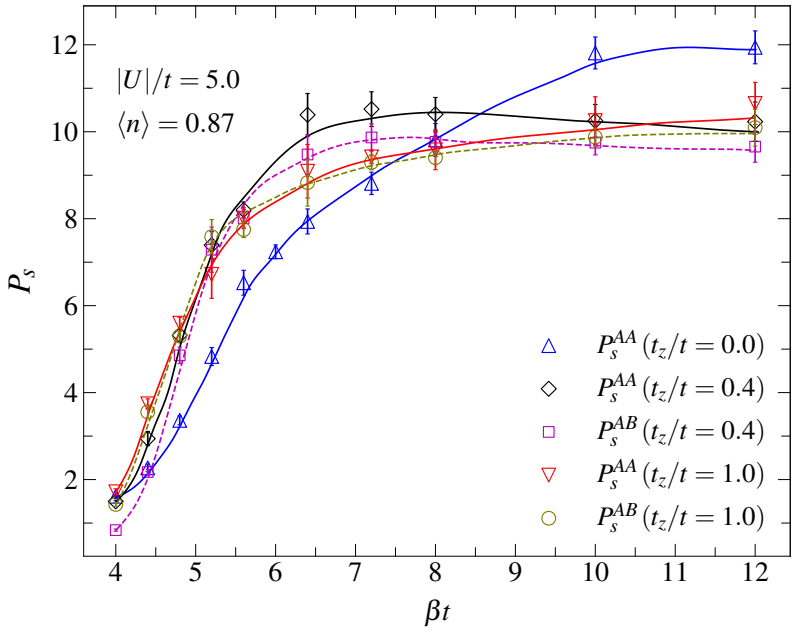

Fig. 3.7: Layer-resolved contributions to the s-wave pair structure factor as functions of the inverse temperature, βt, for different values of t_z and on an $L = 16$ bilayer. Lines are guides to the eye: full and dashed lines respectively refer to intralayer and interlayer contributions.

note that for $|U|/t = 3$, T_c is hardly influenced by the presence of a second layer.

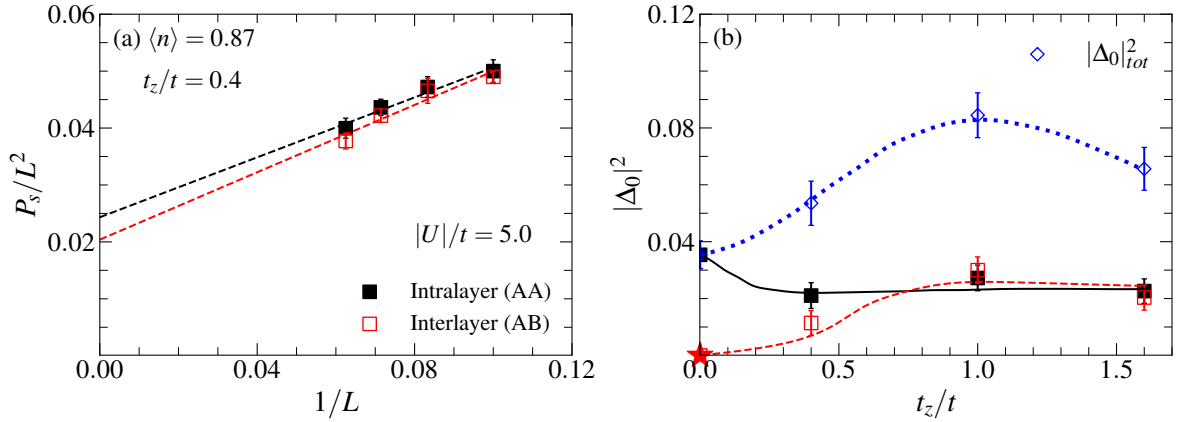

Fig. 3.8: (a) Finite-size-scaling plot for P_s, Eq. (4.4), for lattices with linear sizes $L = 12, 14$ and 16. The full and open symbols represent the intra- and inter-layer contributions to P_s. (b) The intra- (full black symbols) and inter-layer (open red symbols) contributions to the squared zero temperature gap, $|\Delta_0|^2$, as functions of t_z/t. In addition, the total $|\Delta_0|^2$, as a function of t_z/t is show (blue diamonds).

At this point, one may wonder which is the division of labor between intra- and interlayer superconducting correlations. In order to shed light into this issue, we restrict

the sums in the pair structure factor, Eq. (3.4), to sites within the same layer, call it $P_s^{\rm AA}$, and to sites joining the two layers along the z direction, $P_s^{\rm AB}$, in such way that

$$P_s = 2P_s^{\rm AA} + P_s^{\rm AB}. \tag{3.15}$$

Typical data for $P_s^{\rm AA}$ and $P_s^{\rm AB}$ as functions of the inverse temperature are shown in Fig. 3.7. By extracting similar data for other system sizes, we can plug their limiting ($\beta \to \infty$) values into the Huse scaling [107],

$$\frac{P_s}{L^2} = |\Delta_0|^2 + \frac{B}{L}, \quad L \gg 1,\ T \to 0, \tag{3.16}$$

to obtain the separate contributions to the superconducting gap at zero temperature [68, 38]; B is a non-universal constant.

Figure 3.8(a) illustrates the extrapolation to $L \to \infty$ in a scaling plot. Interestingly, when we plot the separate gaps as functions of t_z in Fig. 3.8(b) for fixed U and $\langle n \rangle$, we see that the intralayer contribution initially decreases before stabilizing in a value smaller than that for a monolayer. By contrast, the interlayer contribution rises from zero and stabilizes at roughly the same value as the one for the monolayer. Equation (4.4) allows us to add the contributions to the total $|\Delta_0|^2$, and Fig. 3.8(b) shows that the latter displays a maximum near the isotropic limit, $t_z = t$, similarly to T_c. Thus, the key point is that the correlations between layers lead to a stronger order parameter than in a monolayer, which, in turn, results in higher critical temperatures.

3.3.2 Pairing temperature scale

As mentioned in Chapter 1, one of the interesting features of the AHM is the emergence of a pairing temperature scale above T_c which signals the formation of pairs, but not their coherence. Our purpose here is to investigate how the addition of another layer affects the pairing temperature. One manifestation of pair formation is through a gap opening for spin excitations, hence as a downturn in the uniform magnetic susceptibility χ_s as the temperature is lowered [20, 16, 17, 42, 43, 39].

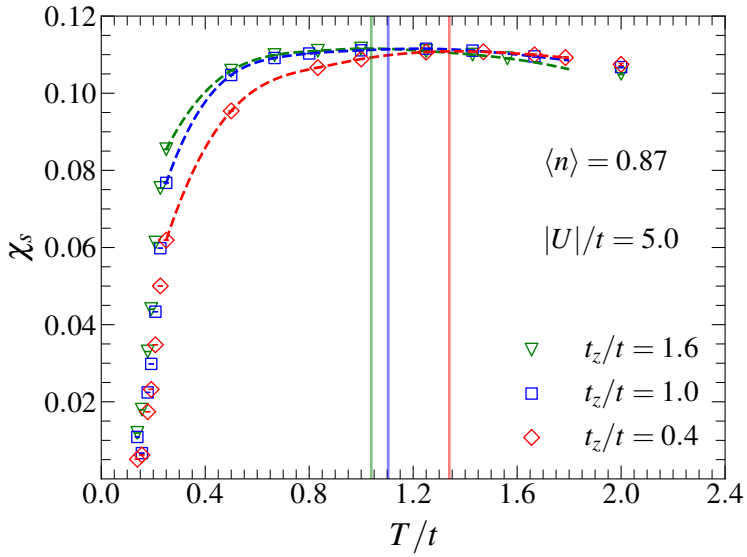

Fig. 3.9: The uniform spin susceptibility for the bilayer, as a function of temperature for $\langle n\rangle = 0.87$, $|U|/t = 5.0$, and different values of the interplane hopping t_z; the linear lattice size is $L = 16$. Dashed lines are guides to the eye, and the vertical lines indicate the temperatures at which the downturn in χ_s occurs.

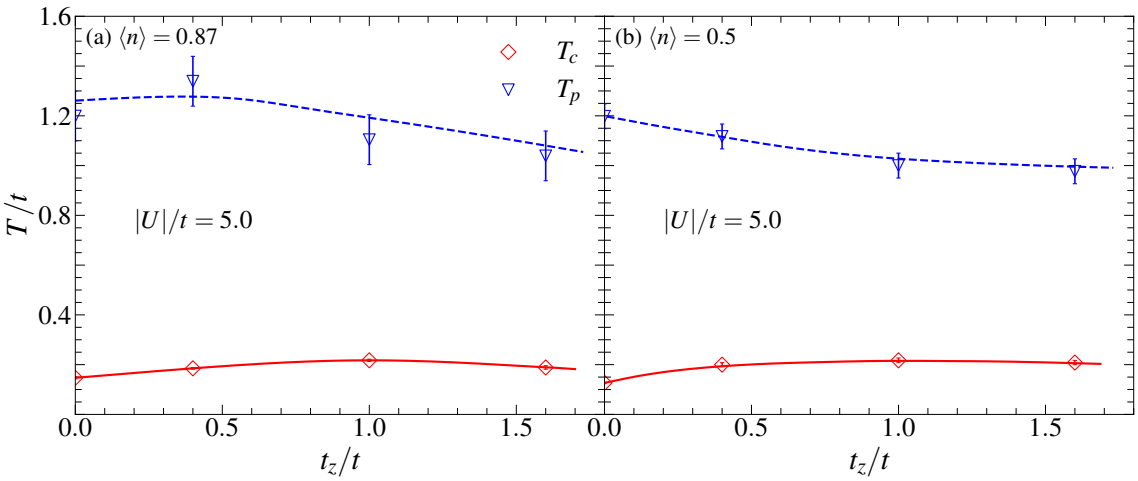

Fig. 3.10: Critical (T_c) and pairing (T_p) temperatures (in units of t) as functions of t_z/t, obtained from our DQMC simulations for a bilayer with linear size $L = 16$, and (a) $\langle n\rangle = 0.87$; (b)$\langle n\rangle = 0.5$. Lines are guides to the eye.

Figure 3.9 shows our typical DQMC data for the temperature dependence of the uniform susceptibility, χ_s [see Eq. (2.15)], for a bilayer with $|U|/t = 5.0$ and $\langle n\rangle = 0.87$, for different interplane hoppings; the linear lattice size is kept fixed at $L = 16$. We note that, for fixed U, χ_s drops steadily below some temperature, whose location depends on

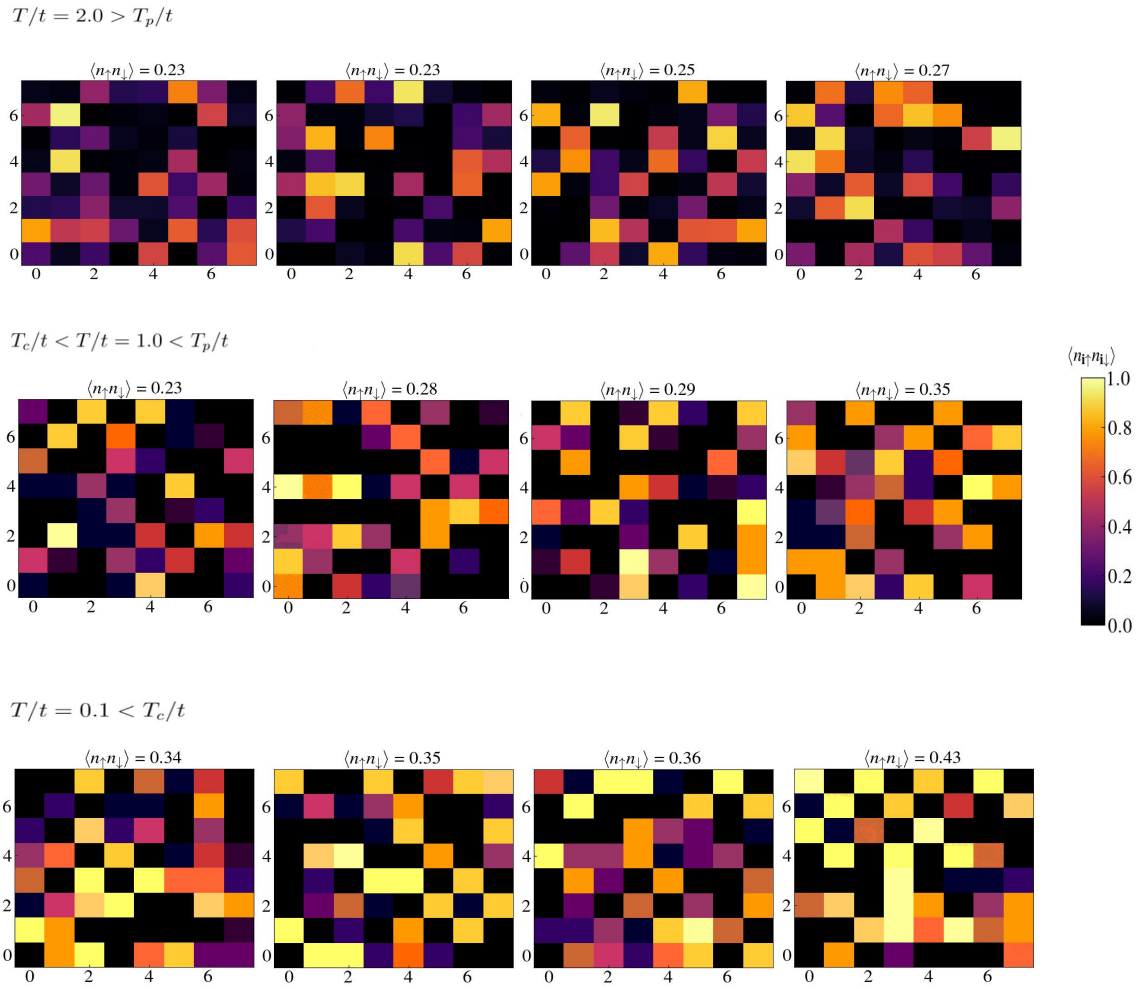

Fig. 3.11: Snapshots of the double occupancy, $d_{\mathbf{i}}$, throughout one of the layers. Labels of horizontal and vertical axes denote site coordinates on an $L = 8$ layer, for $\langle n \rangle = 0.87$, $U/t = -5$ and $t_z = t$. The rows show typical distributions at different temperatures. The calculated double occupancy for each realization appears on top of each panel, and the color map on the right hand side shows the scale for $d_{\mathbf{i}}$.

t_z. Following the idea that this drop signals the formation of local pairs within some temperature scale [16, 17, 42, 43], we adopt the position of the maximum in χ_s as the pairing scale, T_p. As Fig. 3.9 shows, for strong couplings the maxima can be quite broad, so that their position is determined by inspection of the actual numerical output for χ_s, taking into account its error bars; this yields a range of temperatures within which the maximum lies. This somewhat flexible definition is in line with the fact that we are dealing with a crossover, hence a temperature scale, not with a sharp transition.

Estimates for T_p as a function of t_z are shown in Fig. 3.10 for two different densities; for comparison, data for $T_c(t_z)$ are also shown. We see that the overall tendency of T_p is to decrease very slowly with t_z, while, as mentioned before, T_c displays a broad maximum around $t_z = t$. From this we may conclude that, to some extent, interlayer hopping favors pair breaking if they are not part of a condensate, but suppresses pair breaking if in a condensate.

We have also studied the distribution of doubly occupied sites, through

$$d_{\mathbf{i}} \equiv \langle n_{\mathbf{i}\uparrow} n_{\mathbf{i}\downarrow} \rangle, \tag{3.17}$$

and its average over the lattice sites of the bilayer,

$$\langle d \rangle \equiv \langle n_\uparrow n_\downarrow \rangle \equiv \frac{1}{N_s} \sum_{\mathbf{i}} d_{\mathbf{i}}, \tag{3.18}$$

with $N_s = 2L^2$. Figure 3.11 displays snapshots of $d_{\mathbf{i}}$ for $\langle n \rangle = 0.87$ and $|U|/t = 5.0$ for an $L = 8$ bilayer with $t_z = t$ within three ranges of temperature, namely the metallic phase, $T > T_p$, the pseudogap regime, $T_c < T < T_p$, and the superconducting phase, $T < T_c$. As expected, we see that $\langle d \rangle$ typically increases as the temperature is lowered, with the boost being more pronounced as the pairs condense into the superconducting phase. We also see that there is no significant change in the range of values of $\langle d \rangle$. By contrast, the distribution of doublons seems to follow a more pronounced checkerboard pattern in the latter case. In the superconducting phase the checkerboard pattern is even more pronounced than in the pseudogap phase, in the sense that one finds sites with large $\langle d_{\mathbf{i}} \rangle$ surrounded by sites with small $\langle d_{\mathbf{i}} \rangle$. One may attribute this to the presence of more tightly bound pairs.

3.4 The Simple Cubic lattice

Having established the quantitative influence of hopping to another layer on the critical temperature, it is instructive to compare with the behavior of the AHM on a simple cubic

lattice, but with a variable hopping along one of the directions, say the z direction, as in the bilayer. Recalling that now $T_c \neq 0$ for $t_z \neq 0$ at half filling, we will discuss this case, in addition to $\langle n \rangle = 0.87$, which is where the maximum T_c occurs for the two-dimensional case.

Starting with the non-interacting case, Fig. 3.12 shows the density of states for different values of t_z/t, and for the two fillings mentioned above. We see how the van Hove singularity at the two-dimensional particle-hole symmetry point evolves to the typical three-dimensional DOS. As a consequence, the DOS at the corresponding Fermi energies monotonically decrease with t_z/t; see the insets in each case.

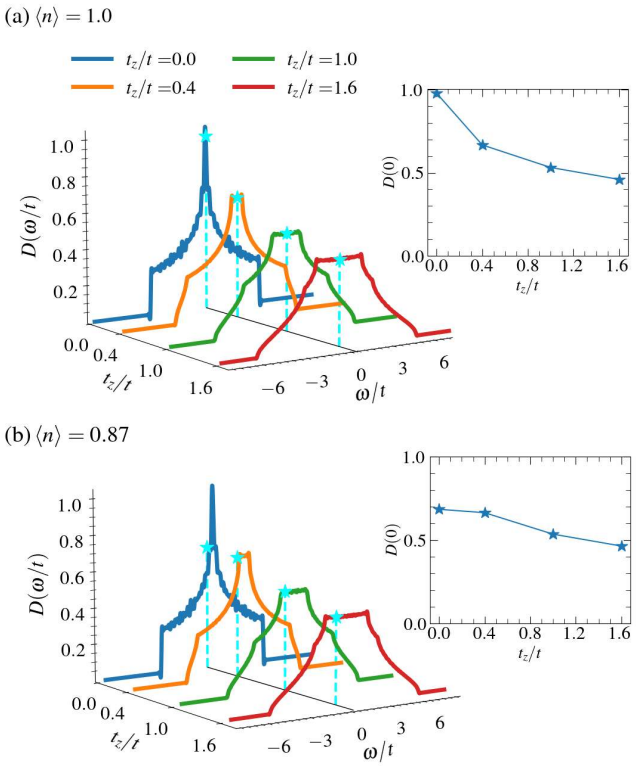

Fig. 3.12: Same as Fig. 3.2, but for a simple cubic lattice: (a) $\langle n \rangle = 1.0$ and (b) $\langle n \rangle = 0.87$.

Figure 3.13 shows the decay of pairing correlations with the distance for the cubic lattice at half filling. It is interesting to note that the length scale of decay increases by two orders of magnitude as the temperature is lowered within the interval shown, signalling the onset of superconducting long-range order. In order to estimate T_c through

our QMC simulations, we adopt a procedure similar to that for the bilayer, namely the crossing of the correlation ratio, Eq. (3.5). Typical results are shown in Fig. 3.14, and by drawing similar plots for other values of U, t_z, and $\langle n \rangle$ one determines $T_c(t_z/t)$ as displayed in Fig. 3.15. We see that for $U = -5t$ the maximum T_c occurs at $t_z = t$ for both fillings; therefore, in this case varying t_z away from the isotropic limit does not lead to higher T_c's. By contrast, for $U = -8t$ the maximum T_c occurs at larger values of t_z as the filling is decreased: there is an increase of $T_c/t = 0.34 \pm 0.01$, for $t_z = t$, from $T_c/t = 0.40 \pm 0.02$ for $t_z = 2t$, which is about 16% over the value for the isotropic case. This may be attributed to the fact that for stronger couplings the pairs are more strongly bound, hence more resistant to the suppressing effects of channelling along the z-direction.

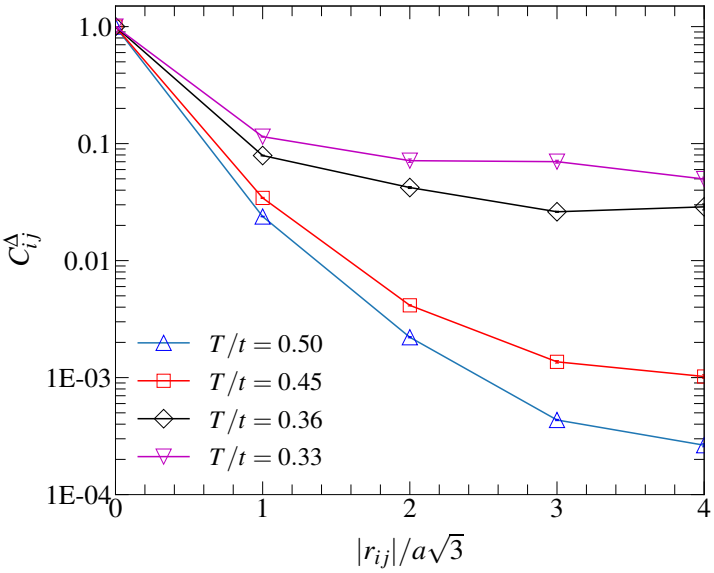

Fig. 3.13: Log-linear plot of the pairing correlation function *vs.* distance along the diagonal of an $8 \times 8 \times 8$ cubic lattice, for different inverse temperatures, βt, for a half-filled band, isotropic hopping $t_z/t = 1$, and $U/t = -8.0$. Due to periodic boundary conditions, the farthest distance is $4a\sqrt{3}$, with a being the lattice spacing.

Figure 3.15 shows that the maximum increase in T_c as $|U|$ goes from $5t$ to $8t$ is of about 50%, reachable when $t_z > 1.5t$. In addition, Fig. 3.15 also shows an interesting feature: a crossing of the $T_c(t_z/t)$ curves for small values of t_z. In order to understand this, let us focus on $\langle n \rangle = 0.87$. For the square lattice the maximum T_c occurs for $U = -5t$ [39],

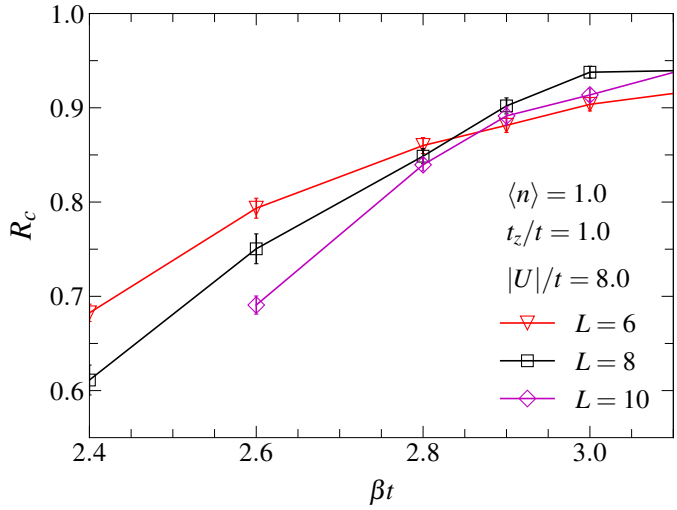

Fig. 3.14: Correlation ratio as a function of the inverse temperature, βt, for different linear cubic lattice sizes. The inverse critical temperature is estimated as $\beta_c t = 2.85 \pm 0.05$.

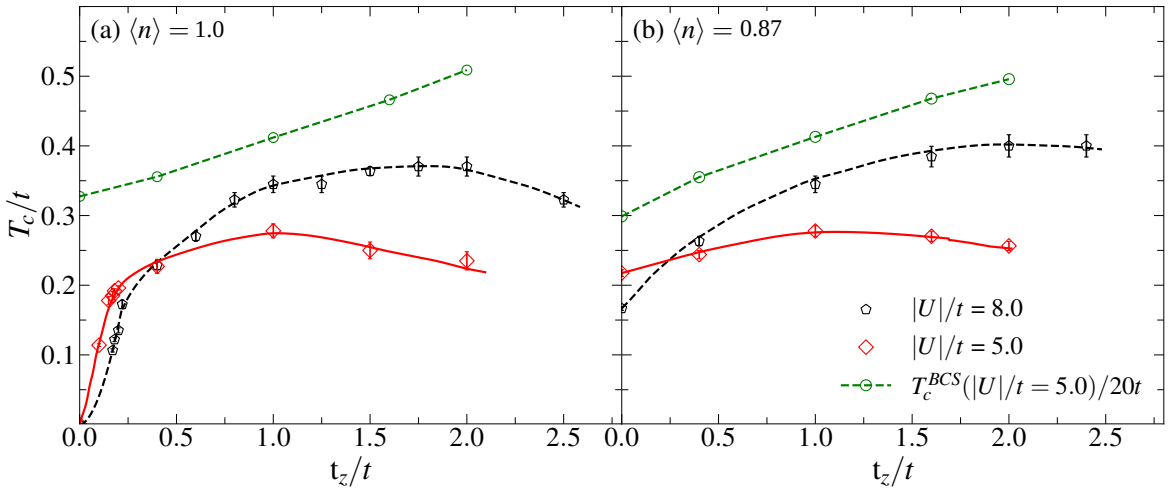

Fig. 3.15: DQMC estimates for the 3D critical temperature, T_c, as a function of t_z/t: (red) diamonds and (black) pentagons correspond to $U = -5t$ and $U = -8t$, respectively; scaled data for $T_c^{\rm BCS}$, Eq. (1.2), for $U = -5t$, are shown as (green) circles. We have arbitrarily divided $T_c^{\rm BCS}$ by 20 just to lie closer to the other curves. The panels correspond to the densities shown. All lines are guides to the eye.

namely $T_c \approx 0.22t$, while for $U = -8t$, $T_c \approx 0.16t$; see data for $t_z = 0$ in Fig. 3.15(b). On the other hand, for the isotropic simple cubic lattice the maximum T_c occurs for $|U|/t \gtrsim 8$, as it can be inferred from the data for $\langle n \rangle = 0.8$ in Ref. [17]. The crossing is therefore a consequence of the dimensional crossover driven by t_z. In other words, the crossing at

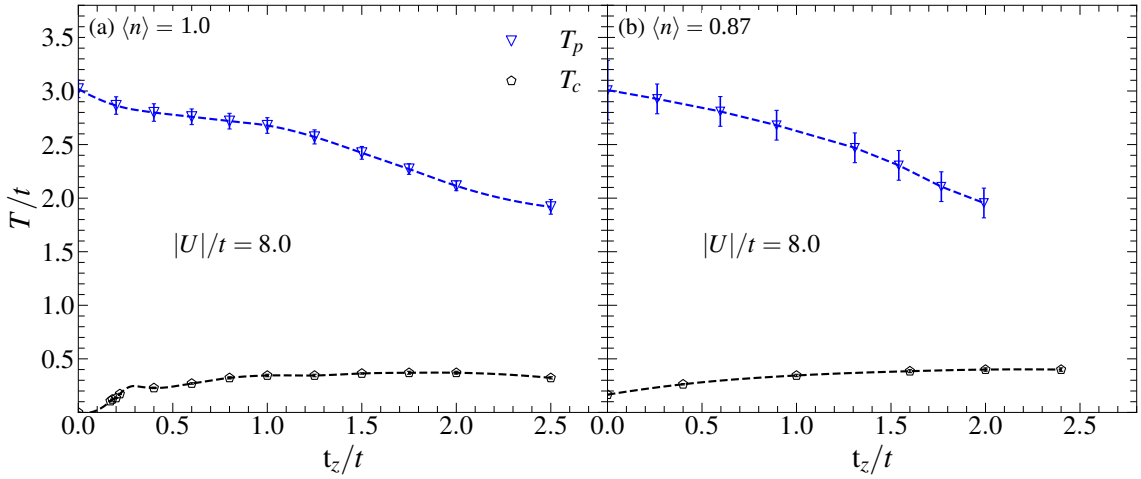

Fig. 3.16: Critical, T_c, and pairing, T_p, temperatures (in units of t) as functions of t_z/t, obtained from our DQMC simulations for a cubic lattice with linear lattice size $L = 8$, at (a) half filling and (b) for $\langle n \rangle = 0.87$, for $|U|/t = 8.0$. Dashed lines are guides to the eye.

$t_z \approx 0.25t$ for $\langle n \rangle = 0.87$ seems to separate two regimes: one in which interplane pairing correlations are significantly less relevant than the intraplane ones. Similar arguments should also account for the crossing at half filling, despite the fact that T_c is suppressed to zero for $t_z = 0$.

Similarly to what we did for the two-dimensional geometries, we now probe the effectiveness of the BCS estimate for the anisotropic simple cubic lattice. Figure 3.15 compares the dependence of T_c/t and $T_c^{\rm BCS}/W$ with t_z/t, for fixed $U = -5t$, and for two densities; $W = 8t + 4t_z$ is the bandwidth. At half filling, $T_c^{\rm BCS}$ does not satisfy the Mermin-Wagner theorem for $t_z = 0$, as expected. In addition, one sees that $T_c^{\rm BCS}$ does not track our DQMC estimates for T_c for both fillings.

Let us now discuss how the pairing temperature is affected by a variable hopping along the z-direction. Our DQMC data are shown in Fig. 3.16 for fixed $U = -8t$, and for different fillings; T_c is also plotted for comparison. We see that T_p decreases much more steadily with t_z than for the bilayer; this leads one to conclude that confinement along the z-direction favors pair formation, but not necessarily pair condensation. The data also show that the behavior of T_p with t_z is not too dependent on $\langle n \rangle$ within the range

considered.

And, finally, Fig. 3.17 compares the effect of anisotropy on T_c for both the bilayer and the simple cubic lattice. We see that away from half filling T_c is about 30% higher for the 3D lattice.

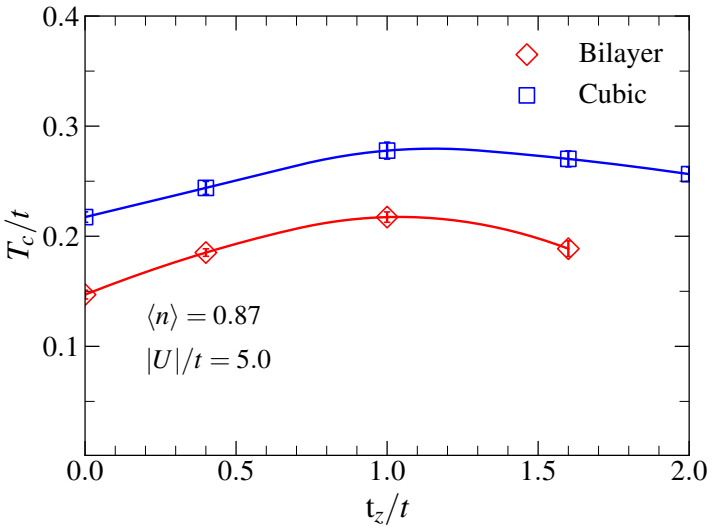

Fig. 3.17: Comparison of our DQMC data for T_c on the bilayer and on the simple cubic lattice.

3.5 Conclusions

In this Chapter we have examined layering as a possible route to increase the superconducting critical temperature in the attractive Hubbard model.

In two dimensions, layering consists of stacking two planes with hopping t_z between them; intra-plane hoppings and on-site attraction are the same in both planes. We have found that by a judicious choice of fillings and on-site attraction, a bilayer can exhibit critical temperatures between 1.5 and 1.7 times those of the single layer. We have also established that double occupancy can be used to distinguish between normal (metallic), pre-formed pairs (pseudogap), and superconducting phases through quantum gas microscope measurements.

For a simple cubic lattice, layering consists of allowing t_z to vary with respect to the

isotropic case, $t_z = t$, but the number of planes along the z direction, L_z, is the same as the number of sites, $L_x = L_y$, along the planar directions. We have found a smaller enhancement of T_c relative to the isotropic case, namely of 1.3 times larger, for some specific choices of t_z, U and $\langle n \rangle$.

For both geometries, we have found that the BCS estimate roughly tracks the DQMC T_c's, although the positions of T_c maxima are not reliable; less serious is the multiplicative factor of order 20 for both geometries, since the unknown proportionality factor in Eq. (1.2) could account for it. In addition, since T_c^{BCS} does not follow the Mermin-Wagner theorem this discrepancy at half-filling in 3D is even more serious for $t_z \lesssim 0.5t$. Also, care must be taken since the BCS estimate for T_c scales with the bandwidth, which, in turn, depends on t_z; this leads to more severe discrepancies in bilayer than in 3D.

We hope our results will stimulate optical lattice experiments to explore this route of layering to further increase T_c.

This work has been published as Ref. [45].

Chapter 4

Effects of next-nearest neighbor hopping on the pairing and critical temperatures of the attractive Hubbard model on a square lattice

4.1 Introduction

One of the experimental challenges in the study of the AHM on a square lattice concerns the critical temperature, which is far from the accessible experimental temperature range. Thus, a natural question is whether we can generate a high superconducting temperature, while having the system strictly two-dimensional. In Chapter 3, we saw that, based on the BCS argument, Eq. (1.2), we can produce an increase in critical temperature T_c, by increasing $D(0)$.

Here we examine this possibility by allowing for both nearest, t, and next-nearest-neighbor (NNN) hopping, t', so that fermions may also move along the diagonals of a square lattice. This provides an additional channel for Cooper pairs to move around, avoiding pair-breaking scattering events by lattice sites. Figure 4.1 shows the non-interacting density of states for $\langle n \rangle = 0.87$ (the density for which T_c in the AHM is maximum over a range of values of U), for both $t' = 0$ and $t' = -0.2t$; the corresponding Fermi levels sit at $\omega \equiv \varepsilon(\mathbf{k}) - \mu = 0$, with the dispersion $\varepsilon(\mathbf{k})$ given by Eq. (4.1), and are indicated by the

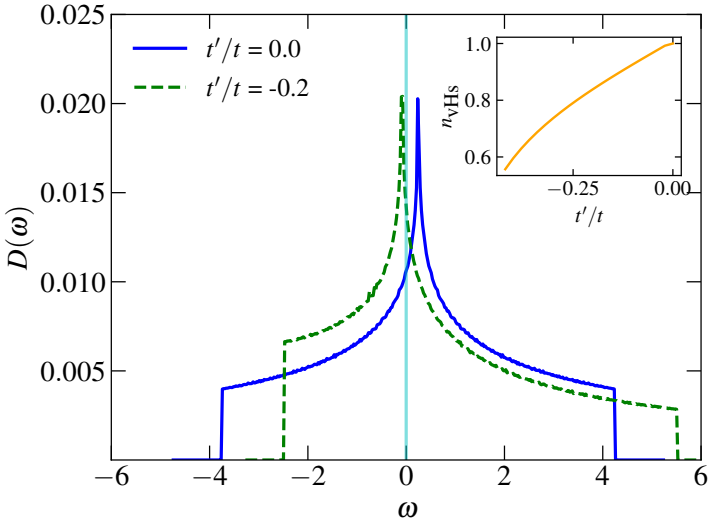

Fig. 4.1: Non-interacting density of states as a for $t' = 0$ and $t' = -0.2t$. The vertical lines locate the corresponding Fermi energies for $\langle n \rangle = 0.87$. The inset shows the electronic density at which the van Hove singularity occurs, n_{vHS}, as a function of t'/t.

vertical lines. We see that for this filling $D(0)$ is larger for $t' = -0.2t$, which, according to Eq. (1.2), suggests a T_c higher than for $t' = 0$. This picture is supported by perturbative approaches [108] and by early QMC simulations for limited sets of parameters [109, 46], both showing an enhancement of superconducting pairing correlations for a finite t'. In addition, Ref. [110] has explored analytically and numerically the effects of an additional hopping channel on modulation instability and breather dynamics in 2D ultracold atoms, which is described within the Hubbard model framework. Note, however, that in two dimensions this is only applicable to the doped case, since the degeneracy between charge ordering and superconductivity suppresses T_c to zero, by virtue of the Mermin-Wagner theorem [84]. Further, with second neighbor hopping the non-interacting band can become flatter than for $t' = 0$. Indeed, Fig. 4.2 shows the single-particle band,

$$\varepsilon(\mathbf{k}) = -2t\,[\cos k_x + \cos k_y] - 4t' \cos k_x \cos k_y, \tag{4.1}$$

and the flattening for $t' = -0.2t$ is significant. Flat bands tend to enhance electronic correlations in the presence of interactions, thus giving rise to a more robust superconducting state [111, 112, 113, 114].

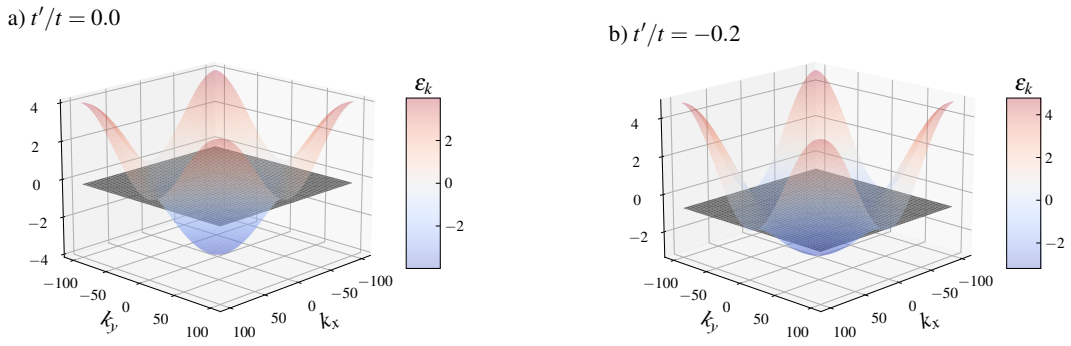

Fig. 4.2: Band dispersion, Eq. (4.1) for (a) $t'/t = 0.0$ and (b) $t'/t = -0.2$. The gray planes locate the Fermi energy for $\langle n \rangle = 0.87$.

From an experimental point of view, we note that a triangular optical lattice has been set up experimentally by adding an extra pair of counter-propagating laser beams; see Ref. [115]. Given that the triangular lattice may be thought of as a square lattice with hopping along one of the diagonals, a possible route to generate NNN hopping on a square lattice would be to add yet another pair of counter-propagating laser beams, this time along the other diagonal direction.

In view of these possibilities, a systematic study of the effects of NNN hopping on the critical temperature of the AHM is of interest. With this in mind, here we use DQMC simulations to map out how much can T_c be enhanced by second neighbor hopping for different values of the attractive interaction and band filling. In addition, we also explore the behavior of the pairing temperature with t'.

Thus, here we report on results from Monte Carlo simulations for AHM with an additional NNN hopping channel. The layout of this chapter is as follows: In Section 4.2 we discuss the model and highlight the main aspects of DQMC, including the quantities used to probe the physical properties of the system. In Sec. 4.3 we present our main results for the critical temperature and for the pairing temperature as functions of the NNN hopping amplitude. Section 4.4 summarizes our findings.

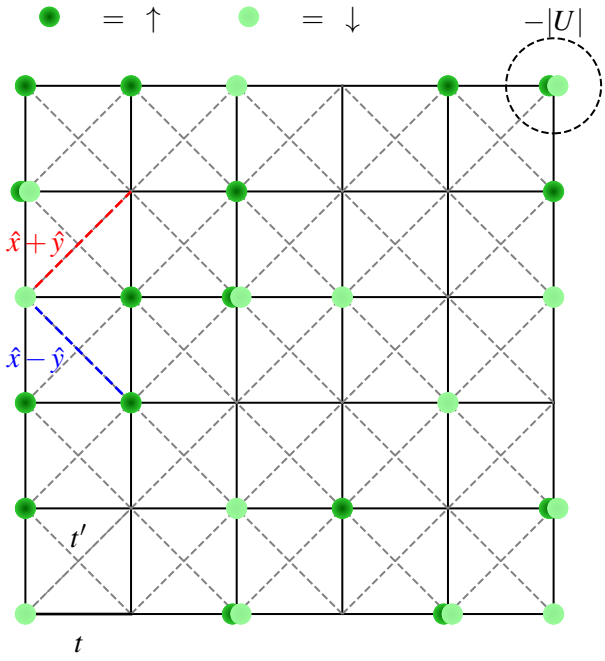

Fig. 4.3: Typical portion of a square lattice illustrating the model parameters. Two fermions with opposite spins on the same site contribute with $-|U|$ to the total energy. Fermions hopping between nearest-neighboring sites (horizontally, $\hat{\mathbf{x}}$, or vertically, $\hat{\mathbf{y}}$) contribute with $-t$ (full lines) to the total energy. Fermions hopping along the diagonals, $\hat{\mathbf{x}}\pm\hat{\mathbf{y}}$, contribute with $-t'$ (dashed lines) to the total energy.

4.2 Model and Methodology

We consider the attractive Hubbard Hamiltonian (2.1) with second-neighbor hopping [108, 109, 116], where the different hopping processes are describes by the tight-binding Hamiltonian,

$$\mathcal{H}_{t,t'} = -t \sum_{\langle \mathbf{i},\mathbf{j}\rangle,\sigma} \left(c^{\dagger}_{\mathbf{i}\sigma} c_{\mathbf{j}\sigma} + \text{h.c.} \right) - t' \sum_{\langle\langle \mathbf{i},\mathbf{j}\rangle\rangle,\sigma} \left(c^{\dagger}_{\mathbf{i}\sigma} c_{\mathbf{j}\sigma} + \text{h.c.} \right) \tag{4.2}$$

with,

$$t_{\mathbf{i},\mathbf{j}} = \begin{cases} t, & \text{if } \mathbf{i},\, \mathbf{j} \text{ are nearest neighbors (NN)}, \\ t', & \text{if } \mathbf{i},\, \mathbf{j} \text{ are next-nearest neighbors (NNN)}\ , \\ 0, & \text{otherwise;} \end{cases} \tag{4.3}$$

where $\langle \mathbf{i},\mathbf{j}\rangle$ and $\langle\langle \mathbf{i},\mathbf{j}\rangle\rangle$ respectively restrict hoppings between nearest- and next-nearest neighboring sites on a square lattice, with amplitudes t and t'; 'h.c.' stands for hermitian conjugate of the previous expression. Fig. 4.3 shows a picture of fermions with opposite spins moving on a square lattice, where red and blue dashed lines correspond to two non-equivalent NNN hopping direction by symmetries. The on-site double occupancy is represented by a dashed circle.

Through DQMC simulations [99, 64, 65, 66, 67], we investigate the finite temperature properties of this model. In order to probe the emergence of superconductivity, we analyze the s-wave pair correlation functions [Eq. (2.2)], where the decay of $C^{\Delta}_{\mathbf{ij}}$ with the distance $r_{\mathbf{ij}} \equiv |\mathbf{i}-\mathbf{j}|$ probes the resilience of pair coherence at a given temperature.

In addition, the Fourier transform of $C^{\Delta}_{\mathbf{ij}}$ at $\mathbf{q}=0$ defines the s-wave pair structure factor, Eq. (2.4), with $N = L \times L$ being the number of sites of the lattice, where L is the linear lattice size; periodic boundary conditions (PBC) are imposed. The finite-size scaling behavior of P_s is therefore obtained upon integration of $C^{\Delta}_{\mathbf{ij}}$ over a two-dimensional system of linear dimension L [68, 38], Eq. (2.6), and so, given that the system displays long-range order in the ground state, a 'spin-wave scaling' holds [107],

$$\frac{P_s}{L^2} = |\Delta_0|^2 + \frac{B}{L}, \tag{4.4}$$

where Δ_0 is the superconducting gap function at zero temperature, and B is a $|U|$-dependent constant.

We have estimated the critical temperature, T_c, in two different ways: first, we perform an analysis through the correlation ratio, Eq. (3.5); and then, we use the universal-jump relation, Eq. (2.14), to obtain the superconducting critical temperature. It is important to highlight that, since we have an additional next-nearest-neighbor hopping channel, we rewrite the current density operator, which is taken in Eq. (3.11), as

$$\begin{aligned}\mathbf{J}(\boldsymbol{\ell}) = \frac{t}{2} \sum_{\substack{\hat{\delta}\in\{\hat{\delta}\} \\ \sigma}} \hat{\delta} \left(i c^{\dagger}_{\boldsymbol{\ell}+\hat{\delta},\sigma} c_{\boldsymbol{\ell},\sigma} + \text{H.c.} \right) \\ + \frac{t'}{2} \sum_{\substack{\hat{\delta}'\in\{\hat{\delta}'\} \\ \sigma}} \hat{\delta}' \left(i c^{\dagger}_{\boldsymbol{\ell}+\hat{\delta}',\sigma} c_{\boldsymbol{\ell},\sigma} + \text{H.c.} \right) \ .\end{aligned} \tag{4.5}$$

where $\left\{\hat{\delta}\right\}$ and $\left\{\hat{\delta}'\right\}$ include all unitary displacements for nearest and next-nearest neighbor sites, namely $\left\{\hat{\delta}\right\} = \{\pm\hat{x},\ \pm\hat{y}\}$ and $\left\{\hat{\delta}\right\} = \{\pm\hat{x}\pm\hat{y},\ -\hat{x}+\hat{y},\ \hat{x}-\hat{y}\}$; see Fig. 4.3. Thus, we can write

$$j_x(\boldsymbol{\ell},\tau) = e^{\mathcal{H}\tau} \left[\mathbf{J}(\boldsymbol{\ell})\cdot\hat{x}\right] e^{-\mathcal{H}\tau} \ , \tag{4.6}$$

see Ref. [71] for details.

Gauge invariance requires that the longitudinal part of Λ satisfies the equality [71],

$$\Lambda^L \equiv \lim_{q_x \to 0} \Lambda_{xx}(q_x, q_y = 0, \omega_n = 0) = -K_x \tag{4.7}$$

where K_x is the kinetic energy contribution relative to the x direction,

$$\begin{aligned} K_x = \Big\langle & -t \sum_{\sigma} \left(c^{\dagger}_{\boldsymbol{\ell}+\hat{\mathbf{x}},\sigma} c_{\boldsymbol{\ell},\sigma} + c^{\dagger}_{\boldsymbol{\ell},\sigma} c_{\boldsymbol{\ell}+\hat{\mathbf{x}},\sigma} \right) \\ & - t' \sum_{\sigma} \left(c^{\dagger}_{\boldsymbol{\ell}'+\hat{\mathbf{x}}'+\hat{\mathbf{y}}',\sigma} c_{\boldsymbol{\ell}',\sigma} + c^{\dagger}_{\boldsymbol{\ell}',\sigma} c_{\boldsymbol{\ell}'+\hat{\mathbf{x}}'+\hat{\mathbf{y}}',\sigma} \right) \\ & - t' \sum_{\sigma} \left(c^{\dagger}_{\boldsymbol{\ell}'+\hat{\mathbf{x}}'-\hat{\mathbf{y}}',\sigma} c_{\boldsymbol{\ell}',\sigma} + c^{\dagger}_{\boldsymbol{\ell}',\sigma} c_{\boldsymbol{\ell}'+\hat{\mathbf{x}}'-\hat{\mathbf{y}}',\sigma} \right) \Big\rangle \ , \end{aligned} \tag{4.8}$$

in which we take into account both NN and NNN contributions.

We will also discuss the behavior of a pairing temperature scale, T_p, which may be signalled by a gap opening for spin excitations, hence as a downturn in the uniform magnetic susceptibility χ_s as the temperature is lowered [20, 16, 17, 42, 43, 39]. We recall that, the uniform susceptibility is obtained through the fluctuation-dissipation theorem, where $\chi_s = \beta \langle S^2 \rangle$, where $\langle S^2 \rangle$ was defined in Eq. (2.15) and (2.16a - 2.16c).

Our simulations were carried out on $L \times L$ lattices, with $L \leq 20$. Typically our data have been obtained after $5 - 10 \times 10^3$ warming-up steps, followed by $2 - 6 \times 10^5$ sweeps for measurements, depending on the temperature, interaction strength, and electronic density.

4.3 Results and Discussions

4.3.1 Pairing Correlations

Figure 4.4 compares the decay with distance of the pairing correlation function, Eq. (2.2), for both $t' = 0$ and $t' \neq 0$. The behavior is similar in both cases, namely at high temperatures the fast decay of C^{Δ}_{ij} reflects the lack of pair coherence along the lattice. The situation changes completely at low temperatures, $\beta t \gtrsim 6.8$, beyond which

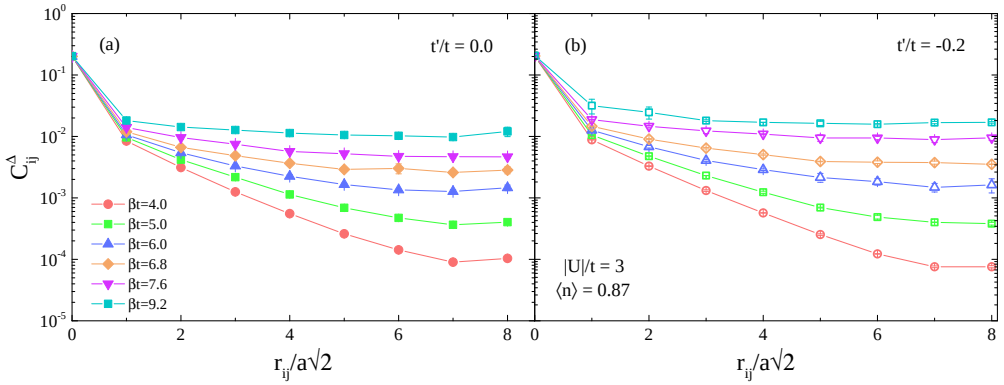

Fig. 4.4: (Color online) Log-linear plot of the decay with diagonal distance of the pairing correlation function for different temperatures, at fixed $U/t = -3$, electronic density $\langle n \rangle = 0.87$, for (a) $t'/t = 0$, and (b) $t'/t = -0.2$.

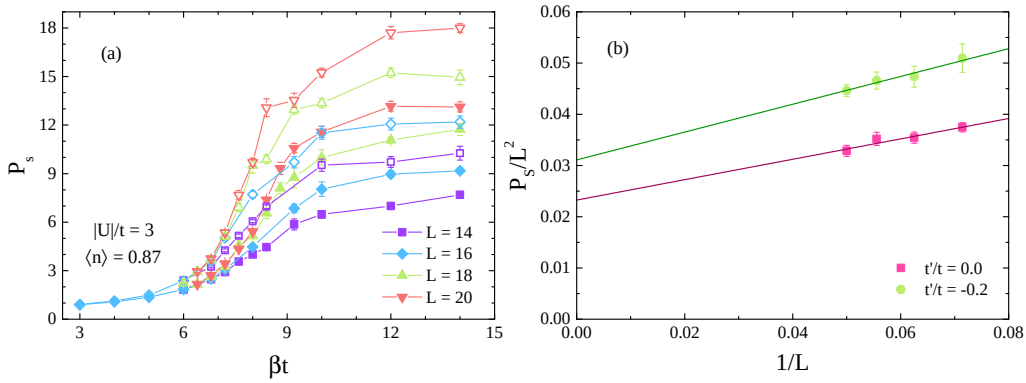

Fig. 4.5: (Color online) Pair structure factor P_s as a function of inverse of temperature, for different lattice sizes. The full symbols correspond to $t'/t = 0$ results, while the empty symbols to $t'/t = -0.2$ ones.

the correlations decay at a much lower rate, consistent with long-range superconducting order in the ground state. Further, a closer look at the data seems to indicate that $C_{ij}^{\Delta}(\mathbf{r}_{ij})$ stabilizes at a slightly larger value for $t' = -0.2t$ than for $t' = 0$. In order to check this, Figure 4.5(a) shows the s-wave structure factor, P_s [Eq. (2.4)], as a function of the inverse temperature, βt. We see that all data stabilize at low temperatures, at values which increase with the system size, consistently with order in the ground state. In addition, for a given system size, the data for $t' = -0.2t$ stabilize at larger values than those for $t' = 0$.

This can be cast into a more quantitative basis by performing a finite-size scaling

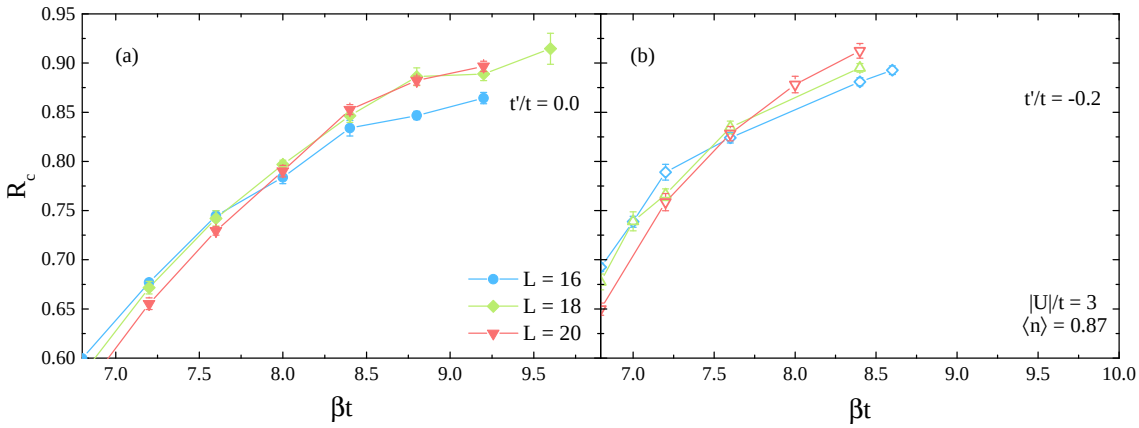

Fig. 4.6: (Color online) The correlation ratio R_c as a function of the inverse of temperature, for different lattice sizes, and fixed (a) $t'/t = 0.0$, and (b) $t'/t = -0.2$. In both panels we have $\langle n \rangle \approx 0.87$, and $U/t = -3$.

(FSS) analysis of P_s; see Eq. (4.4). The low-temperature stabilized values of P_s at large β's, extracted from Fig. 4.5(a), are divided by L^2 and plotted in Fig. 4.5(b) as functions of $1/L$. The intercepts with the vertical axis provide estimates for Δ_0^2; these, in turn, are larger for $t' = -0.2t$ than for $t' = 0$, consistently with a more robust pairing. Therefore, if one assumes the proportionality between Δ_0 and T_c, from the BCS theory, we may expect an increase of T_c when t' is turned on.

4.3.2 Critical temperature

We first estimate the possible increase of critical temperature, T_c, through the correlation ratio, R_c, Eq. (3.5). Figure 4.6 shows the temperature dependence of $R_c(L)$ for $t' = 0$ [panel (a)] and for $t'/t = -0.2$ [panel (b)], for three different system sizes. For sufficiently large system sizes, the curves should cross at a single point, β_c. However, for the sizes considered here these crossings occur at slightly different values of β: while for $t'/t = 0.0$ the intersection occurs at $\beta t \approx 8.0 \pm 0.2$ ($T_c/t \approx 0.125 \pm 0.003$), for $t'/t = -0.2$ we estimate $\beta t \approx 7.5 \pm 0.2$ ($T_c/t \approx 0.133 \pm 0.004$). That is, T_c for the NNN hopping case is slightly enhanced with respect to the NN hopping.

In order to obtain a more complete diagram of $T_c \times t'$, we employ a more robust analysis

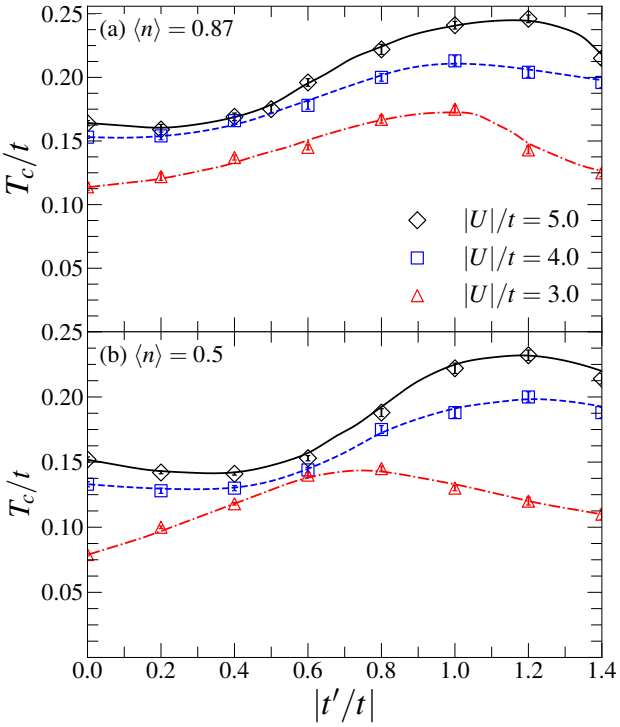

Fig. 4.7: Critical temperature as a function of NNN hopping amplitude, for different values of the attractive interaction, for (a) $\langle n \rangle = 0.87$, and (b) $\langle n \rangle = 0.5$. The lines through the points are guides to the eye, and the error bars are smaller than the data points.

of T_c for an extensive range of t', $|U|/t$, $\langle n \rangle$, using the jump relations in Eq. (2.14). Figure 4.7(a) shows the behavior of the critical temperature as a function of $|t'/t|$, for different values of U and fixed $\langle n \rangle = 0.87$. For all values of interaction strength we analyzed, there is an increase in T_c relative to its value for $t' = 0$, T_c^0. Interestingly, the maximum T_c occurs at slightly different values of t' when varying $|U|/t$. For the values of U shown, the maximum critical temperature, $T_c(\langle n \rangle, |U|/t) = 0.246 \pm 0.003$, is reached for $|U|/t = 5.0$ and $t' = -1.2t$. This represents a 50% increase compared with the corresponding T_c^0. Similar results are obtained at quarter-filling, as shown in Fig. 4.7(b), with a maximum $T_c(\langle n \rangle, |U|/t) = 0.232 \pm 0.003$ at $t' = -1.2t$; again an increase of about 50% over the value for $t' = 0$. Overall, we see that T_c increases with $|U|$, with t' controlling how much the increase in T_c is relative to the value when $t' = 0$.

At this point, it is instructive to examine the behavior of the non-interacting DOS and

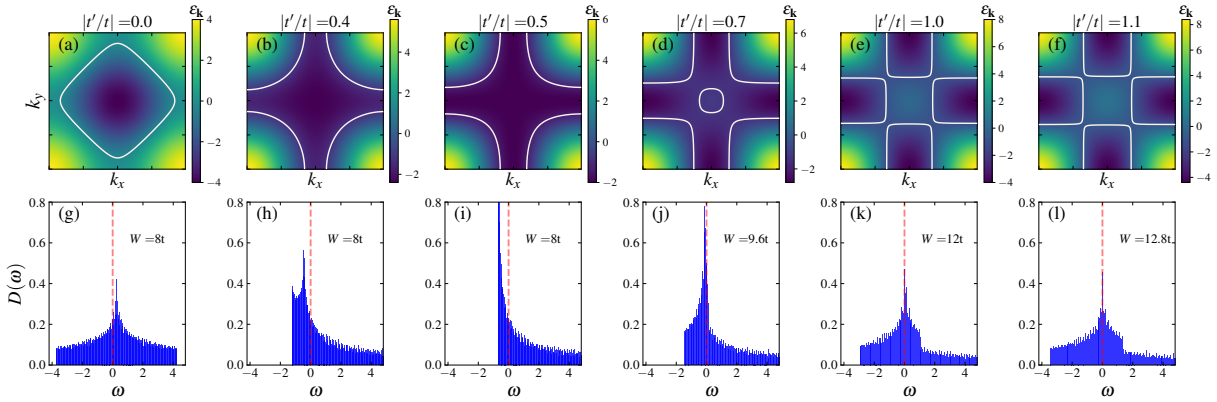

Fig. 4.8: (a)-(f): Contour map of the single-particle dispersion, $\varepsilon_{\mathbf{k}}$, for different values of t'/t; in each panel, the Fermi surface for $\langle n \rangle = 0.87$ is shown as a white line. (g)-(l): corresponding evolution of the density of states; the dashed red vertical lines locate the corresponding Fermi energies.

Fermi surface for different values of t'. For instance, Figs. 4.8(a)-(f) show the evolution of the Fermi surface with t' for $\langle n \rangle = 0.87$, where one may notice a change from an electron-like behavior to a hole-like one as $|t'|$ increases. The corresponding evolution of the density of states is shown in Figs. 4.8(g)-(l), from which one also notices that for $|t'/t| \leq 0.5$, $D(0)$ is approximately constant, and in the interval $0.7 \lesssim |t'/t| \leq 1.1$ $D(0)$ lies at, or very close to, a van Hove singularity. We can therefore resort to Eq. (1.2) to explain the slow increase of T_c with t' in the former interval, and a faster increase in the latter, as shown in Fig. 4.7(a). Also, this increase above $|t'/t| \approx 0.6$ is faster for larger $|U|$. Another interesting aspect emerging from Fig. 4.8 is that the bandwidth is constant up to $|t'| = 0.5t$, and increases with t' thereafter, which indicates that care must be taken when normalizing energies by W.

4.3.3 Pairing Temperature

Unlike conventional superconductors, the high-T_c cuprates display a pseudogap in the spectrum of spin excitations [117, 118], which is usually associated with the formation of Cooper pairs below some temperature scale $T_p \gtrsim T_c$; these preformed pairs condense into a superconducting state at T_c [119]. One of the signatures of this behavior is a drop in

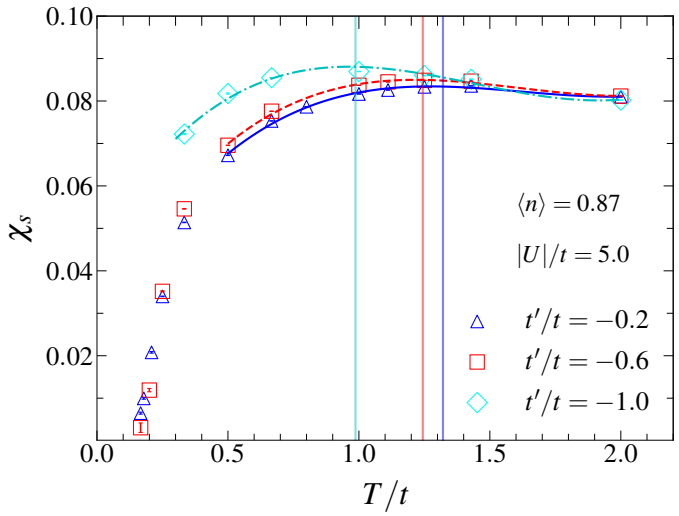

Fig. 4.9: Uniform spin susceptibility as a function of temperature, for different values of t', with fixed $\langle n \rangle = 0.87$ and $|U|/t = 5.0$, for a linear lattice size $L = 16$. The curves through data points represent polynomial interpolations, and the vertical lines locate the maxima. The error bars are smaller than data points.

the uniform susceptibility, χ_s, as the temperature decreases [16, 17, 40, 41, 118, 18, 119, 42, 43, 39]. Therefore, it is also instructive to determine the behavior of T_p as a function of t' in our model.

Figure 4.9 exhibits DQMC data for the temperature dependence of the uniform susceptibility, χ_s [see Eq. (2.15)], for different values of t', and for fixed $|U|/t = 5.0$ and $\langle n \rangle = 0.87$. For each t' we see that χ_s drops steadily below some temperature. In line with the idea that this downturn signals the formation of local pairs within some temperature scale [16, 17, 40, 41, 42, 43], we adopt the position of the maximum in χ_s as the pairing scale, $T_p(t')$. As Fig. 4.9 shows, the maxima can be quite broad, so that their positions are determined by performing a polynomial fit through the data. The error bars are estimated as half of the interval between two temperatures around the maxima. This somewhat flexible definition is consistent with the fact that we are dealing with a crossover, hence T_p must be regarded as signaling a temperature scale, not a sharp transition. We repeat this procedure for other values of t', and collect the estimates for $T_p(t')$ in Fig. 4.10(a), which also includes the corresponding data for T_c from Fig. 4.7(a),

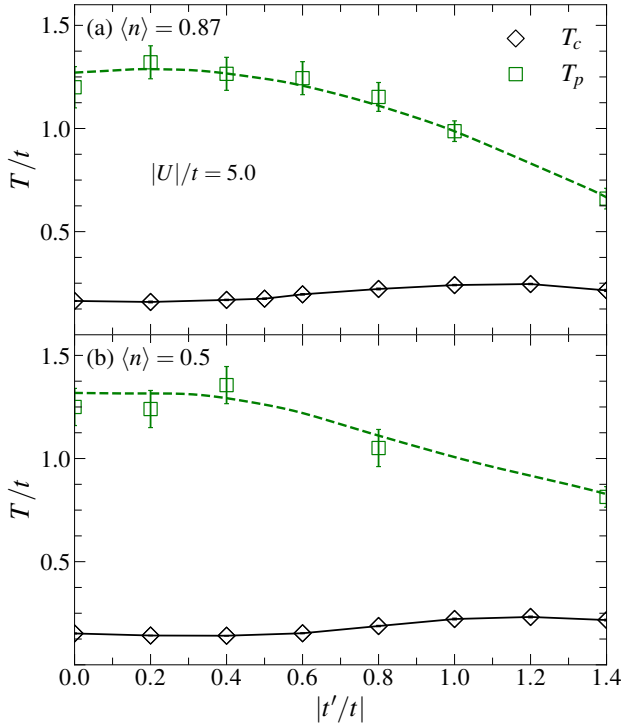

Fig. 4.10: Pairing temperature T_p (squares), and critical temperature T_c (diamonds), as functions of t', for fixed $|U|/t = 5.0$: (a) $\langle n \rangle = 0.87$ and (b) $\langle n \rangle = 0.5$. Lines are guides to the eyes.

for comparison. Figure 4.10(b) shows similar plots for $\langle n \rangle = 0.5$. It is interesting to note that increasing t' causes a decrease in T_p, and an increase in T_c: the NNN hopping channel tends to suppress pair formation, while favoring their condensation. The merging of T_p and T_c for large $|t'/t|$ also suggests a route to approach the BCS limit even at moderate coupling, which, when $t' = 0$, occurs at $|U/t| \ll 1$.

Further insight into the behavior within this Metal-Superconductor transition, crossing a preformed-pair region in the process, may be obtained through the interacting DOS, $D(\omega)$. The latter is obtained from data for the imaginary-time Green's function, $G(\tau)$, extracted from our DQMC simulations, and using the maximum-entropy method [120] to invert the integral equation,

$$G(\tau) = -\int d\omega D(\omega) \frac{e^{-\omega\tau}}{1 + e^{-\beta\omega}}. \tag{4.9}$$

Figure 4.11 shows $D(\omega)$ for $\langle n \rangle = 0.87$, with fixed $U/t = \ -5$, $|t'/t| = 1.0$, and linear

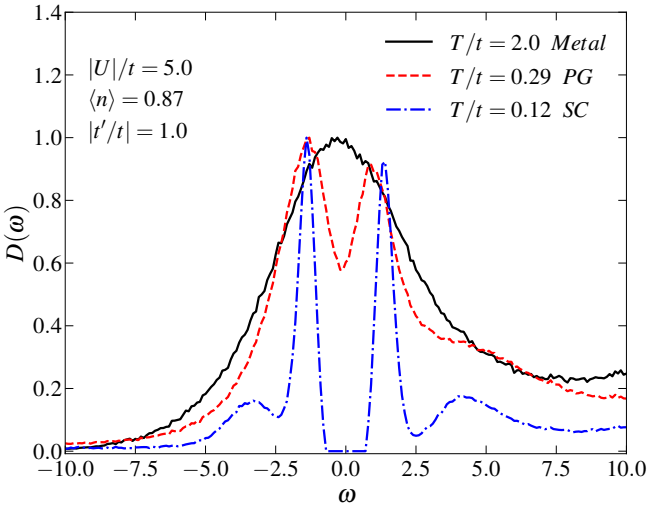

Fig. 4.11: Interacting DOS at different temperatures for fixed $\langle n\rangle = 0.87$, $|U|/t = 5.0$ and $|t'/t| = 1$, for a 16×16 lattice. PG and SC respectively stand for pseudogap and superconducting phases.

size $L = 16$. For $T/t = 2$, the system is in a metallic gapless phase, and $D(0)$ is maximum. As the temperature is decreased, states tend to be suppressed at the Fermi energy, $\omega = 0$, which is associated with the pseudogap region. Further decrease in the temperature leads to a complete depletion of states at $\omega = 0$, when the gap opens and the system becomes superconducting. This scenario is in line with previous findings for the AHM with $t' = 0$ [121].

Let us now investigate what happens to $D(\omega)$ around the Fermi energy, $\varepsilon_{\rm F}$, at temperatures near T_c. To this end, we examine the electronic density within a very narrow range, 2Δ around $\omega = 0$, defined as

$$n_0 = \lim_{\Delta\to 0} \int_{-\Delta}^{\Delta} d\omega D(\omega). \tag{4.10}$$

This quantity must vanish when the system enters the SC phase, due to the opening of the gap at $\varepsilon_{\rm F}$.

In Fig. 4.12(a) we show $D(\omega)$ for several values of t', with $|U|/t$ and $\langle n\rangle$ kept fixed; the temperature T/t is constant, chosen to be slightly above the maximum T_c for all values of t' considered [see the inset in Fig. 4.12 (b)]. We see that $D(0)$ never vanishes. Most

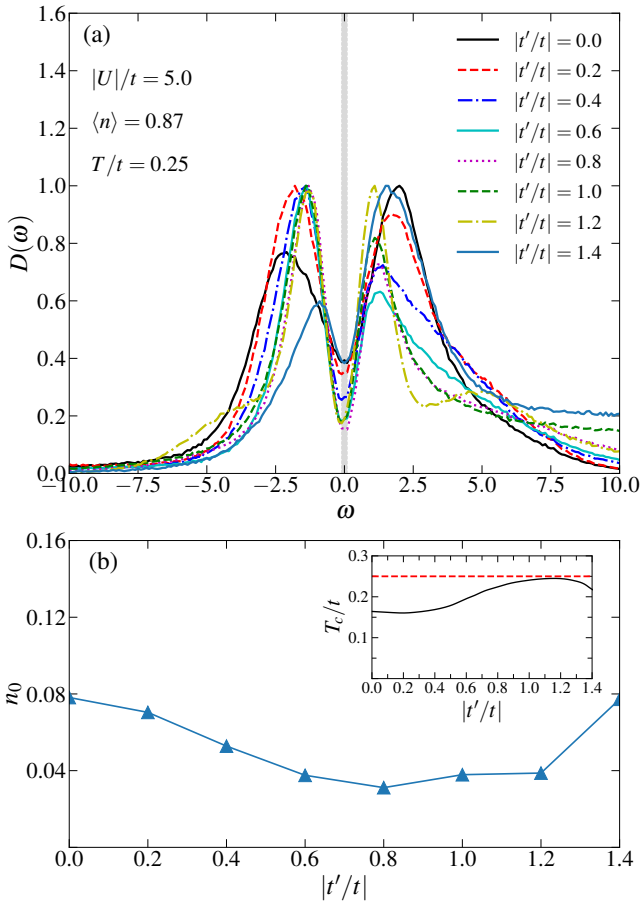

Fig. 4.12: (a) Interacting density of states, $D(\omega)$, for different values of t', and fixed $U/t = -5.0$, $\langle n \rangle = 0.87$. The temperature is kept fixed at $T/t = 0.25$. (b) Fermionic density within an energy range 2Δ around $\omega = 0$, n_0 [see Eq. (4.10)]. We take $2\Delta = 0.2t$, as represented by the shaded area around $\omega = 0$. The inset on panel (b) show the fixed temperature range (red dashed horizontal line), in relation to the critical temperature curve (black full line), for density and attractive interaction fixed.

interestingly, Fig. 4.12 (b) shows that n_0 first decreases steadily with $|t'/t|$, signaling a continuing depletion of the Fermi level. However, this depletion is incomplete, since the temperature is always higher than T_c, so that n_0 never vanishes. Beyond the maximum T_c, n_0 starts increasing, indicating a rise in the occupation of the Fermi level. One may therefore conclude that n_0 at a given temperature measures how far one stands from T_c, as the remaing parameters are varied.

By contrast, Fig. 4.13 shows the corresponding data at a temperature slightly lower than the maximum T_c. In this case, we see that $D(0)$ actually vanishes, with a finite

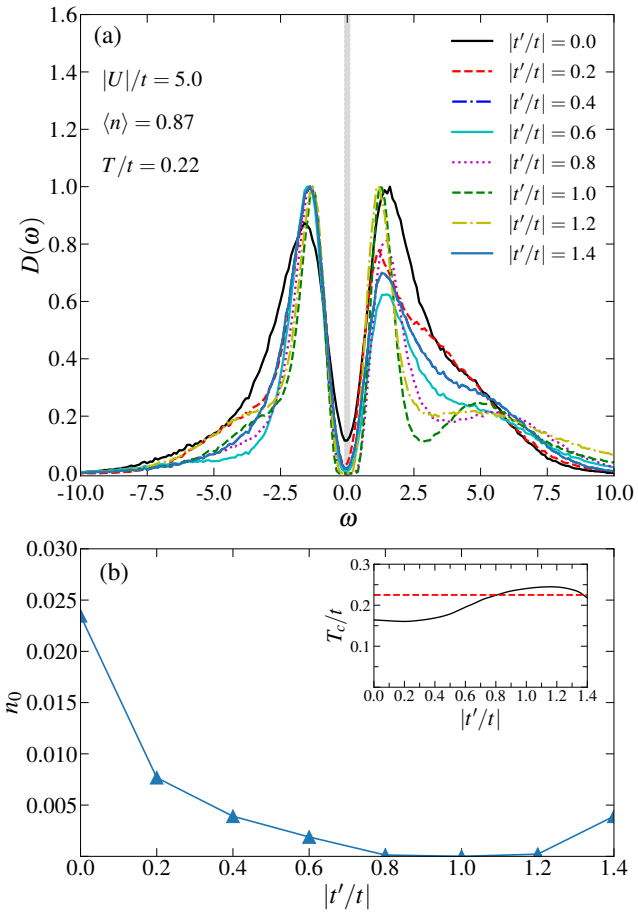

Fig. 4.13: Same as Fig. 4.12, but for $T/t = 0.22$

superconducting gap opening. Accordingly, n_0 now reaches zero, indicating a complete depletion of the Fermi level. This persists until $|t'/t|$ is such that $T \gtrsim T_c$, allowing an increasing occupation of the Fermi level. This reinforces the role of n_0 as a measure of distance from T_c within the pseudogap region.

4.4 Conclusions

We have investigated how the presence of next-nearest-neighbor hoppings affects some pairing properties of the attractive Hubbard model on a square lattice. Through quantum Monte Carlo simulations we have found that an increase in $|t'/t|$ can enhance T_c up to 50% for $|U|/t \lesssim 5$. However, the increase in T_c is not monotonic, since a maximum value is achieved at some ratio $|t'/t| \sim 1$ which depends on both U and the density $\langle n \rangle$.

Interestingly, the relative increase, $T_c(t')/T_c(0)$, reaches a maximum at $|t'/t| \approx 1.2$, with otherwise the same parameters leading to the maximum $T_c(0)$, namely $U = -5t$ and $\langle n \rangle = 0.87$ [39].

We have also examined the influence of t' on the pairing temperature, T_p, which defines the region of pre-formed pairs (often associated with a pseudo-gap phase) above the superconducting phase. It turned out that T_p behaves oppositely to T_c: it decreases with increasing $|t'/t|$, thus decreasing the temperature interval in which pre-formed local pairs exist without coherence. One may conjecture that for sufficiently large $|t'/t|$ the two temperatures merge, thus restoring the BCS regime even in the presence of a sizeable on-site coupling. We attribute this to the fact that while next-nearest neighbor hopping opens new paths for pairs to move, it also hinders pair formation since unpaired fermions also have more paths to follow.

We have also provided numerical evidence that the pseudogap indeed turns into a superconducting gap, by examining the evolution of the interacting density of states, $D(\omega)$. At two fixed temperatures, one slightly above and the other slightly below the maximum T_c, we clearly identify the dip in $D(0)$ vanishing within a finite energy interval when $T < T_c$. In this context, we have introduced n_0, the density of fermions within a small interval, Δ, around the Fermi energy. It turned out that n_0 at a fixed temperature provides a measure of the distance from T_c as the remaining parameters are varied.

The contents of this Chapter has already appeared as Ref. [47].

Chapter 5

The impact of Rashba spin-orbit coupling in charge-ordered systems

5.1 Introduction

So far in this thesis, we have treated superconductivity from the point of view of an effective attractive interaction between electrons. However, this attractive interaction can often occur mediated by lattice vibrations, with the electron-phonon coupling (EPC) favoring the formation of bound electron pairs with opposite spin and momentum, the Cooper pairs, which condense into a superconducting ground state.

In the scenario of phonons mediating interactions between fermions, the Holstein model provides an important framework. This model describe local phonons at each lattice site, with finite frequency ω_0, coupled with itinerant electrons. The EPC can eventually lead to an ordered and coherent state, such as a superconducting state, for a given electronic density or strength of EPC. For instance, on a square lattice with a half filled band, the natural ground state for the Holstein model consists of charge modulation, named Charge-Density-Wave (CDW) [122]. The occurrence of CDW ordering in real materials is due to an EPC, which creates instabilities in the metallic system, leading to a ground state with spatially-modulated charge order [48, 49], a behavior correctly captured by the Holstein model. In addition, such a state is characterized by a gapped single-particle charge spectrum and a gapless collective mode formed by phonon excitations.

Two-dimensional materials such as TMDs compounds have shown CDW ordering and superconductivity, followed by a strong spin-orbit coupling (SOC), due to the atomic number of transition metals [50, 51]. However, the interplay between SOC and EPC remains an open issue in condensed matter physics. Even for the single-excitation case, the leading effects of the competition between the energy gained from coupling with phonons (and its quasiparticle formation) and the electronic dispersion from the SOC are subtle, with the effective polaron mass depending on both EPC and SOC [123, 124, 125, 126]. This delicate balance could have direct implications in the development of novel devices, particularly in the field of spintronics [127]. The degree of complexity is quite increased in the many-electron case, due to the inclusion of electronic correlations. As strong electron-electron interactions introduce many-body effects which may lead to long-range ordered phases, the SOC changes the Hamiltonian symmetries and, consequently, the electron dynamics. This fundamental change could lead to unpredictable physical responses or new phases of matter [128]. Some iridates or pyrochlore materials are prototypes or such interplay, as they are Mott insulators and also exhibit strong SOC effects. Indeed, these compounds show a myriad of phases, from Weyl semimetals and topological insulators, to spin liquid phases [129, 130]. However, while the interplay between SOC and direct (Coulomb) electron-electron has been vastly scrutinized in the literature [131, 132, 133, 134, 135, 136, 137], the leading effects of SOC on indirect interactions, such as the EPC, and vice versa, are much less clear.

From the TMDs point of view, this interplay can be explored in some materials, such as 2H-$TaSe_2$ and 2H-TaS_2, which exhibit significant EPC and SOC effects [138, 139, 140]. In the former, both in bulk and single-layer forms, the CDW phase in the ground state appears to be barely affected by SOC, with the wavevector of this phase remaining almost unchanged, whether SOC is present or not [141]. By contrast, in 2H-TaS_2, SOC has a pronounced impact on the EPC strength, suppressing EPC matrix elements. This suppression of EPC by SOC is essential for accurately explaining the superconducting critical

temperatures observed in this material [142]. Another interesting example is the Pb crystal, which is a conventional (strong coupling) superconductor. For this material, the EPC strength, calculated from Eliashberg functions, is drastically affected by the inclusion of SOC, which is essential to replicate the experimentally observed superconducting (SC) properties [143]. Finally, the interplay between charge order and SOC remains a subject of ongoing debate even for 1D systems, such as in atomic wire arrays on semiconductor surfaces [144], or in the quasi-1D material $(TaSe_4)_2I$. The latter, in particular, is considered as a Weyl semimetal [145], exhibiting Rashba-like band splittings, but also undergoes a CDW phase transition at $T_{\mathrm{CDW}} = 263$ K [146].

As already mentioned, from a theoretical perspective, the Holstein model captures the essential features of systems in which EPC plays a central role [147] and it has been extensively studied in the literature, exhibiting a competition between CDW and SC phases that depends on finely tuned external parameters or the lattice geometry [148, 149, 150, 151, 152, 153, 154, 155, 156, 157, 158, 159, 160]. However, the many-body problem of interacting electron-phonon coupled electrons in the presence of SOC, particularly within the context of the Holstein Hamiltonian, remains a question much less explored. Indeed, Ref. [161] employs an unbiased Quantum Monte Carlo (QMC) approach to explore the emergence of an induced spin-orbit coupling (SOC) when the EPC is spin-dependent, for a square lattice at half-filled regime. In addition, the antiadiabatic limit has also been analyzed in Refs. [162, 163, 164] using QMC methods, as further discussed below.

Motivated by these experimental and theoretical results, we further investigate how a Rashba Spin-Orbit Coupling (RSOC) affects a system with strong EPC, analyzing it both for the adiabatic and antiadiabatic limits. To this end, we employ different methods: first, a Mean-Field-Theory (MFT) and a Cluster-Perturbation-Theory (CPT) are used to extract the information about the spectral quantities; then an unbiased finite-temperature QMC method is employed to examine charge and pairing correlations for the two-dimensional Rashba-Holstein model on a half-filled square lattice. As our main

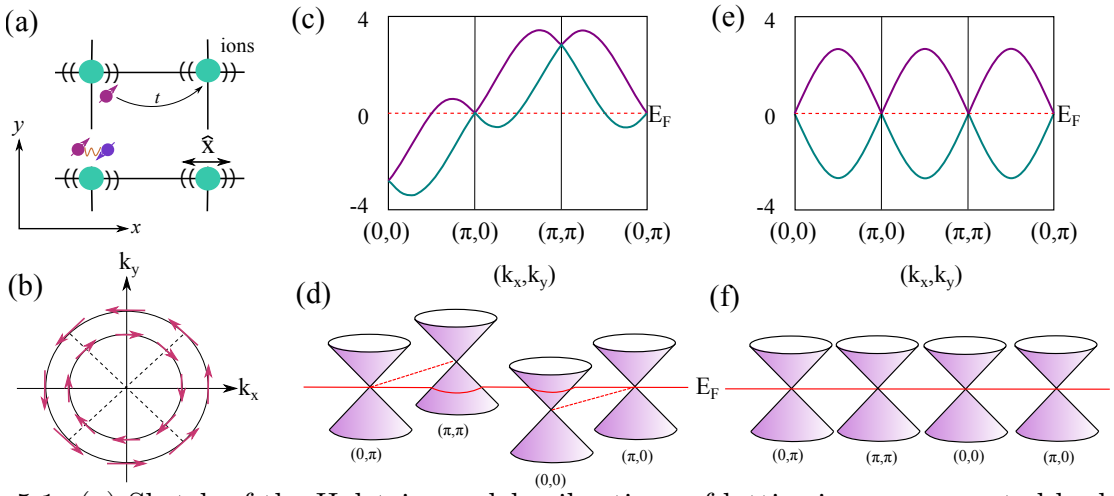

Fig. 5.1: (a) Sketch of the Holstein model: vibrations of lattice ions, represented by local dispersionless phonons, mediate an indirect electron-electron interaction. (b) Illustration of spin splitting due to Rashba spin-orbit coupling in a 2D electron gas, producing spin textures with opposite chiralities. (c) The electronic dispersion relation along the high-symmetry points in a square lattice with finite Rashba spin-orbit coupling. (d) Pictorial representation of four Weyl cones, with two located at the Fermi level (indicated by the red line). (e) Same as in panel (c), but in the pure Rashba hopping limit where $t/\alpha = 0$. (f) Same as in panel (d), but in the pure Rashba hopping limit where $t/\alpha = 0$.

results, we provide finite temperature and ground state phase diagrams. This Chapter is organized as follows: in Sec. 5.2 we present the model. In Secs. 5.4 and 5.5, the MFT and CPT results are present and discuss, while in Sec. 5.6 the DQMC results are presented. Finally, the main conclusions and further remarks are presented in Section 5.8.

5.2 The Rashba-Holstein Hamiltonian

We consider electrons hopping in a single orbital square lattice. Here, we assume the system has a broken $(z \to -z)-$symmetry, as occurs in lead chalcogenides monolayers [165, 166] and in confined electron gases [167, 168, 169, 170], which allows the occurrence of RSOC. In addition, we use the Holstein model to describe the EPC, which captures the local interaction of electrons with single-Einstein phonon degrees of freedom [147].

For the Rashba-Holstein model (RHM), the Hamiltonian reads

$$\begin{aligned}\mathcal{H} = &- t \sum_{\langle \mathbf{i},\mathbf{j}\rangle,\sigma} (c^{\dagger}_{\mathbf{i},\sigma} c_{\mathbf{j},\sigma} + h.c.) - \mu \sum_{\mathbf{i},\sigma} n_{\mathbf{i},\sigma} + \sum_{\mathbf{i}} \left(\frac{\hat{P}^2_{\mathbf{i}}}{2M} + \frac{M\omega_0^2}{2} \hat{X}^2_{\mathbf{i}} \right) \\ &- g \sum_{\mathbf{i},\sigma} n_{\mathbf{i},\sigma} (a_{\mathbf{i}} + a^{\dagger}_{\mathbf{i}}) - t_R \sum_{\langle \mathbf{i},\mathbf{j}\rangle} c^{\dagger}_{\mathbf{i}} \left(\overleftrightarrow{\alpha}_{\mathbf{i},\mathbf{j}} \times \overleftrightarrow{\sigma} \right)_z c_{\mathbf{j}} \ , \end{aligned} \tag{5.1}$$

where the sums run over a square lattice, with $\langle \mathbf{i}, \mathbf{j} \rangle$ denoting nearest neighbors, $\hat{X}_{\mathbf{i}} = \sqrt{\frac{\hbar}{2M\omega_0}}(a_{\mathbf{i}} + a^{\dagger}_{\mathbf{i}})$ and $\hat{P}_{\mathbf{i}} = i\sqrt{\frac{\hbar M\omega_0}{2}}(a^{\dagger}_{\mathbf{i}} - a_{\mathbf{i}})$ being the position and momentum operators, respectively, of a harmonic oscillator in a given site $\mathbf{i}$. Here we use the usual second quantization formalism, with $c_{\mathbf{i},\sigma}$ ($c^{\dagger}_{\mathbf{i},\sigma}$) being a fermionic operator that annihilates (creates) an electron with spin $\sigma = \uparrow, \downarrow$ on a given site $\mathbf{i}$; $n_{\mathbf{i},\sigma} = c^{\dagger}_{\mathbf{i},\sigma} c_{\mathbf{i},\sigma}$ is the fermion number operator. Similarly, $a_{\mathbf{i}}$ ($a^{\dagger}_{\mathbf{i}}$) is a bosonic operator that annihilates (creates) a phonon with energy $\hbar\omega_0$ on a given site $\mathbf{i}$. In the last term of Eq. (5.1), $\overleftrightarrow{\alpha}_{\mathbf{i},\mathbf{j}} \equiv \left(\alpha^x_{\mathbf{i},\mathbf{j}}, \alpha^y_{\mathbf{i},\mathbf{j}}, 0\right)$ is the displacement tensor $\alpha^{\nu}_{\mathbf{i},\mathbf{j}} \equiv i(\delta_{\mathbf{i},\mathbf{j}+\alpha_\nu} - \delta_{\mathbf{i},\mathbf{j}-\alpha_\nu})$, with α_ν being unitary translation in the ν direction, and $\overleftrightarrow{\sigma} \equiv (\sigma_x, \sigma_y, \sigma_z)$ are Pauli matrices related to electronic spin. The first two terms on the right-hand side of Eq. (5.1) correspond to the hopping of the electrons and their chemical potential, respectively. The third term describes the local harmonic oscillators, while the fourth represents the EPC, with strength g. Finally, the last term is the RSOC, with strength t_R. We set the energy scale in units of the hopping integral t.

Before proceeding, it is worthy discussing the limit cases. For instance, the occurrence of long-range order in the pure Holstein model ($t_R = 0$) has been under intense investigation over the past years, at different lattices and fillings. In particular, in the half-filled square lattice, there are strong evidences that support the emergence of CDW for any EPC $g > 0$, at any frequency ω_0 due to instabilities from van Hove singularity (vHs) and the Fermi surface nesting (FSN) [171, 172, 122], different from the 1D case, which exhibits a quantum phase transition [173, 174]. In the antiadiabatic limit, the phonon degree of freedom can be integrated out [175], and the Holstein model is mapped onto the attractive Hubbard model, with effective dynamic electron-electron interaction being $U_{\text{eff}}(\omega) = -\frac{g^2/\omega_0^2}{1-(\omega/\omega_0)^2}$. We define $g^2/\omega_0^2 \equiv \lambda$, which is the energy scale for the polaron

formation, and sets the effective attractive interaction strength in this limit. Notice that the mapping into the attractive Hubbard model leads to a coexistence between CDW and SC for any $|U| > 0$, enforced the $SU(2)$ symmetry.

The most relevant effect of the inclusion of a RSOC is the spin-dependent momentum shift, which splits the spin textures, with well-defined chiralities, as illustrated in Fig. 5.1 (b). It results in a (chiral) splitting of the band structure, shifting the van Hove singularity away from the half-filling, as depicted in Fig. 5.1 (c). As discussed below, such a shift preserves the Fermi surface nesting, creating particle-hole instabilities [135, 176]. Figure 5.1 (c) also provides another interesting issue: the occurrence of four Weyl cones; two at the Fermi level [$(\pi, 0)$ and $(0, \pi)$], and two others above and below the Fermi level [at (π, π) and $(0, 0)$, respectively], as illustrated in Fig. 5.1 (d). The position of the Weyl cones may change depending on the ratio t_R/t, with all cones being at the Fermi level in the limit case of $t/t_R = 0$ (pure Rashba), where a Weyl semimetal (WSM) emerges; see, e.g., Figs. 5.1 (e) and (f).

As mentioned in the Introduction, there are only a few recent unbiased studies available on two-dimensional strongly interacting systems in the presence of SOC. Reference [162] showed that the critical temperatures of the attractive Hubbard model is drastically enhanced by the inclusion of a RSOC, while Refs. [163, 164] investigate how the symmetry of Cooper pair is affected by the RSOC. Both references analyzed the antiadiabatic limit (i.e. for the attractive Hubbard model), and away from the WSM case. In what follows, we investigate this problem in the ground state, by performing analyses through both MFT and CPT approaches.

5.3 Symmetries

Interesting insights can be extracted from this analysis of Hamiltonian (5.1). For instance, at vanishing chemical potential, $\mu = 0$, the Hamiltonian is invariant under

combined particle-hole symmetry

$$P^{-1}t_R c^\dagger_{\mathbf{i},\sigma} P = \overline{t_R} e^{i\mathbf{i}\cdot\mathbf{Q}} c_{\mathbf{i},\sigma} \tag{5.2}$$

and canonical transformation

$$\hat{X}_\mathbf{i} \to -\hat{X}_\mathbf{i},\ \hat{P}_\mathbf{i} \to -\hat{P}_\mathbf{i}. \tag{5.3}$$

Here $\mathbf{Q} = (\pi, \pi)/a$ corresponds to the antiferromagnetic wave vector. As a consequence, $\mu = 0$ corresponds to half-band filling, $\langle n_\mathbf{i} \rangle = 1$. In the absence of interactions, the energy bands read:

$$E_\pm(\mathbf{k}) = \epsilon(\mathbf{k}) \pm |\mathbf{V}(\mathbf{k})| \tag{5.4}$$

with $\epsilon(\mathbf{k}) = -2t\left(\cos(\mathbf{k}\cdot\mathbf{a}_x) + \cos(\mathbf{k}\cdot\mathbf{a}_y)\right)$, and $\mathbf{V}(\mathbf{k}) = 2t_R\left(-\sin(\mathbf{k}\cdot\mathbf{a}_y), \sin(\mathbf{k}\cdot\mathbf{a}_x), 0\right)$. For the antiferromagnetic wave $\mathbf{Q}$ and at half-band filling, $\mu = 0$, the nesting condition is satisfied:

$$\left(E_\pm(\mathbf{k}) - \mu\right) = -\left(E_\mp(\mathbf{k}+\mathbf{Q}) - \mu\right). \tag{5.5}$$

Thereby, in addition to the Cooper instability in e.g. the singlet s-wave channel we observe an antiferromagnetic instability in the particle-hole channel. Owing to the attractive retarded nature of the interaction one will expect charge density wave order to dominate [177].

The $t = 0$ point is special in the sense that the dispersion relation in the vicinity of the chemical potential becomes that of Dirac fermions.

$$E(\mathbf{k}) = \pm\sqrt{\sin^2(\mathbf{k}\cdot\mathbf{a}_x) + \sin^2(\mathbf{k}\cdot\mathbf{a}_y)} \tag{5.6}$$

Expanding around the four time reversal momenta $\mathbf{K} = (0,0), (\pi,\pi), (0,\pi)$, and $(\pi, 0)$ yields the following Dirac Hamiltonian

$$\begin{aligned}\mathcal{H}_{0,t_R} &= v_F \sum_\mathbf{p} c^\dagger_{\mathbf{p},\tau,\mu,\sigma}\left(p_x \delta_{\mu,\mu'}\tau^z_{\tau,\tau'}\sigma^y_{\sigma,\sigma'} - p_y \mu^z_{\mu,\mu'}\tau^z_{\tau,\tau'}\sigma^x_{\sigma,\sigma'}\right) c_{\mathbf{p},\tau',\mu',\sigma'} \\ &\equiv v_F \sum_\mathbf{p} c^\dagger_\mathbf{p}\left(p_x \tau^z\sigma^y - p_y\mu^z\tau^z\sigma^x\right) c_\mathbf{p}\ ,\end{aligned} \tag{5.7}$$

where the Pauli matrices τ^{t_R}, μ^{t_R} and σ^{t_R} act on the τ, μ and σ indices. While σ denotes the spin index, the four eigenstates of $\tau^z\mu^z$ encode the four Dirac points. Specifically $\mathbf{K} = (0,0) \leftrightarrow \tau = 1, \mu = 1$, $\mathbf{K} = (0,\pi) \leftrightarrow \tau = 1, \mu = -1$, $\mathbf{K} = (\pi,\pi) \leftrightarrow \tau = -1, \mu = 1$ and $\mathbf{K} = (\pi,0) \leftrightarrow \tau = -1, \mu = -1$. In the last line we have suppressed the indices to lighten the notation. $\mathbf{p}$ measures momentum from the Dirac points and the Fermi velocity is given by $2t_R a$ with a the lattice constant. While on the lattice, spin-orbit symmetry is discrete, it becomes continuous in the continuum limit with generators $(\tau^x\sigma^z, \tau^y\sigma^z, \tau^z)$ of SU(2).

In the absence of hopping matrix element the Dirac cones are pinned to the chemical potential. In the continuum approximation, the hopping term acts as Dirac cone dependent chemical potential. In particular:

$$\mathcal{H}_{0,t} = -4t \sum_{\mathbf{p}} c^\dagger_{\mathbf{p}} \tau^z \left(\frac{\mu^z + 1}{2} \right) c_{\mathbf{p}}. \tag{5.8}$$

To account for superconducting as well as charge density wave mass terms, we adopt a Bogoliubov basis:

$$\eta^\dagger_{\mathbf{p},\mu,\tau,\sigma,\nu} = \begin{cases} c^\dagger{}_{\mathbf{p},\mu,\tau,\sigma} & \nu = \quad 1 \\ c_{-\mathbf{p},\mu,\tau,\sigma} & \nu = -1 \end{cases} \tag{5.9}$$

In this Bogoliubov basis, the Rashba Hamiltonian reads:

$$\mathcal{H}_{0,t_R} = v_F \sum_{\mathbf{p}} \eta^\dagger_{\mathbf{p}} \left(p_x \tau^z \sigma^y \nu^z - p_y \tau^z \mu^z \sigma^x \right) \eta_{\mathbf{p}}. \tag{5.10}$$

As apparent, the s-wave superconducting order parameter Δ and the charge density order Φ from a triplet of anti-commuting mass terms:

$$\mathbf{M} = (\mathrm{Im}\Delta, \mathrm{Re}\Delta, \Phi) = \left(\nu^x\sigma^y, \nu^y\sigma^y, \nu^z\tau^x \right). \tag{5.11}$$

The three matrices $\Gamma_{i,j} = \frac{i}{2}\left[M_i, M_j\right]$ commute with the Hamiltonian and generate SO(3) rotations between CDW and superconducting orders. Hence provided that the interaction possesses the same symmetry, we expect degenerate superconducting and CDW fluctuations. We will see that this is indeed the case in the anti-adiabatic limit, where the Holstein interaction reduces to an attractive Hubbard-U term.

The Hubbard interaction term satisfies SO(4) symmetry corresponding to SU(2)-spin and SU(2)-η transformations that rotate superconducting states onto CDW orders [178]. The spin symmetry is clearly broken by the Rashba spin-orbit coupling but at $t = 0$ SU(2)-η symmetry is present both in the interaction term as well as is the Dirac Hamiltonian. Hence the appropriate Hamiltonian for this state reads:

$$\mathcal{H} = \mathcal{H}_{0,t_R} - U \int_V d^2\mathbf{x} \sum_{i=1}^{3} \left(c_{\mathbf{x}}^{\dagger} M_i c_{\mathbf{x}} \right)^2 \tag{5.12}$$

This Hamiltonain has SO(3) symmetry which renders degenerate SSC and CDW states.

At finite phonon frequencies, the instantaneous Hubbard term gives way to a retarded interaction. This breaks the SO(3) symmetry and at half-filling we expect the charge density wave state to be favored [177].

5.4 Mean-field theory

We start by discussing the mean-field approach to the Rashba-Holstein Hamiltonian. In this section, we parametrize the hopping terms as $t = \tilde{t}\cos\theta$ and $t_R = \sqrt{2}\tilde{t}\sin\theta$. Within this, the limiting cases of no RSOC ($t_R/t = 0$) and pure RSOC ($t_R/t \to \infty$) correspond to $\theta = 0$ and $\pi/2$, respectively, with $\tilde{t}$ setting the energy scale. In what follows, we define $\omega_0/\tilde{t} = 1$ while varying t, t_R, and g.

Before proceeding, another change in the notation is also recommended: we rewrite the phonon creation and annihilation operators in Eq. (5.1) in terms of position and momentum ones. For instance, by considering the pure Holstein model ($t_R = 0$), its Hamiltonian is

$$\begin{aligned}\mathcal{H}_{\mathrm{H}} = &- t \sum_{\langle \mathbf{i},\mathbf{j}\rangle,\sigma} (c_{\mathbf{i},\sigma}^{\dagger} c_{\mathbf{j},\sigma} + h.c.) - \mu \sum_{\mathbf{i},\sigma} n_{\mathbf{i},\sigma} - g\sqrt{\frac{2M\omega_0}{\hbar}} \sum_{\mathbf{i},\sigma} n_{\mathbf{i},\sigma} \hat{X}_{\mathbf{i}} \\ &+ \sum_{\mathbf{i}} \left(\frac{\hat{P}_{\mathbf{i}}^2}{2M} + \frac{M\omega_0^2}{2} \hat{X}_{\mathbf{i}}^2 \right) ,\end{aligned} \tag{5.13}$$

where, here, we define the mass of the harmonic oscillators (M) and the lattice constant as unities.

Within a static mean-field approach, we assume that the kinetic energy of lattice vibrations is negligible if compared with potential energy ($\hat{P}_{\mathbf{i}}^2/2M \ll M\omega_0^2\hat{X}_{\mathbf{i}}^2/2$), i.e., we deal with a permanent distortion that breaks the translation symmetry of the lattice. This assumption corresponds to the adiabatic regime [179, 180], i.e. $\omega_0 \to 0$ while keeping $M\omega_0^2 \equiv k$ finite. In this regime, the Hamiltonian is a quadratic form for electron creation/annihilation operators, therefore its ground state is exact by a mean-field approach, assuming that our *ansatz* is correct.

We then approximate the position operator by its expectation value, assuming the *ansatz* $\hat{X}_{\mathbf{i}} \to \langle X_{\mathbf{i}} \rangle = X_0 + \cos(\mathbf{Q}\cdot\mathbf{i})X_1$, with $\mathbf{Q} = (\pi,\pi)$. Notice that other ansatz involving arbitrary wavevectors $\mathbf{Q} = (q_x, q_y)$ can be explored, even in incommensurate cases [181]. However, owing to the four-fold rotational symmetry inherent to the square lattice, along with the nesting properties and the commensurate filling, it is expected that the (π,π) configuration is the one that most significantly reduces the internal energy. Therefore, the MFT Holstein Hamiltonian becomes

$$\begin{aligned}\mathcal{H}_{\mathrm{H}} = &- t\sum_{\langle \mathbf{i},\mathbf{j}\rangle,\sigma}(c_{\mathbf{i},\sigma}^{\dagger}c_{\mathbf{j},\sigma} + \mathrm{H.c.}) - \mu\sum_{\mathbf{i},\sigma} n_{\mathbf{i},\sigma} - g\sqrt{\frac{2M\omega_0}{\hbar}}\sum_{\mathbf{i},\sigma} n_{\mathbf{i},\sigma}\left[X_0 + X_1\cos(\mathbf{Q}\cdot\mathbf{i})\right] \\ &+ \frac{NM\omega_0^2}{2}\left(X_0^2 + X_1^2\right), \end{aligned} \tag{5.14}$$

where N is the number of lattice sites.

The inclusion of the RSOC term changes the electron dispersion, and the eventual mean-field Hamiltonian in reciprocal space reads

$$\begin{aligned}\mathcal{H}_{\mathrm{MF}} = &\sum_{\mathbf{k},\sigma}(\varepsilon_{\mathbf{k}} - \mu')c_{\mathbf{k}\sigma}^{\dagger}c_{\mathbf{k}\sigma} + \sum_{\mathbf{k},\sigma,\sigma'}(\widehat{V}_{\mathbf{k}})_{\sigma\sigma'}c_{\mathbf{k}\sigma}^{\dagger}c_{\mathbf{k}\sigma'} - g\sqrt{\frac{M\omega_0}{2\hbar}}X_1\sum_{\mathbf{k},\sigma}(c_{\mathbf{k}+\mathbf{Q}\sigma}^{\dagger}c_{\mathbf{k}\sigma} + \mathrm{H.c.}) \\ &+ \frac{NM\omega_0^2}{2}\left(X_0^2 + X_1^2\right), \end{aligned} \tag{5.15}$$

with $\varepsilon_{\mathbf{k}} = -2t(\cos k_x + \cos k_y)$, $\widehat{V}_{\mathbf{k}} \equiv 2t_{\mathrm{R}}(\sigma_x \sin k_y - \sigma_y \sin k_x)$, and $\mu' = \mu + g\sqrt{2M\omega_0/\hbar}X_0$. In a basis of Nambu spinors $\Phi_{\mathbf{k}}^{\dagger} = (c_{\mathbf{k}\uparrow}^{\dagger}, c_{\mathbf{k}\downarrow}^{\dagger}, c_{\mathbf{k}+\mathbf{Q}\uparrow}^{\dagger}, c_{\mathbf{k}+\mathbf{Q}\downarrow}^{\dagger})$, we obtain a quadratic form

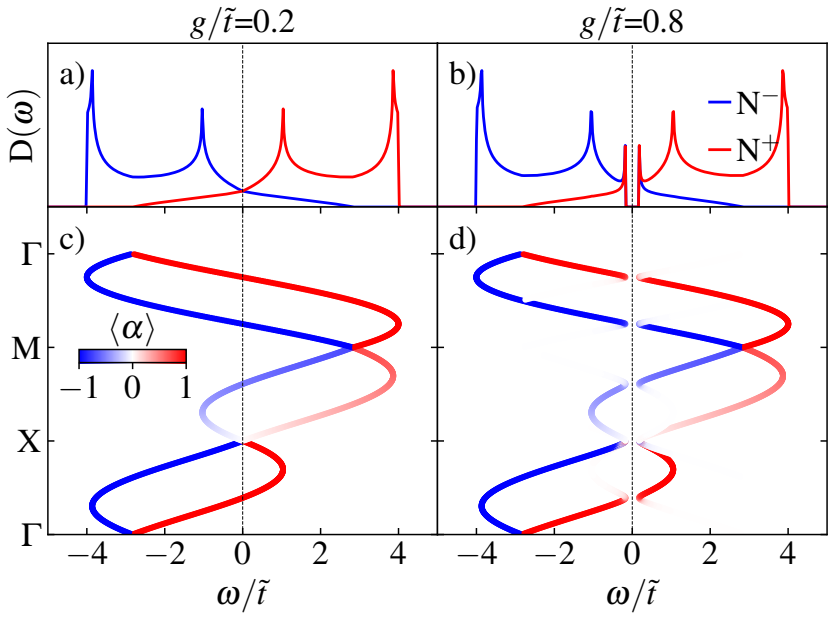

Fig. 5.2: The mean-field result for the density of states of the Rashba-Holstein model for EPC (a) $g/\tilde{t} = 0.2$, and (b) $g/\tilde{t} = 0.8$, and its electronic dispersion in (c) and (d), respectively. The results are for fixed RSOC $t_{\mathrm{R}}/t = \sqrt{2}$, with the color codes indicating the chiral spin-texture polarization of bands.

representation of $\mathcal{H}_{MF}$,

$$\mathcal{H}_{\mathrm{MF}} = \frac{1}{2}\sum_{\mathbf{k}} \Phi_{\mathbf{k}}^{\dagger} \widehat{H}_{\mathbf{k}} \Phi_{\mathbf{k}} + \frac{NM\omega_0^2}{2}\left(X_0^2 + X_1^2\right) \tag{5.16}$$

where

$$\widehat{H}_{\mathbf{k}} = \begin{pmatrix} \varepsilon_{\mathbf{k}} - \mu' & (\widehat{V}_{\mathbf{k}})_{\uparrow\downarrow} & -\Delta X & 0 \\ (\widehat{V}_{\mathbf{k}})_{\downarrow\uparrow} & \varepsilon_{\mathbf{k}} - \mu' & 0 & -\Delta X \\ -\Delta X & 0 & \varepsilon_{\mathbf{k}+\mathbf{Q}} - \mu' & (\widehat{V}_{\mathbf{k}+\mathbf{Q}})_{\uparrow\downarrow} \\ 0 & -\Delta X & (\widehat{V}_{\mathbf{k}+\mathbf{Q}})_{\uparrow\downarrow} & \varepsilon_{\mathbf{k}+\mathbf{Q}} - \mu' \end{pmatrix} \tag{5.17}$$

with $\Delta X = g\sqrt{2M\omega_0/\hbar}X_1$. Notice that we added X_0 to the chemical potential μ', since this field shifts the energy level, while the X_1 field modulates the electronic distribution, therefore being proportional to the amplitude of the CDW order parameter. Indeed, if we define $\langle n_i \rangle = n + \cos(\mathbf{Q}\cdot\mathbf{i})\delta n$, from Eq. (5.14) one obtains $\delta n = \omega_0\sqrt{\frac{M\hbar\omega_0}{2}}\frac{X_1}{g}$, which is our MFT order parameter.

The parameters $X_{0(1)}$ are determined self-consistently by minimizing the Helmholtz free energy, through the diagonalization of Eq. (5.16). We use the minimization solutions

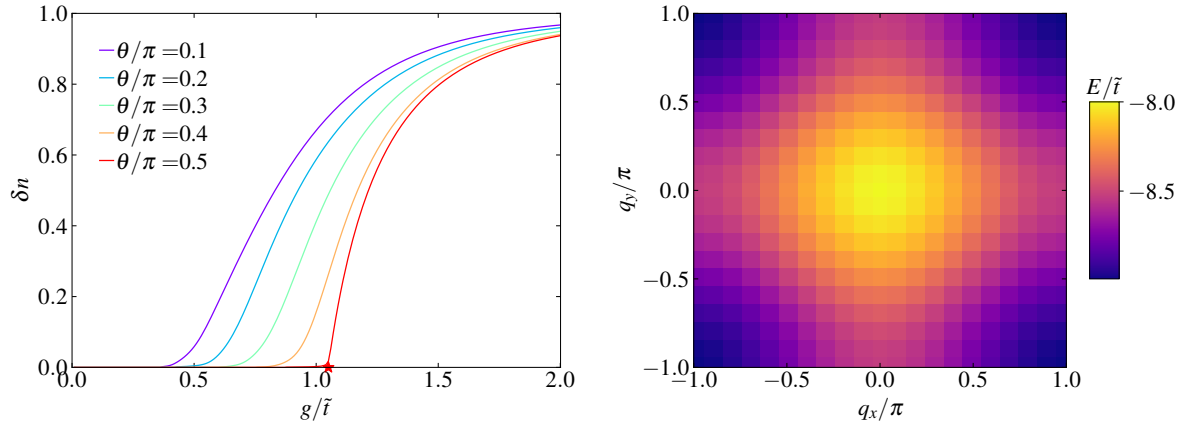

Fig. 5.3: Left panel: The behavior of the ground state mean-field parameter X_1 (proportional to the CDW order parameter) as a function of the EPC g, for different values of RSOC t_R's. Right panel: Contour plot of the MFT internal energy as a function of the CDW wavevectors q_x and q_y, for fixed $g/\tilde{t} = 2$ and $\theta = \pi/2$, at the ground state.

to describe the ground state properties of the system, such as the DOS and the electron dispersion, e.g., as displayed in Fig. 5.2 for small and large values of EPC, while keeping $t_R/t = \sqrt{2}$ [$\tan(\theta) = 1$] fixed. When $g/\tilde{t} = 0.2$, the mean-field solution leads to a negligible CDW order parameter (as discussed later), and the system resembles a Rashba metal. This is presented in Figs. 5.2 (a) and (c), where the RSOC splits the electronic spectra into two branches with well-defined chiralities, $\langle \overleftrightarrow{\sigma} \rangle.(\mathbf{k} \times \hat{z})/|\mathbf{k}| = \pm 1$ for right-handed and left-handed. Such a split shifts the energy levels and, consequently, the van Hove singularities, leading to a reduction in the DOS at the half-filling, as shown in Fig. 5.2 (a). On the other hand, for larger EPC, the mean-field solution leads to a robust charge modulation, creating a charge gap at the half-filling, as displayed in Figs. 5.2 (b) and (d), for $g/\tilde{t} = 0.8$.

To further emphasize the effects of the RSOC on the CDW phase, Fig. 5.3 (upper panel) displays the behavior of δn as a function of $g/\tilde{t}$, for different values of θ, in the ground state. If one fixes a value for $g/\tilde{t}$ and increases θ [i.e., any vertical line in Fig. 5.3 (upper panel)], it is clear that the main effect of the RSOC is to reduce the charge modulation. Notice also that, as displayed in Fig. 5.3 (upper panel), δn exhibits an

asymptotic behavior for any $0 \leq \theta < \frac{\pi}{2}$, which is a consequence of the FSN at the half-filling, despite the absence of the vHs. Therefore, within the MFT, one obtains a CDW ground state, except when $\theta = \pi/2$ (i.e., $t_R/t \to \infty$), where a WSM may emerge. For the latter, as displayed in Fig. 5.3 (upper panel), there is a quantum critical point from a WSM to a staggered CDW phase at $g_c/\tilde{t} \approx 1.05$.

At this point, we have to recall that, for $\theta = \pi/2$, the Dirac cones are nested for both $\mathbf{Q} = (\pi, \pi)$ and $\mathbf{Q} = (0, \pi)$ wavevectors, which could lead to striped phases. Indeed, in the Rashba-Hubbard model, a $(0, \pi)$-striped antiferromagnetic phase emerges around $\theta = \pi/2$ [176]. Therefore, it is worth investigating the stabilization of the CDW order for different wavevectors $\mathbf{Q} = (q_x, q_y)$. The contour plot of Fig. 5.3 (lower panel) displays the internal energy for different wavevectors, for fixed $g/\tilde{t} = 2$ and $\theta = \pi/2$ [1]. It is clear from the figure that the (π, π) mode is the most stable one. The same analysis for other values of θ and $g/\tilde{t}$ also leads to the staggered CDW phase as being more stable than the striped ones, by contrast to the Rashba-Hubbard model.

As depicted in Fig. 5.3 (upper panel), the CDW order parameter exhibits two regimes for any $0 \leq \theta < \pi/2$: a strong and a weak one (exponentially small). To facilitate the following discussion, here we define the former as the CDW phase and the latter as the weak-CDW (wCDW) one, although both denote the same charge-ordered state. In practice, we delineate the crossover between the CDW and wCDW phases using a threshold ($\delta n = 10^{-3}$) for the order parameter. This distinction is crucial because the wCDW region is susceptible to exponentially small perturbations found in real compounds, whether external (e.g., temperature effects) or intrinsic (due to slight next-nearest neighbor hoppings). For instance, in the presence of small temperature fluctuations, the CDW-wCDW crossover would approximately mark the critical region between the CDW and the Rashba

[1] At this point we have to caution the reader that the block-diagonal subspace represented in Eq. (5.17) is exact for $\mathbf{Q} = (\pi, \pi)$ or $(0, \pi)$. However, for any $\mathbf{Q} = (q_x, q_y)$ different from those, one may not easily block-diagonalized it, and Eq. (5.17) becomes equivalent to a quasidegenerate perturbation theory (see, e.g., the discussion in Ref. [181])

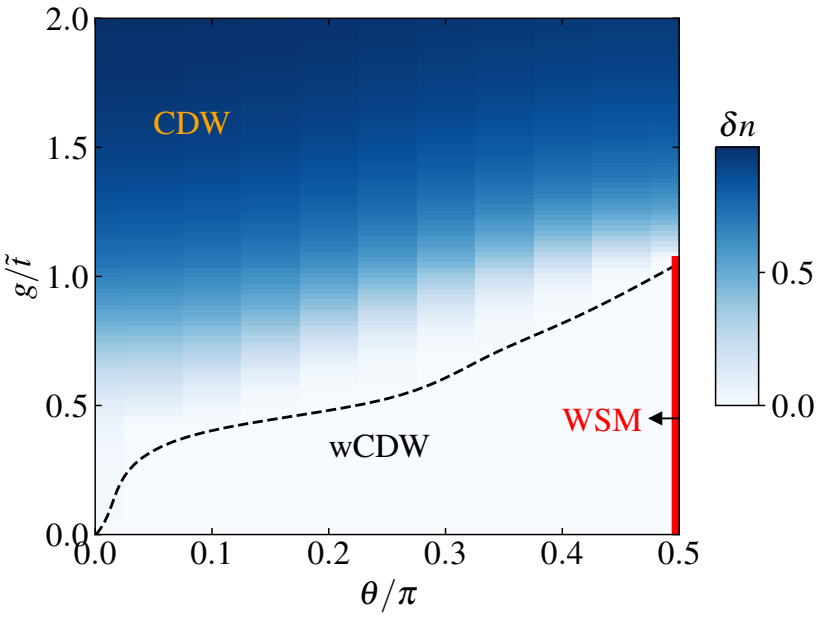

Fig. 5.4: The ground-state MFT phase diagram of the Rashba-Holstein model in the half-filled square lattice. The blue heatmap indicates the amplitude of charge modulation in the CDW phase. The black dashed line corresponds to the CDW-wCDW crossover, while the red vertical line denotes the Weyl semimetal phase in $\theta = \pi/2$.

metal phases. Furthermore, the wCDW phase is also unstable against the enhancement of competing tendencies, such as superconductivity. Since our static mean-field analysis only permits the investigation of CDW phases and fails to capture long-range correlations, the existence of this wCDW phase may be an artifact of the mean-field solution.

Repeating similar analyses as those of Fig. 5.3, we are able to present the mean-field phase diagram of the Rashba-Holstein model at half-filling, as shown in Fig. 5.4. Here, the CDW-wCDW crossover is denoted by the dashed black curve, while the color-map scheme describes the amplitude of the charge modulation, δn. Interestingly, the CDW-wCDW crossover is pushed for larger values of $g/\tilde{t}$ as the t_R/t ratio increases, until it reaches the pure Rashba model ($\theta/\pi = 0.5$), where a true quantum critical phase transition takes place at $g_c/\tilde{t} = 1.05$, from a Weyl semimetal to a CDW state. In Fig. 5.4, the Weyl semimetal phase is depicted as the vertical red solid line at $\theta/\pi = 0.5$. These results are in line with our previous discussion, that the RSOC tends to suppress the CDW phase,

maybe leading to a Rashba metal one.

Despite being obtained by a static mean-field approach, the phase diagram of Fig. 5.4 is expected to provide the correct transition lines when $\omega_0 \to 0$. However, $\omega_0/\tilde{t} = 1$ is clearly away from this limit, which may require less biased methodologies to investigate the Hamiltonian properties, as discussed in the next Section.

5.5 Cluster Perturbation Theory

Now, we use the cluster perturbation theory, which is a convenient technique to extract spectral weights and the electronic DOS of a correlated system. Briefly speaking, the CPT consists of partitioning an infinite lattice into clusters of finite size where the Hamiltonian is exactly solved, while coupling the clusters by perturbation theory approaches. A pedagogical introduction to this method can be found in Ref. [182, 183, 184], and a more detailed discussion in the Appendix C.

This method enable us write a CPT Green's functions, $G_{\mathrm{CPT}}(\mathbf{k},\omega)$, which approximates the behavior of the infinite lattice starting from the Green's function of the finite-sized cluster. By incorporating the leading-order interaction terms, $G_{\mathrm{CPT}}(\mathbf{k},\omega)$ provides a framework to calculate the spectral weight

$$A_0(\mathbf{k},\omega) = -\frac{1}{2\pi}\mathrm{Im}[G_{\mathrm{CPT}}(\mathbf{k},\omega)], \tag{5.18}$$

and the DOS

$$D(\omega) = \frac{1}{N}\sum_{\mathbf{k}} A_0(\mathbf{k},\omega). \tag{5.19}$$

In what follows, we use the DOS to identify the transition from a gapped CDW phase to a Rashba metal, from a gapped CDW phase to an ungapped one. However, it is important to note that our results are constrained by the resolution of the methodology, making it challenging to detect tiny gaps. As previously discussed, a metallic phase is inherently unstable under any external interaction, except when $t/t_R = 0$. Therefore, the term '*Rashba metal*' used hereafter is equivalent to a wCDW.

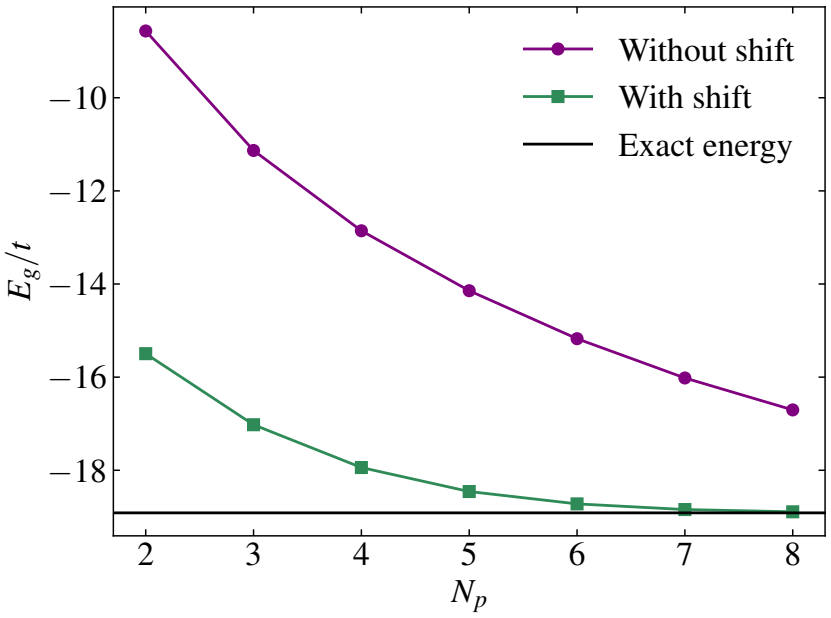

Fig. 5.5: The ground state energy of the Holstein model for $g/t = 1.5$, in a 2×2 plaquette, as a function of the cutoff number of phonons per site N_p. The dark green squares (purple circles) symbols denote the ground state energies for the case with (without) a shift to symmetrize the electron-phonon term.

At this point, it is worth discussing a few technical issues about our CPT implementation. Due to the phonon degrees of freedom, the Hilbert space is infinite, which demands a cutoff in the total number of phonons to perform the exact diagonalization procedure. Among the different ways of establishing this cutoff, we have defined a maximum limit, N_p, for the number of phonons per site. Its value is determined through a systematic analysis of the ground state energy E_g as a function of N_p, as displayed in Fig. 5.5, for fixed $g/t = 1.5$ and $\omega_0/t = 1$, in a 2×2 plaquette. Notice that $E_g(N_p)$ goes asymptotically to the limit $N_p \to \infty$, so the error from the cut-off may be disregarded for a given value of N_p. However, the electron-phonon term described in Eq. (5.1) requires a substantial number of phonons to attain the correct ground state, as evidenced by the behavior of the purple circle symbols in Fig. 5.5. To circumvent this difficulty and keep N_p as small as possible, we perform a shift in the phonon operators $a_{\mathbf{i}} \to \left(a_{\mathbf{i}} + g\langle n\rangle\right)$, with $\langle n\rangle$ being the average electron density. We emphasize that such a shift is equivalent to a change in the

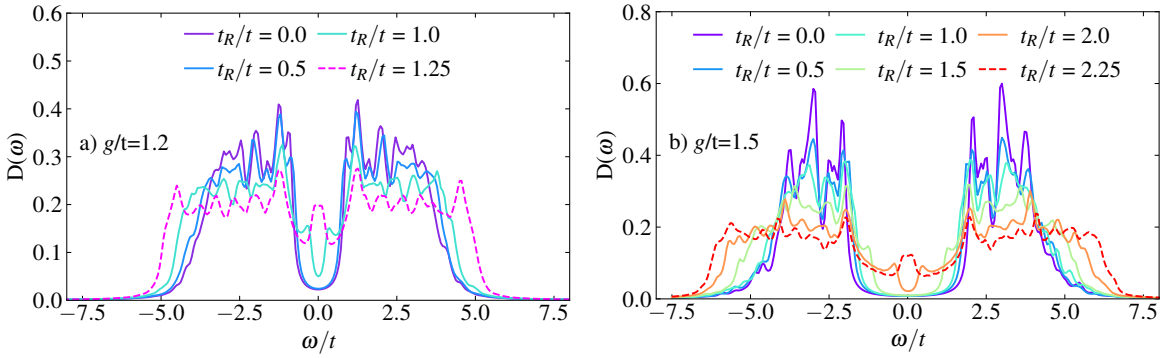

Fig. 5.6: The DOS of the Rashba-Holstein model for EPC (a) $g/t = 1.2$ and (b) $g/t = 1.5$, for different values of RSOC t_R.

origin of the phonon position operators $\hat{X}_{\mathbf{i}}$ to deal just with excitations around its mean value. This drastically reduces the number of required phonons, as shown by the behavior of the dark green square symbols in Fig. 5.5. Despite this improvement, the greater the EPC, the larger the values of N_p, therefore we limit our analyses to intermediate coupling strengths for clusters of 2×2 sites.

In what follows, we use the CPT method to discuss the effects of the RSOC on the spectral properties of our charge-ordered system at the half-filling, for fixed $\omega_0/t = 1$, without the parametrization of the hopping terms. Figure 5.6 (a) displays the behavior of $D(\omega)$ for $g/t = 1.2$ and different values of t_R. When $t_R = 0$, the system has a large charge gap around $\omega = 0$, in line with our expectation of a CDW phase for the Holstein model in the half-filled square lattice. Interestingly, the size of the gap remains nearly unchanged for $t_R/t \lesssim 0.5$, which shows that the CDW phase is robust against spin-orbit perturbations up to this value. However, for larger RSOC, the charge gap drastically decreases, until $D(\omega \approx 0)$ exhibits a peak instead of a gap for $t_R/t \approx 1.25$. This specific change in the behavior of $D(\omega)$ around $\omega \approx 0$ (and $t_R/t \approx 1.25$) is a clear indication of the occurrence of a transition from the CDW phase to a Rashba metal.

A very similar behavior occurs for different values of g, as displayed in Fig. 5.6 (b), for $g/t = 1.5$. The main difference between this case and the previous one is the need for a larger RSOC to destroy the charge gap. In view of this, here we define as *critical points*

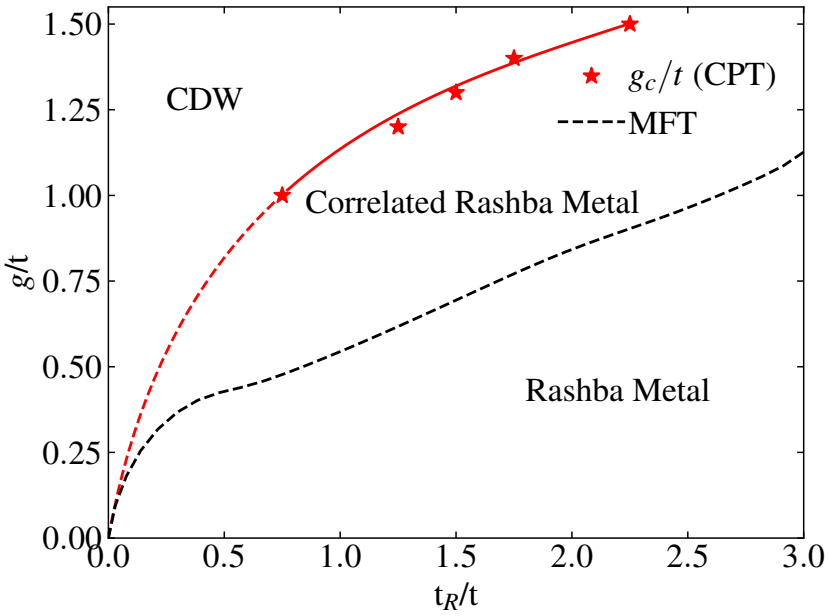

Fig. 5.7: The ground-state CPT phase diagram of the Rashba-Holstein model in the half-filled square lattice. The red (dashed and solid) lines are just guides to the eye, while the black dashed curve is the CDW-wCDW crossover from the MFT solution.

the values of t_R at which $D(\omega)$ exhibits a peak instead of a gap at the half-filling. These CPT critical points are presented as red star symbols in the phase diagram of Fig. 5.7, with the red (dashed and solid) lines being just guides to the eye. The dashed black curve denotes the CDW-wCDW crossover from the MFT solution, which is important to compare both methodologies, as discussed below.

In order to further emphasize the phase transitions, we extract the charge gap directly from Fig. 5.6 by defining the CDW order parameter, $\Delta_{\rm CDW}$, as the energy difference between the two peaks away from $\omega = 0$. The behavior of $\Delta_{\rm CDW}$ as a function of t_R is displayed in Fig. 5.8, for $g/t = 1.2$ (red diamond symbols) and 1.5 (blue triangle symbols), from which one may notice that the gap closing is consistent with a second order phase transition. In particular, the suppression of the CDW phase seems to occur at $t_{R(c)} = 1.1 \pm 0.1$ for $g/t = 1.2$, and at $t_{R(c)} = 2.1 \pm 0.1$ for $g/t = 1.5$.

There are clear differences between the CPT and MFT results, which may be understood through two key remarks. First, and foremost, the CPT method takes into

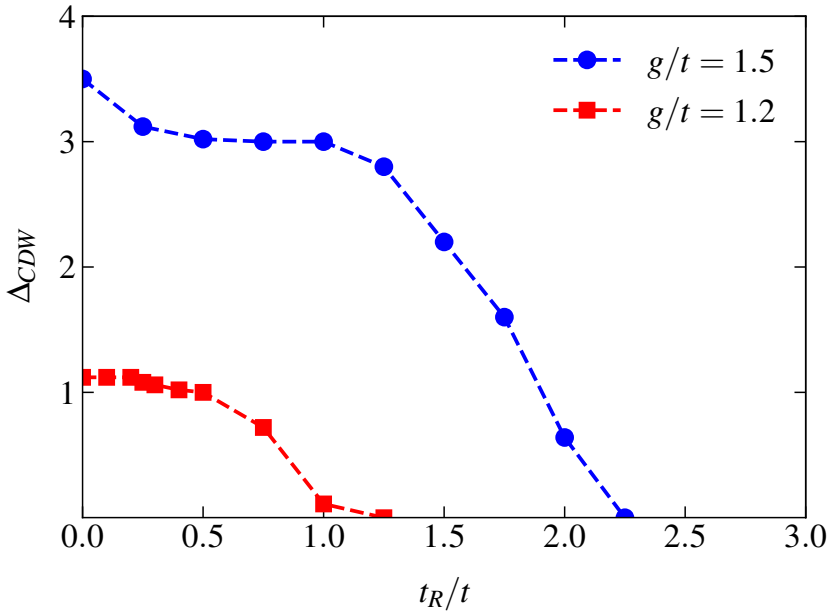

Fig. 5.8: The CDW charge gap, Δ_{CDW} as a function of the RSOC, t_R/t, for fixed $\omega_0/t = 1$.

account the effects of short-range electronic correlations, while the MFT deals with local ones. That is, the MFT (CDW-wCDW crossover) line exhibits the points where there are strong on-site correlations, while the CPT provides insights when these correlations become long-ranged. Therefore, the region enclosed between the MFT and CPT lines in Fig. 5.4 defines a *correlated* Rashba metal, i.e. metallic (from CPT) but with strong on-site correlations (from MFT approach). As a second remark, we recall that the mean-field solution is exact at the ground state when $\omega_0 \to 0$, thus the MFT line in Fig. 5.4 can also be interpreted as as the boundary of the adiabatic limit. That is, if one reduces ω_0, the CPT transition line must be pushed into the MFT ones. Then, it provides the behavior of the critical points when ω_0 changes.

Last, but not least, we recall that the SOC has been investigated in different contexts of strongly correlated systems, in particular for those involving electron-electron interactions. Then, it is imperative to compare these cases with ours, highlighting both their similarities and differences. For instance, for the repulsive Hubbard model in the half-filled square lattice, the inclusion of the RSOC leads to the emergence of novel magnetic

phases, which may include spiral and striped ones; away from the half-filling, ferromagnetism may appear [185, 186, 134, 187, 135, 188, 176]. This occurs due to the spin-flip term in the RSOC, which disfavors the staggered antiferromagnetic ground state of the half-filling, suppressing the charge gap, while keeping gapless spin excitations. Due to the spin dependence in the interaction term in the Hubbard model, the CPT spectral properties for this case exhibit a clear dependence of the chiral bands and DOS as a function of the Hubbard interaction strength U [186]. It is substantially different from our present study, since the interaction term in the Rashba-Holstein model is not spin-dependent, with the spin and charge gaps emerging/disappearing together. Furthermore, noteworthy changes manifest in the attractive Hubbard model when subjected to the RSOC. This model exhibits s-wave superconductivity for any filling [38, 68, 39], whose critical temperatures are significantly increased with the inclusion of the RSOC [162, 163, 189]. This enhancement results from the suppression of charge-charge correlations, in line with our findings for the Rashba-Holstein model. Given that the antiadiabatic regime ($\omega_0 \to \infty$) of the Holstein one can be mapped onto the attractive Hubbard model, we anticipate the emergence of superconductivity in our scenario, coexisting or not with a CDW phase. However, achieving this would require the application of unbiased methodologies, such as quantum Monte Carlo methods, which is discuss in the next section.

5.6 Determinant Quantum Monte Carlo Approach

To simplify the discussion, in this section we will rewrite the Hamiltonian (5.1) in a symmetric form,

$$\mathcal{H} = -t \sum_{\langle \mathbf{i},\mathbf{j}\rangle,\sigma} \left(c^{\dagger}_{\mathbf{i},\sigma} c_{\mathbf{j},\sigma} + \text{H.c.} \right) - \mu \sum_{\mathbf{i},\sigma} n_{\mathbf{i},\sigma} - \alpha \sum_{\mathbf{i},\sigma,\sigma'} \Big[\left(i c^{\dagger}_{\mathbf{i},\sigma} [\hat{\sigma}^{x}]_{\sigma,\sigma'} c_{\mathbf{i}+\hat{\mathbf{y}},\sigma'} - i c^{\dagger}_{\mathbf{i},\sigma} [\hat{\sigma}^{y}]_{\sigma,\sigma'} c_{\mathbf{i}+\hat{\mathbf{x}},\sigma'} \right) + \text{H.c.} \Big] + \sum_{\mathbf{i}} \left(\frac{\hat{P}^{2}_{\mathbf{i}}}{2M} + \frac{M\omega_0^{2}}{2} \hat{X}^{2}_{\mathbf{i}} \right) - g \sum_{\mathbf{i},\sigma} \left(n_{\mathbf{i},\sigma} - 1 \right) \hat{X}_{\mathbf{i}}, \tag{5.20}$$

where sums run over a two-dimensional square lattice under periodic boundary conditions, with $\langle \mathbf{i}, \mathbf{j} \rangle$ denoting nearest neighbors sites. Note that here, we have rewritten the third term of the initial Hamiltonian (5.1), which describes the spin-orbit contribution, of strength α now, with $[\hat{\sigma}^{\gamma}]_{\sigma,\sigma'}$ defining the elements of Pauli matrices ($\gamma = x$, y and z).

To perform a DQMC simulation, the Hamiltonian (5.20) can be written as $\mathcal{H} = \mathcal{H}_k + \mathcal{H}_{ph} + \mathcal{H}_{el-ph}$, with terms on the right-hand side of the equality corresponding to the kinetic energy electrons (which includes the chemical potential and the RSOC contributions), the bare phonons energy, and the electron-phonon coupling, respectively. Therefore, the Trotter-Suzuki decomposition leads to the partition function

$$Z = \mathrm{Tr}\left[\cdots e^{-\Delta\tau\mathcal{H}_k} e^{-\Delta\tau\mathcal{H}_{ph}} e^{-\Delta\tau\mathcal{H}_{el-ph}} \cdots\right],$$

where the trace is performed over both bosonic and fermionic degrees of freedom. Using the HO's positions and the creation and annihilation operators as basis for the states, the bosonic trace leads to the inclusion of a bare phonons action, while the fermionic one leads to a single determinant. Notice that, due to the spin-flip terms of the RSOC, the fermionic weights cannot be rewritten as a product of up and down determinants. That is, the partition function becomes

$$Z = \int \mathrm{d}\{x_{\mathbf{i},l}\} e^{-\Delta\tau S_B} \left[\det\left(I + B_{L_\tau} B_{L_\tau - 1} \cdots\right)\right],$$

with $B_l = e^{[-\Delta\tau H_k]} e^{[-\Delta\tau H_{el-ph}(\{x_{\mathbf{i},l}\})]}$ being the products of the exponential of the matrix representation of the kinetic and electron-phonon terms, respectively, at a given time slice l. Here, $\{x_{i,l}\}$ denotes the set of auxiliary (phonon) fields in real and imaginary-time coordinates, with the integral (i.e., the bosonic trace) $\int d\{x_{\mathbf{i},l}\}$ being performed by Monte Carlo methods. Finally, the exponential $e^{-\Delta\tau S_B}$ is the bare phonon action

$$S_B = \frac{\omega_0^2}{2} \sum_i \sum_{l=1}^{L_\tau} \left[\frac{1}{\omega_0^2 \Delta\tau^2} \left(x_{i,l} - x_{i,l+1}\right)^2 + x_{i,l}^2\right],$$

obtained from free phonon contribution in the partition function, i.e. $e^{-\Delta\tau\mathcal{H}_{ph}}$. Therefore,

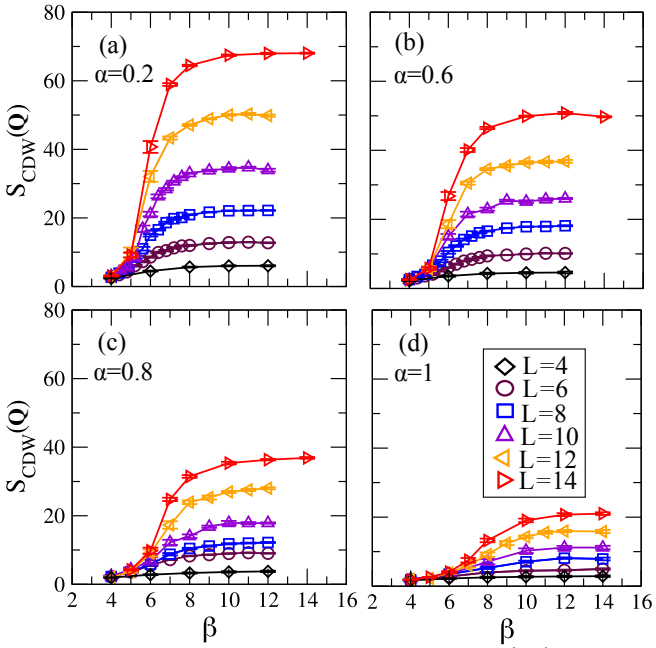

Fig. 5.9: The change-density wave structure factor, $S_{CDW}(\mathbf{Q})$, as a function of the inverse of temperature (β) for different values system sizes and fixed (a) $\alpha = 0.2$, (b) $\alpha = 0.6$, (c) $\alpha = 0.8$ and (d) $\alpha = 1.0$. The phonon frequency is $\omega_0/t = 1$ and the electron-phonon coupling is given by $\lambda/t = 2$. Here, and in all subsequent figures, when not shown, error bars are smaller than symbol size.

$e^{-\Delta\tau S_B}\det\left(I + B_{L_\tau}B_{L_\tau-1}\cdots\right)$ is used as our statistical weight throughout the Monte Carlo sampling. This approach does not suffer from the infamous minus-sign problem.

To examine the effects of the electron-phonon coupling and the possible emergence of long-range order, we investigate charge-charge correlations, $\langle n_{\mathbf{i}} n_{\mathbf{j}}\rangle$, and their Fourier transform, the charge structure factor,

$$S_{\mathrm{CDW}}(\mathbf{q}) = \frac{1}{L^2}\sum_{\mathbf{i},\mathbf{j}} e^{i(\mathbf{i}-\mathbf{j})\cdot\mathbf{q}}\langle n_{\mathbf{i}} n_{\mathbf{j}}\rangle, \tag{5.21}$$

with L being the linear size of the system. The peak of $S_{\mathrm{CDW}}(\mathbf{q})$ defines the leading wavevector $\mathbf{Q}$ in which the system may exhibit charge order. At this point, we should warn that, to compute the correlation functions, one has to include spin-flip terms in the

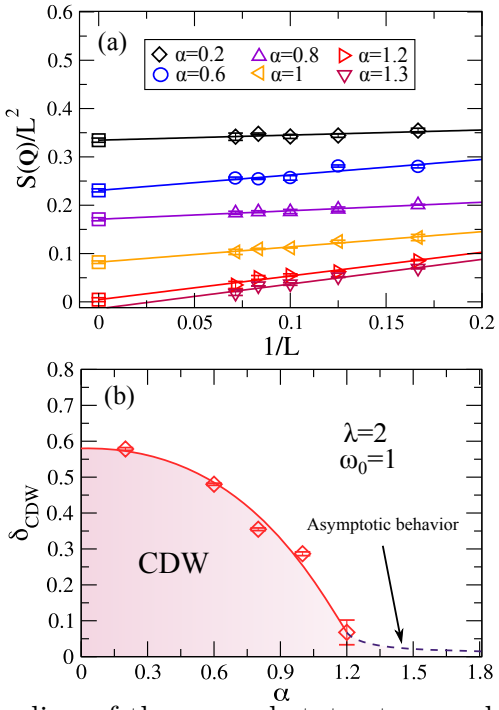

Fig. 5.10: (a) Finite-size scaling of the ground-state staggered CDW structure factor for different RSOC, α, and fixed $\omega_0 = 1$ and $\lambda/t = 2$. (b) The CDW order parameter, δ_{CDW}, as a function of α, for the same parameters of the previous panel. The red curve is just a guide to the eye.

Wick's decomposition. For instance,

$$\begin{aligned}\langle n_{\mathbf{i},\sigma} n_{\mathbf{j},\bar{\sigma}} \rangle &= \langle c^{\dagger}_{\mathbf{i},\sigma} c_{\mathbf{i},\sigma} c^{\dagger}_{\mathbf{j},\bar{\sigma}} c_{\mathbf{j},\bar{\sigma}} \rangle \\ &= \langle c^{\dagger}_{\mathbf{i},\sigma} c_{\mathbf{i},\sigma} \rangle \langle c^{\dagger}_{\mathbf{j},\bar{\sigma}} c_{\mathbf{j},\bar{\sigma}} \rangle + \langle c^{\dagger}_{\mathbf{i},\sigma} c_{\mathbf{j},\bar{\sigma}} \rangle \langle c_{\mathbf{i},\sigma} c^{\dagger}_{\mathbf{j},\bar{\sigma}} \rangle \\ &= (1 - G^{\sigma,\sigma}_{\mathbf{i},\mathbf{i}})(1 - G^{\bar{\sigma},\bar{\sigma}}_{\mathbf{j},\mathbf{j}}) - G^{\sigma,\bar{\sigma}}_{\mathbf{i},\mathbf{j}} G^{\bar{\sigma},\sigma}_{\mathbf{j},\mathbf{i}} \ , \end{aligned} \tag{5.22}$$

in which $G^{\sigma,\bar{\sigma}}_{\mathbf{i},\mathbf{j}} \equiv \langle c_{\mathbf{i},\sigma} c^{\dagger}_{\mathbf{j},\bar{\sigma}} \rangle$ is the equal-time Green's function, with $\bar{\sigma} = -\sigma$.

Given this, we determine the quantum critical points, as well as the finite temperature ones by the charge correlation ratio, which we remind the reader can be written as,

$$R_{CDW} = 1 - \frac{S_{\mathrm{CDW}}(\mathbf{Q} - \delta\mathbf{q})}{S_{\mathrm{CDW}}(\mathbf{Q})} \tag{5.23}$$

where $\mathbf{Q} = (\pi, \pi)$ and $\delta\mathbf{q} = \frac{2\pi}{L}$.

5.7 DQMC Results and discussion

We begin our analysis by considering the case of fixed $\omega_0/t = 1$ and EPC $\lambda/t = 2$, while varying the RSOC parameter, α. We recall that the pure Holstein model has been extensively examined for this set of parameters, showing CDW order below a critical temperature $T_c = 0.174(2)$ [190]. The leading effects of the Rashba coupling on this charge order are illustrated in Fig. 5.9, where we show the behavior of the staggered CDW structure factor as a function of the inverse temperature, $\beta = 1/T$, for different values of α and system sizes. As the temperature decreases, the behavior of $S_{\mathrm{CDW}}(\mathbf{Q})$ changes from being weakly dependent on the system size at high temperatures to strongly dependent at low temperatures. This transition occurs approximately at the critical $T_c(\alpha)$. However, as we are dealing with finite system sizes, at very low temperatures the correlation length becomes larger than L, resulting in plateaus in $S_{\mathrm{CDW}}(\mathbf{Q})$, as shown in Fig. 5.9. Therefore, the reduction of the strength of the $S_{\mathrm{CDW}}(\mathbf{Q})$ plateuaus as α increases provides a clear evidence that Rashba coupling weakens the CDW phase. Moreover, as discussed in detail below, the energy scale at which $S_{\mathrm{CDW}}(\mathbf{Q})$ begins to increase is shifted to larger values of β, suggesting that the Rashba coupling not only affects the order parameter but also pushes the critical temperature to lower values.

To obtain the CDW order parameter, δ_{CDW}, we assume that the low-T plateaus of $S_{\mathrm{CDW}}(\mathbf{Q})$ provide a good estimate of the ground state response. Therefore, we extrapolate $\frac{S_{\mathrm{CDW}}(\mathbf{Q})}{L^2}$ as a function of $1/L$ to capture its behavior in the thermodynamic limit. That is, we employ the FSS [107]

$$\frac{S_{\mathrm{CDW}}(\mathbf{Q})}{L^2} = \delta^2_{\mathrm{CDW}} + \frac{A}{L} + \mathcal{O}(1/L^2) \ , \tag{5.24}$$

where A is a constant obtained from fitting the QMC data. This finite-size scaling analysis is shown in Fig. 5.10 (a) for different values of RSOC. The error bar for δ^2_{CDW} comes from the linear fitting.

In line with the previous discussion, Fig. 5.10 (a) demonstrates that, in the thermo-

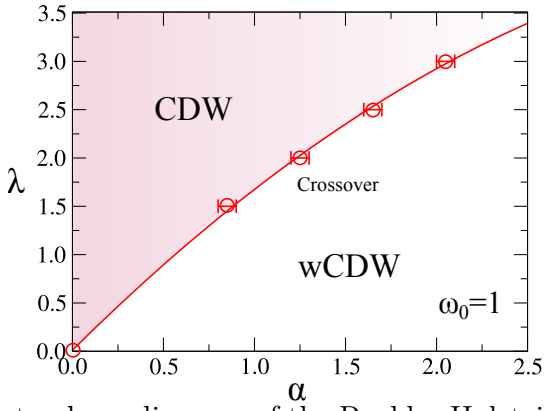

Fig. 5.11: The ground state phase diagram of the Rashba-Holstein model for fixed $\omega_0 = 1$. The solid red line is just a *crossover* between a robust CDW (magenta region) and a weak CDW (write region) one.

dynamic limit, $S_{\mathrm{CDW}}(\mathbf{Q})/L^2$ is significantly impacted by the RSOC, leading to nearly vanishing values for $\alpha/t \approx 1.3$. These results allow us to present the CDW order parameter as a function of α/t, as shown in Fig. 5.10 (b). Notice that, for small values of RSOC, the CDW response remains similar to that of the pure Holstein model, but, as α increases, the order parameter is suppressed. At this point, an important remark should be made: although Fig. 5.10 suggests a zero order parameter at $\alpha \approx 1.3$, we expect an asymptotic approach to zero instead. This expectation is based on the instability of the particle-hole channel from the nesting of the Fermi surface in the noninteracting regime, as discussed in Sec. 5.3. Indeed, weak coupling (mean-field) results, presented in Ref. [52], exhibit asymptotic behavior for the CDW order parameter in the RHM. However, such a very small order parameter response is particularly challenging to capture using QMC methods, since it demands very low temperatures.

Then, the ground state of the Rashba-Holstein model is expected to always manifest as a CDW, for any $\alpha \geq 0$. However, the strength of its order parameter (which is proportional to the charge gap at the Fermi level) depends on the RSOC, becoming exponentially small for large values of α. Therefore, for practical purposes, it is useful to identify the crossover region where the system goes from a strong CDW regime to a weak CDW (wCDW) one. Here, this crossover is identified as the point where the extrapolation

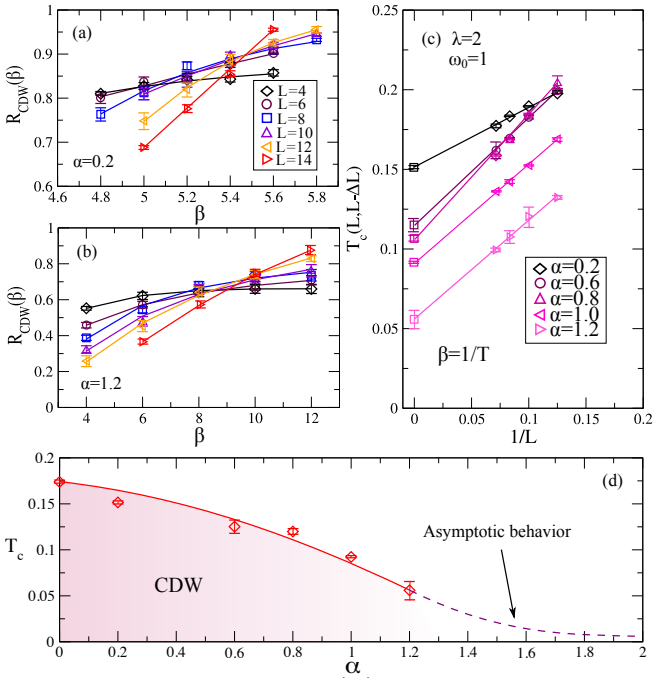

Fig. 5.12: The CDW correlation ratio $R_{CDW}(\beta)$ as a function of the inverse temperature (β=1/T), for fixed (a) $\alpha = 0.2$ and (b) $\alpha = 1.2$, and different lattice sizes. (c) The extrapolation of the crossings of the $R_{CDW}(\beta)$, between L and $L + \Delta L$ system sizes, $T_c(L, L + \Delta L)$. Here, we fixed $\Delta L = 4$. (d) The extrapolated critical temperatures of the Rashba-Holstein model for fixed $\omega_0/t = 1$. The red curve is just a guide to the eye.

of $S_{\rm CDW}(\mathbf{Q})/L^2$ vanishes, e.g. for $\lambda/t = 2$ and $\omega_0 = 1$, it is $\alpha \approx 1.25 \pm 0.05$. Identifying this crossover is important, particularly because the region with such an exponentially small order parameter is unstable to even small perturbations, such as thermal fluctuations or further neighbor hopping terms (which break the nesting of the Fermi surface), which can lead to the occurrence of a plain Rashba metal.

By repeating the same procedure outlined in Fig. 5.10, but for other values of EPC, one obtains the phase diagram of Fig. 5.11. Here, as already mentioned, the QMC points corresponds to the vanishing $\delta_{\rm CDW}$ in the thermodynamic limit, and determines the CDW-wCDW crossover. However, for a fixed low temperature (e.g., $\beta/t = 40$), this crossover line becomes a second order transition belonging to the two-dimensional Ising universality class, from a CDW phase to a Rashba metal.

It is also important to examine the finite temperature behavior, particularly to identify

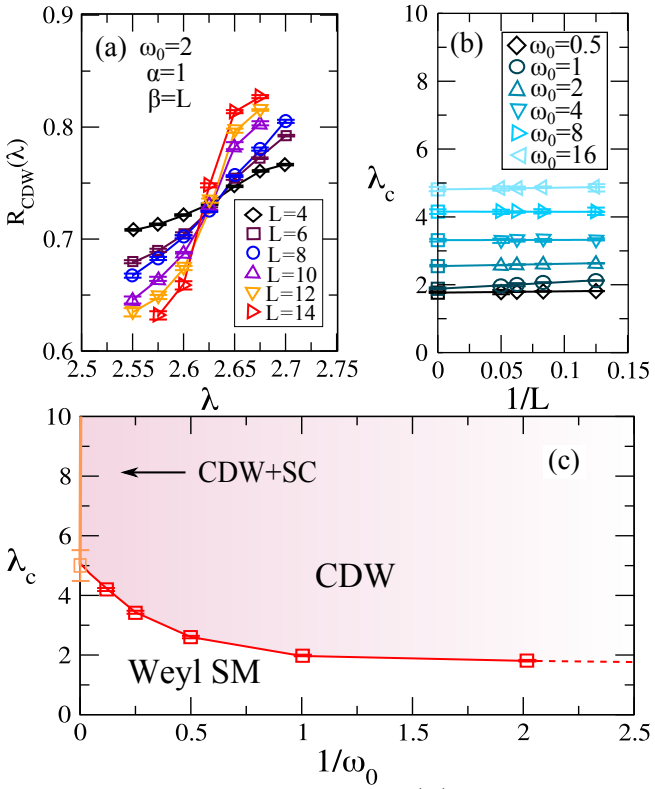

Fig. 5.13: (a) The CDW correlation ratio, $R_{CDW}(\lambda)$, as a function of λ in the limit of the pure Rashba hopping, and fixed $\omega_0/\alpha = 2$, $\beta = L$, and $\alpha = 1$. (b) The extrapolation of the crossings of the $R_{CDW}(\beta)$, between L and $L + \Delta L$ system sizes. Here, we fixed $\Delta L = 4$. (c) The phase diagram of the Rashba-Holstein model in the limit of a pure Rashba hopping. The coexistence between CDW and SC occurs only at the limit of $\omega_0 \to \infty$.

the critical temperature for the emergence of CDW, as determined by the crossings of the correlation ratio, Eq. (5.23). Figure 5.12 shows the behavior of $R_{\rm CDW}$ as a function of β for different lattice sizes, and fixed (a) $\alpha/t = 0.2$ and (b) $\alpha/t = 1.2$. In all cases, the behavior is similar: $R_{\rm CDW} \to 0$ as $\beta \to 0$, and $R_{\rm CDW} \to 1$ as $\beta \to \infty$. However, it is the crossing points for different system sizes that determine the critical value β_c. For $\alpha/t = 0.2$, these crossings occur around $\beta \approx 5.4$, while for $\alpha/t = 1.2$, they occur at larger values of β, as expected. A more precise estimate of T_c can be obtained by extrapolating these crossings to the thermodynamic limit. This is done by determining the crossing points between $R_{\rm CDW}(L)$ and $R_{\rm CDW}(L - \Delta L)$, with $\Delta L = 4$ – defining this as $T_c(L, L - \Delta L)$ – and then extrapolating to $1/L \to 0$, as illustrated in Fig. 5.12 (c). The results for T_c in the

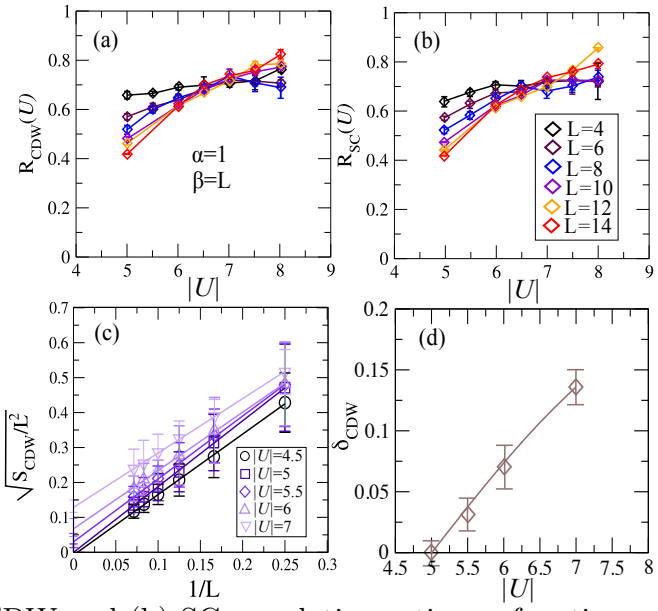

Fig. 5.14: The (a) CDW and (b) SC correlation ratios as functions of $|U|$, in the limit of the attractive Hubbard model, for the case of a pure Rashba hopping. (c) The extrapolations to the thermodynamic limit of the $\sqrt{S_{CDW}/\mathrm{L}^2}$, which leads to the order parameter presented in panel (d). The critical point is at $|U_c| = 5.0 \pm 0.5$).

thermodynamic limit are presented in Fig. 5.12 (d), where one may notice that the larger α, the lower T_c. An asymptotic behavior is also expected for T_c; however, for $\alpha/t \gtrsim 1.2$, achieving this would require $\beta t \gg 20$, which is computationally costly.

A similar asymptotic behavior is expected to occur for a different set of parameters, as long as instabilities in the particle-hole channel persist. However, this situation changes in the limit of the pure Rashba model, i.e., when $t/\alpha = 0$. As discussed earlier, in this limit there are four Weyl cones at $(0,0)$, $(\pi,0)$, $(0,\pi)$, and (π,π) for the non-interacting half-filled case. Similar to the honeycomb lattice, this vanishing density of states requires sufficiently strong electronic interactions to lead to a quantum phase transition [191, 192, 193]. Indeed, a semimetal-CDW quantum critical point (QCP) occurs for the Holstein and Hubbard-Holstein models in the half-filled honeycomb lattice [151, 152, 157], thus we expect an analogous behavior in this limit of the pure Rashba coupling.

We proceed by projecting onto the ground state, assuming Lorentz invariance and defining $\beta \propto L^z$, where $z = 1$ is the dynamic critical exponent at the QCP [193, 194, 195].

As before, the critical point is determined by the crossing of R_{CDW} for different lattice sizes, as shown in Fig. 5.13 (a). In this case, we have fixed $\beta = L$ and $\omega_0/\alpha = 2$, while varying λ, with clear crossings around $\lambda/\alpha \approx 2.62$. Following procedure as that to determining the critical temperatures, we extrapolate the crossings for the critical λ_c to the thermodynamic limit, as presented in Fig. 5.13 (b), thereby determining the QCP. We repeated this analysis for other values of ω_0 [see Fig. 5.13 (b)], which allowed us to construct the ground state phase diagram of the Rashba-Holstein model in the limit of the Weyl semimetal cones (i.e. a pure Rashba hopping), depicted in Fig. 5.13 (c). Notice that, even for high frequency (e.g., $\omega/\alpha = 16$) the ground state is either a staggered CDW or a WSM one, with no enhancement of SC or striped CDW phases.

In the adiabatic limit ($\omega_0 \to 0$), the Holstein model can be solved using a mean-field approach, as it corresponds to permanent (static) distortions in the lattice. In contrast, in the antiadiabatic limit ($\omega_0 \to \infty$), the indirect interaction between electrons becomes instantaneous, and by integrating out the phonons, one obtains the attractive Hubbard model with $|U| = \lambda$. Both limits have been previously investigated in the presence of RSOC, as discussed in Refs. [162, 163, 164, 45]. Despite this, the attractive Hubbard model with a pure Rashba hopping (i.e. $t/\alpha = 0$) has never been explored in the literature. Therefore, to complete the phase diagram in Fig. 5.13 (c), it is necessary to examine the emergence of CDW and/or SC in the limit of $\omega_0 \to \infty$.

In view of this, we employ the same ground state projection (i.e., $\beta \propto L^z$) for the attractive Hubbard model with pure Rashba hopping. Figures 5.14 (a) and (b) show the results for R_{CDW} and R_{SC} as functions of $|U|$, respectively. Here, R_{SC} is defined similarly to Eq. (5.23), but it refers to the pairing structure factor with $\mathbf{Q} = 0$, instead of the staggered one. Notice that both CDW and SC responses are identical within error bars. As discussed in Sec. 5.3, although the $SU(2)$ symmetry is broken in the presence of RSOC, in the limit of a pure Rashba hopping (i.e. $t = 0$), the $SU(2) - \eta$ symmetry is recovered in the attractive Hubbard model. Therefore, the degeneracy presented in Figs. 5.14 (a) and

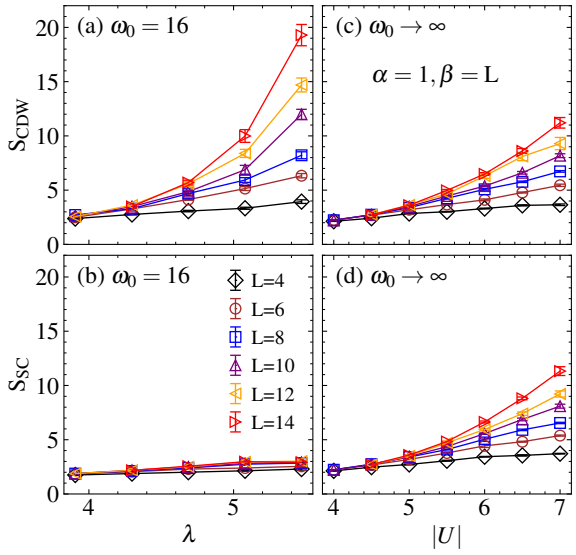

Fig. 5.15: (a) Staggered CDW structure factor and (b) homogeneous pair structure factor as functions of the electron-phonon coupling parameter, λ, for fixed $\omega_0/\alpha = 16$ and different lattice sizes. Panels (c) and (d) present the corresponding quantities for the attractive Hubbard model, and as functions of $|U|$. Both cases are in the limit of a pure Rashba hopping.

(b) are imposed by symmetry. Given this, we identify the QCP at $|U_c| \approx 5$, as shown in Fig. 5.14 (c), with the CDW (and SC) order parameters displayed in Fig. 5.14 (d).

Finally, the previous results naturally prompt the question of whether the coexistence between CDW and SC occurs only in the limit $\omega_0 \to \infty$ (symmetry-imposed), or if it can also manifest at finite frequency values (not symmetry-imposed). To address this issue, we fix $\omega_0/\alpha = 16$ and $\beta = L$, while varying λ. The results are displayed in Fig. 5.15, for the response of (a) the staggered CDW structure factor and (b) the homogeneous s-wave SC structure factor, S_{sc}. While the former shows significant enhancement for $\lambda \gtrsim 4.5$, consistent with a charge ordered ground state, the latter exhibits only weak size dependence as λ increases, indicating the absence of SC long-range order. This should be compared to the case of the attractive Hubbard model, shown in Figs. 5.15 (c) and (d), for S_{CDW} and S_{sc}, respectively. In stark contrast, both the CDW and SC structure factors exhibit significant finite-size dependence, suggesting their coexistence in this regime. Therefore, if CDW and SC coexist for finite ω_0, it likely occurs at very large frequency values or very

small temperatures.

5.8 Conclusions

In this chapter, we have studied the impact of the Rashba spin-orbit coupling to a charge-ordered system, such as the Holstein model. To this end, we investigated the Rashba-Holstein model using two methodologies: (i) a static mean-field approach, and (ii) the cluster perturbation theory – the latter provides the spectral functions of an infinite system with short-range correlations, i.e. beyond a Hartree-Fock approximation. Given this, our main findings are summarized in the phase diagrams of Figs. 5.4 and 5.7, which present the MFT and CPT results, respectively. From these, one notices that the RSOC is harmful to the CDW phase, which could be understood from the diminishing DOS at the half-filling when t_R increases, from a weak coupling point-of-view; or by a large energetic price to pay to avoid spin-flip processes (within the CDW phase), from a strong coupling point-of-view. Furthermore, as shown in Figs. 5.6 and 5.8, the transition from the CDW phase to a *correlated* Rashba metal seems to be continuous (within the resolution of the CPT method), with the transition line being pushed to larger values of t_R when $\omega_0 \to 0$. Even though the critical phenomena properties (such as critical exponents) are beyond the scope of this work, our phase diagram $g \times t_{\mathrm{R}}$ provides accurate critical points, which could be used as a first step towards less biased analyses, and whose fundamental properties may shed light into the growing class of Rashba materials [165, 166, 196].

These results are published as Ref. [52].

By seeking to go beyond MFT and CPT approaches, we employed unbiased finite-temperature Quantum Monte Carlo simulations. Within this methodology, we determined the behavior of the ground state order parameter as a function of RSOC [as shown in Fig. 5.10 (c)], which allowed us to construct the phase diagram in Fig. 5.11. Our results suggest that, due to instabilities in the particle-hole channel, the Rashba metal is unstable, and the emergence of a CDW phase is expected for any RSOC, although the CDW phase

remains relatively weak when $\alpha \gg t$. Additionally, we present the finite-temperature phase diagram in Fig. 5.12 (d), where similar asymptotic behavior is also expected at large values of RSOC.

However, the features of the model change drastically in the limit of a pure Rashba hopping, i.e., when $t/\alpha = 0$. In this limit, four Weyl cones appear at half-filling, and quantum phase transitions are expected to occur at strong interactions. Specifically, we demonstrated that the CDW phase emerges for a finite quantum critical coupling λ_c, for a given phonon frequency. By varying ω_0, the critical λ_c also changes, leading to the phase diagram shown in Fig. 5.13. At finite phonon frequencies, we expect this transition to belong to the Ising Gross-Neveu universality class with $N_f = 8$ two component Dirac cones [197, 198]. In the antiadiabatic limit where $1/\omega_0 \to 0$ the interaction corresponds to the attractive Hubbard model, with $|U| = \lambda$. In this limit, and as described in Sec. 5.3 we expect an emergent $\mathrm{SU}(2)_\eta$ symmetry the ties SC and CDW orders together. In this limit the transitions for the WSM to the massive phase corresponds to a SU(2) Gross-Neveu transtion with $N_f = 8$ two component Dirac cones. This corresponds to the same universality class as that of the Hubbard model on the honeycomb lattice [193, 194]. These findings provide a step forward in understanding the interplay between SC and CDW phases in systems with spin-orbit coupling, and we hope they could shed light on the nature of these compounds.

These results are are available as Ref. [53].

Chapter 6

Conclusions

In the course of this work, we explored superconducting phase transitions in various scenarios, employing the attractive Hubbard model (AHM) to describe the dynamics of fermion pairing on a square lattice.

Initially, through Determinant Quantum Monte Carlo (DQMC) simulations, we have mapped the relevant temperature scales of the attractive Hubbard model on a square lattice for various band fillings, $\langle n \rangle$, and interaction strengths, $|U|/t$. We have identified an optimal critical temperature region within the parameter range $|U|/t \approx 5 \pm 1$ and $\langle n \rangle \approx 0.79 \pm 0.09$, with a critical temperature $T_c \approx 0.16t$, corresponding to $T_c \approx 8.8$ nK, under experimental conditions reported in Ref. [27]. Additionally, we examined two other temperature scales: the degeneracy temperature, which marks the onset of quantum effects, and the pairing temperature, T_p, associated with the formation of pairs and gapped spin excitations. In addition, we discussed potential scenarios for the breakdown of Fermi liquid (FL) theory across the BCS-BEC crossover, analyzing double occupancy, momentum distribution functions, and quasiparticle weight. The findings suggest an FL at weak coupling that progressively transitions into a non-Fermi liquid (NFL) as unpaired fermions mediate interactions between tightly bound bosonic pairs.

However, since T_c for the square lattice remains much smaller than the experimentally accessible temperature ranges, we have explored two different routes to increase the critical superconducting temperature to one closer to the experimentally accessible ranges. The

first approach involved introducing an additional hopping degree of freedom, t_z, which connects superconducting layers. For a bilayer system, DQMC simulations shows an increase of critical temperatures between 1.5 and 1.7 times those of a single layer, under optimal conditions of fillings and on-site attraction. In addition, the effects of t_z over T_p and a pre-formed pairs region were discussed, where measurements of double occupancy via quantum gas microscopes were proposed to distinguish between metallic, pseudogap, and superconducting phases. This analysis was repeated for a simple cubic lattice, we varied t_z with respect to the isotropic case ($t_z = t$) while maintaining the same number of sites along all directions. A moderate T_c enhancement of 1.3 times the isotropic case was observed for suitable choices of t_z, U, and $\langle n \rangle$.

An alternative route considered second-neighbor hopping contributions, $t'/t < 0$, on a square lattice was also explored. DQMC results have indicated a 50% T_c increase compared to the $t' = 0$ limit for appropriate fillings and on-site attraction values. The effects of t' over the pairing temperature, T_p, and a suppression of the pseudogap region were also discussed, with the effects on the interacting DOS being shown as an alternative guide to the Metal-Pseudogap-Superconductor transition.

In the final part of this work, we explored the effects of Rashba spin-orbit coupling (RSOC), t_R, on systems with charge ordering due to electron-phonon interactions on a square lattice. Using the Holstein model framework, we examined the Rashba-Holstein Hamiltonian through various methodologies, including Mean Field theory and Cluster Perturbation Theory (CPT). We observed that RSOC weakens the charge density wave (CDW) phase. This behavior was attributed to diminished DOS at half-filling for increased t_R in the weak coupling regime and the high energetic cost of avoiding spin-flip processes in the strong coupling regime. Our phase diagram, $g \times t_R$, pinpointed critical points for the transition from the CDW phase to a correlated Rashba metal, with the transition line shifting to larger t_R values as $\omega_0 \to 0$.

We further employed finite-temperature Quantum Monte Carlo simulations on the

effective Rashba-Holstein Hamiltonian. The study of the ground state order parameter as a function of RSOC, revealed that the Rashba metal is unstable due to particle-hole channel instabilities, leading to a CDW phase even for strong RSOC, although the CDW phase weakens as $\alpha \gg t$. Additionally, we mapped the finite-temperature phase diagram, observing the asymptotic behavior for large RSOC values. In the pure Rashba hopping limit ($t/\alpha = 0$), we identified the emergence of four Weyl cones at half-filling and predicted quantum phase transitions at strong interactions. Specifically, we demonstrated that the CDW phase emerges at a finite quantum critical coupling λ_c, varying with phonon frequency ω_0.

In summary, this work has significantly deepened our understanding of superconducting transitions and the interplay of charge and spin degrees of freedom in systems with spin-orbit coupling. By suggesting novel mechanisms to enhance T_c and elucidating the role of Rashba coupling in correlated materials, we hope to inspire future experimental and theoretical investigations into these fascinating systems. Furthermore, there are issues that still need to be explored, such as a combination of the effects of layering and second neighbor hopping yet an another route to increase T_c. In addition, what happens in the Rashba-Holstein model for band fillings far from the half-filling is another interesting question to explore.

Appendix A

Determinant Quantum Monte Carlo

In this Appendix we present a brief explanation about the Determinant Quantum Monte Carlo (DQMC) method, with the technical details (e.g. Green's functions updates, matrix product stabilization, ...) being left to the references herein.

The Method: The DQMC [99, 64, 65, 66] is a numerically exact technique in which all sources of error, statistical (from finite sampling) and systematic (from the discretization of the inverse temperature β) can be removed to the desired degree of accuracy. The basic idea of the method is the use of the Trotter-Suzuki decomposition to separate the exponentials of the one-body and two-body pieces, $\hat{\mathcal{K}}$ and $\hat{\mathcal{P}}$ respectively, in the partition function, $\mathcal{Z} = \mathrm{Tr}\, e^{-\beta\hat{\mathcal{H}}} = \mathrm{Tr}\left[\left(e^{-\Delta\tau(\hat{\mathcal{K}}+\hat{\mathcal{P}})}\right)^M\right] \approx \mathrm{Tr}\left[e^{-\Delta\tau\hat{\mathcal{K}}}e^{-\Delta\tau\hat{\mathcal{P}}}e^{-\Delta\tau\hat{\mathcal{K}}}e^{-\Delta\tau\hat{\mathcal{P}}}\cdots\right]$. Here $M = \beta/\Delta\tau$ is the number of incremental time evolution operators. This decomposition has an error proportional to $(\Delta\tau)^2$ and is exact in the limit $\Delta\tau \to 0$.

For Attractive Hubbard Hamiltonian, the resulting isolation of $e^{-\Delta\tau\hat{\mathcal{P}}}$ allows for the performance of a discrete Hubbard-Stratonovich (HS) transformation, [1]

$$\begin{aligned} e^{|U|\Delta\tau\hat{n}_\uparrow\hat{n}_\downarrow} &= \frac{1}{2}e^{\frac{|U|\Delta\tau}{2}\hat{n}}\sum_{s=\pm1}e^{s\lambda\hat{m}} \\ &= \frac{1}{2}\sum_{s=\pm1}\prod_{\sigma=\uparrow,\downarrow}e^{\left(s\lambda+\frac{|U|\Delta\tau}{2}\right)\left(\hat{n}_\sigma-1/2\right)} \end{aligned} \tag{A.1}$$

where $\hat{n} = \hat{n}_\uparrow + \hat{n}_\downarrow$ and $\hat{m} = \hat{n}_\uparrow - \hat{n}_\downarrow$ are, respectively, the electron density and local magnetization operators, while $\lambda = \cosh^{-1}(e^{\frac{|U|\Delta\tau}{2}})$. In words, one can rewrite the partition

[1] To this end, one should use, e.g., the identity $\hat{n}_\uparrow\hat{n}_\downarrow = \frac{1}{2}\left(\hat{n}^2 - \hat{n}\right)$

function in quadratic (single body) form, but with the cost of introducing discrete HS auxiliary fields $s_{\mathbf{i}}(l)$ with components on each of the space and imaginary time lattice coordinates.

Thus, we may replace the on-site interaction on site of the space-time lattice by Eq. A.1, leading to the sought form in which only bilinear terms appear in the exponential. For the repulsive case we can write the partition function as,

$$\mathcal{Z} = \left(\frac{1}{2}\right)^{L^d M} \operatorname*{Tr}_{\{s\}} \prod_{M=l}^{1} \prod_{\sigma=\uparrow,\downarrow} e^{-\Delta\tau K} e^{-\Delta\tau V_\sigma(l)} \ , \tag{A.2}$$

where the traces are over Ising fields and over fermion occupancies on every site, d is the lattice dimension, L is the linear lattice size. The product from $l = M$ to 1 simply reflects the fact that earlier 'times' appear to the right. The time-slice index l appears through the HS field $s_{\mathbf{i}}(l)$ for each site $\mathbf{i}$, in

$$V_\sigma^{\mathbf{i}}(l) = \frac{1}{\Delta\tau}\lambda\sigma s_{\mathbf{i}}(l) + \left(\mu - \frac{U}{2}\right) \ , \tag{A.3}$$

which are the elements of the $N \times N$ diagonal matrix $V_\sigma(l)$, with N the number of sites.

With some algebra (see, e.g. Ref. [67]), one can integrated out the fermions and obtain

$$\begin{aligned} \mathcal{Z} &\sim \sum_{\{s_{\mathbf{i}}(l)\}} \prod_{\sigma} \det\Big[\, I + B_\sigma(M) B_\sigma(M-1) \cdots B_\sigma(1) \,\Big] \\ &\sim \operatorname*{Tr}_{\{s\}} \rho(\{s\}), \end{aligned} \tag{A.4}$$

where we have define,

$$B_\sigma(l) \equiv e^{-\Delta\tau K} e^{-\Delta\tau V_\sigma(l)} \ , \tag{A.5}$$

and the "density matrix", $\rho(\{s\})$, corresponds to the product of the determinants above. Here the identity matrix I and the matrices $B_\sigma(l)$ have the dimension of the spatial lattice size N, with the latter being the product of the exponential of the kinetic energy matrix and a diagonal matrix V_σ whose entries depend on λ, $s_{\mathbf{i}}(l)$, σ and the on-site energy U.

Then, one can measure physical quantities by sampling the HS fields with ordinary Monte Carlo techniques, where the acceptance or rejection depends on the ratio

$$r = \frac{\mathrm{det}O^{\uparrow}(\{s\}') \times \mathrm{det}O^{\downarrow}(\{s\}')}{\mathrm{det}O^{\uparrow}(\{s\}) \times \mathrm{det}O^{\downarrow}(\{s\})}, \tag{A.6}$$

with $O^{\sigma} = I + B_{\sigma}(M)B_{\sigma}(M-1)\cdots B_{\sigma}(1)$, and $\{s\}$ and $\{s\}'$ being the HS field configurations before and after a change proposal, respectively.

Now, we must discuss the calculation of average values. For two operators A and B, their equal-'time' correlation function is

$$\langle AB \rangle = \frac{1}{\mathcal{Z}} \underset{\{s\}}{\mathrm{Tr}} \mathcal{T}r \left[AB \prod_{\sigma} \prod_{l} B_{\sigma}(l) \right] , \tag{A.7}$$

where, $\mathcal{T}r$ is fermionic trace. We can define the fermionic average for a given configuration of HS field as,

$$\langle AB \rangle_{\{s\}} = \frac{1}{\rho(\{s\})} \mathcal{T}r \left[AB \prod_{\sigma,l} B_{\sigma}(l) \right] . \tag{A.8}$$

In this formulation, the two-bodies correlation function becomes,

$$\langle AB \rangle = \frac{1}{\mathcal{Z}} \underset{\{s\}}{\mathrm{Tr}} \langle AB \rangle_{\{s\}} \rho(\{s\}) . \tag{A.9}$$

The Eq. (A.9) can be used to obtain the average of the fermionic Green's function, which player a central role in this method. If we take $A \equiv c_{\mathbf{i}\sigma}$ and $B \equiv c^{\dagger}_{\mathbf{j}\sigma}$, the single particle Green's function, for a given HS field $\{s\}$, can be write as,

$$G_{\mathbf{ij},\sigma} \equiv \langle c_{\mathbf{i}\sigma} c^{\dagger}_{\mathbf{j}\sigma} \rangle_{\{s\}} = \left[(\ 1 + B_{\sigma}(M)B_{\sigma}(M-1)\cdots B_{\sigma}(1)\ )^{-1} \right]_{\mathbf{ij}} \tag{A.10}$$

Thus, for a fixed HS configuration the single particle Green's function are used to obtain the average of more than two fermionic operator, through the Wick's theorem [199]. For example,

$$\begin{aligned} \langle c^{\dagger}_{\alpha} c_{\beta} c^{\dagger}_{\gamma} c_{\delta} \rangle_{\{s\}} &= \langle c^{\dagger}_{\alpha} c_{\beta} \rangle_{\{s\}} \langle c^{\dagger}_{\gamma} c_{\delta} \rangle_{\{s\}} + \langle c^{\dagger}_{\alpha} c_{\delta} \rangle_{\{s\}} \langle c_{\beta} c^{\dagger}_{\gamma} \rangle_{\{s\}} \\ &= (1 - G_{\beta\alpha})_{\{s\}} (1 - G_{\delta\gamma})_{\{s\}} + (1 - G_{\delta\alpha})_{\{s\}} (G_{\beta\gamma})_{\{s\}} \end{aligned} \tag{A.11}$$

where the subscribe index are a combination of sites $\mathbf{i}$ and spins $\sigma =\uparrow,\downarrow$, and we are considering a system with up and down spin channels factorize, which limit the fermionic combination of the operators to case in Eq. (A.11).

The extension of this idea to the case of unequal-time correlation functions is straightforward. We start define the operators A in the Heisenberg picture, as

$$A(l) \equiv A(t) = \exp\Big(t\hat{\mathcal{H}}\Big) A \exp\Big(-t\hat{\mathcal{H}}\Big) \ , \quad t = l\Delta\tau \ , \tag{A.12}$$

so that the initial time is set to $t = \Delta\tau$ with this discretization, and $A^{\dagger}(l) \neq [A(l)]^{\dagger}$. So, the unequal-time Green's function, for $l_1 > l_2$ is write as,

$$G^{\sigma}_{\mathbf{ij}}(l_1, l_2) \equiv \langle c_{\mathbf{i}}(l_1) c^{\dagger}_{\mathbf{j}}(l_2)\rangle_{\{s\}} = [B_{\sigma}(l_1)B_{\sigma}(l_1-1)\cdots B_{\sigma}(l_2+1)g_{\sigma}(l_2+1)]_{\mathbf{ij}} \tag{A.13}$$

where,

$$g_{\sigma}(l) = [1 + B_{\sigma}(l-1)B_{\sigma}(l-2)\cdots B_{\sigma}(1)B_{\sigma}(M)\cdots B_{\sigma}(l)]^{-1} \tag{A.14}$$

The minus-sign problem: Although this is not a problem that occurs in the attractive form of the Hubbard model, it is instructive to discuss it here.

The DQMC is exact method, however its low temperature application is restricted to systems with particle-hole (PHS) or other symmetries [200]. For instance, when PHS holds, one can show [67] that $\det O^{\uparrow} \sim \det O^{\downarrow}$, which guarantees positive "Boltzmann weights". When this symmetry is broken, e.g. away from half-filling, the product of determinants in Eq. (A.4) may be negative, giving rise the infamous minus-sign problem [201, 202]. Since one cannot work with negative "Boltzmann weights", $p(c) = \det O^{\uparrow}\det O^{\downarrow}$, it constrains the use of DQMC. However, one can naively suggest that the $p(c)$ should be taken in absolute value, paying the price of multiplying by the sign of the product of determinants, i.e. $p(c) = |p(c)| \times sign(c)$. On the one hand, it circumvents the negative probabilities, on the other hand it includes noise in the measurements, since

$$\langle A\rangle = \frac{\sum_c |p(c)| sign(c) A(c)}{\sum_c |p(c)| sign(c)} = \frac{\langle A \times sign\rangle}{\langle sign\rangle}, \tag{A.15}$$

for a given quantity A; these averages become meaningless when $\langle sign \rangle \ll 1$. In summary, the eventual consequence of the minus-sign problem is to introduce strong fluctuations on the measurements, making the simulations more demanding, sometimes impractical. It is worth mentioning that such problem has not been circumvent until present time, and still is the main obstacle to a wider use of DQMC.

Appendix B

Quantities of interest

B.1 Superfluid weight

Let us consider a generic Hamiltonian as,

$$\hat{\mathcal{H}} = \hat{\mathcal{H}}_{\mathbf{k}} + \hat{\mathcal{H}}_U \ , \tag{B.1}$$

where $\hat{\mathcal{H}}_U$ is a arbitrary interaction, which can have, for instance, an onsite, or extended Hubbard form or involve an electron-photon coupling. This one, eventually can lead to a superconductor states, for example. In addition, $\hat{\mathcal{H}}_{\mathbf{k}}$ is a general single particle Hamiltonian for a multiband model, read as,

$$\hat{\mathcal{H}}_{\mathbf{k}} = \sum_{i\alpha j\beta\sigma} t_{\alpha\beta}\left(\mathbf{r}_i - \mathbf{r}_j\right) c^{\dagger}_{i\alpha\sigma} c_{j\beta\sigma} \ . \tag{B.2}$$

In this case, $t_{\alpha\beta}\left(\mathbf{r}_{i\alpha} - \mathbf{r}_{j\beta}\right)$ is the fermionic hopping matrix element, which connects the orbital β in unit cell j to the orbital α in unit cell i with $i,\ j$ cycling through all unit cells.

We are interested in the current response to a vector potential applied in the $\hat{x}$ direction, $\mathbf{A}_x(\mathbf{r}, t)$. In particular, we want to analyze the system in the long-wavelength limit $\mathbf{q} \to 0$, where $\mathbf{A}_x(\mathbf{r}, t)$ very slowly varies. This assumption, of an infinitesimally small vector potential $\mathbf{A}_x(\mathbf{r})$, ensures that we are probing the system's intrinsic properties rather than introducing artificial finite-size effects. In other words, we are probing the system's bulk behavior, rather than small-scale fluctuations that might appear at finite $\mathbf{q}$.

Let us, without loss of generality, change the notation for a generalized coordinates, where $\mathbf{R} = (\mathbf{r}_{i\alpha} + \mathbf{r}_{j\beta})/2$ and $\mathbf{r} = (\mathbf{r}_{i\alpha} - \mathbf{r}_{j\beta})$, we can rewrite the equation (B.2) as,

$$\hat{\mathcal{H}}_{\mathbf{k}} = \sum_{\mathbf{r}\alpha\beta\sigma} t_{\alpha\beta}(\mathbf{r})\, c^{\dagger}_{i\alpha\sigma} c_{j\beta\sigma} \ . \tag{B.3}$$

The vector potential $\mathbf{A}_x$ enters in a tight-binding Hamiltonian by the so-called Peierls substitution, where the gauge-invariance requires transform the creation (annihilation) operator of an electron at a site as,

$$c^{\dagger}_{i\alpha\sigma} \rightarrow c^{\dagger}_{i\alpha\sigma} \exp\left(-i\frac{e}{\hbar c}\mathcal{A}(\mathbf{r}_{i\alpha})\right) \ , \tag{B.4}$$

where $\mathcal{A}(\mathbf{r}_i)$ generates the gauge transformation of the vector potential $\mathbf{A}_x(\mathbf{r}_i) \rightarrow \mathbf{A}_x(\mathbf{r}_i) + \nabla\mathcal{A}(\mathbf{r}_i)$. Thus, using the Eq. (B.4) and (B.3), the hopping picks up the Peierls phase, as,

$$\hat{\mathcal{H}}_{\mathbf{k}} \rightarrow \hat{\mathcal{H}}_{\mathbf{k}} = \sum_{\mathbf{r}\alpha\beta\sigma} t_{\alpha\beta}(\mathbf{r}) \exp\left(-i\frac{e}{\hbar c}\left(\mathcal{A}(\mathbf{r}_{i\alpha}) - \mathcal{A}(\mathbf{r}_{j\beta})\right)\right) c^{\dagger}_{i\alpha\sigma} c_{j\beta\sigma} \ , \tag{B.5}$$

Or, in an integral way

$$\hat{\mathcal{H}}_{\mathbf{k}}(\mathbf{A}_x) = \sum_{\mathbf{r}\alpha\beta\sigma} t_{\alpha\beta}(\mathbf{r}) \exp\left(-i\frac{e}{\hbar c}\left(\int_{\mathbf{r}_{i\alpha}}^{\mathbf{r}_{j\beta}} d\mathbf{r}'\mathbf{A}_x(\mathbf{r}')\right)\right) c^{\dagger}_{i\alpha\sigma} c_{j\beta\sigma} \ . \tag{B.6}$$

Thus, we assume that the vector potential varies slowly over the hopping distance, which enable us expand $\mathbf{A}_x(\mathbf{r}')$ around the midpoint $\mathbf{R}$ as

$$\mathbf{A}_x(\mathbf{r}') = \mathbf{A}_x(\mathbf{R}) + (\mathbf{r}' - \mathbf{R})\nabla\mathbf{A}_x(\mathbf{R}) + \mathcal{O}(|\mathbf{r}' - \mathbf{R}|^2) \ , \tag{B.7}$$

where we will neglect higher order terms of $\mathbf{R}$, contained in $\mathcal{O}$. So, substituting the Taylor expansion, Eq. (B.7), into the integral of the Eq. (B.6), we can write,

$$\begin{aligned}\int_{\mathbf{r}_{i\alpha}}^{\mathbf{r}_{j\beta}} d\mathbf{r}'\mathbf{A}_x(\mathbf{r}') &\approx \int_{\mathbf{r}_{i\alpha}}^{\mathbf{r}_{j\beta}} d\mathbf{r}' \left[\mathbf{A}_x(\mathbf{R}) + (\mathbf{r}' - \mathbf{R})\nabla\mathbf{A}_x(\mathbf{R})\right] \\ &= \int_{\mathbf{r}_{i\alpha}}^{\mathbf{r}_{j\beta}} d\mathbf{r}' \left[\mathbf{A}_x(\mathbf{R})\right] + \int_{\mathbf{r}_{i\alpha}}^{\mathbf{r}_{j\beta}} d\mathbf{r}' \left[(\mathbf{r}' - \mathbf{R})\nabla\mathbf{A}_x(\mathbf{R})\right]\end{aligned} \tag{B.8}$$

where, since $\mathbf{r}' - \mathbf{R}$ is symmetric around the midpoint, the second integral in the right side of the Eq. (B.8) vanishes in the first-order approximation. The integral can be

approximated for,

$$\int_{\mathbf{r}_{i\alpha}}^{\mathbf{r}_{j\beta}} d\mathbf{r}' \mathbf{A}_x(\mathbf{r}') \approx \mathbf{A}_x(\mathbf{R}) \cdot (\mathbf{r}_{j\beta} - \mathbf{r}_{i\alpha})$$

or,

$$\int_{\mathbf{r}_{i\alpha}}^{\mathbf{r}_{j\beta}} d\mathbf{r}' \mathbf{A}_x(\mathbf{r}') \approx \mathbf{A}_x(\mathbf{R}) \cdot \mathbf{r} \tag{B.9}$$

Thus, in the long-wavelength limit, the phase accumulated by an electron hopping from site i to j is effectively determined by the vector potential at the midpoint of the hopping path.

Using the Eq. (B.9), we can rewrite Eq. (B.6) as,

$$\hat{\mathcal{H}}_{\mathbf{k}}(\mathbf{A}_x) = \sum_{\mathbf{R}\mathbf{r}\alpha\beta\sigma} t_{\alpha\beta}(\mathbf{r}) \exp\left(-i\frac{e}{\hbar}\mathbf{A}_x(\mathbf{R}) \cdot \mathbf{r}\right) c^{\dagger}_{i\alpha\sigma} c_{j\beta\sigma} \ , \tag{B.10}$$

where, for simplicity, we have take $c = 1$.

Within linear response theory, we can further Taylor expand the exponential, retaining terms which are linear (paramagnetic) and quadratic (diamagnetic) in $\mathbf{A}$,

$$\exp\left(-i\frac{e}{\hbar}\mathbf{A}_x(\mathbf{R}) \cdot \mathbf{r}\right) \approx 1 - i\frac{e}{\hbar}\mathbf{A}_x(\mathbf{R}) \cdot \mathbf{r} - \frac{e^2}{2\hbar^2}\left(\mathbf{A}_x(\mathbf{R}) \cdot \mathbf{r}\right)^2 + \mathcal{O}(\mathbf{A}_x^3) \ . \tag{B.11}$$

Of the Eq. (B.11) into Eq. (B.10), we can write,

$$\begin{aligned}\hat{\mathcal{H}}_{\mathbf{k}}(\mathbf{A}_x) &\approx \sum_{\mathbf{R}\mathbf{r}\alpha\beta\sigma} t_{\alpha\beta}(\mathbf{r}) \left(1 - i\frac{e}{\hbar}\mathbf{A}_x(\mathbf{R}) \cdot \mathbf{r} - \frac{e^2}{2\hbar^2}\left(\mathbf{A}_x(\mathbf{R}) \cdot \mathbf{r}\right)^2\right) c^{\dagger}_{i\alpha\sigma} c_{j\beta\sigma} \\ &= \hat{\mathcal{H}}_{\mathbf{k}} - \sum_{\mathbf{R}\mathbf{r}\alpha\beta\sigma} t_{\alpha\beta}(\mathbf{r}) \left[i\frac{e}{\hbar}\left(\mathbf{A}_x(\mathbf{R}) \cdot \mathbf{r}\right) c^{\dagger}_{i\alpha\sigma} c_{j\beta\sigma} + \frac{e^2}{2\hbar^2}\left(\mathbf{A}_x(\mathbf{R}) \cdot \mathbf{r}\right)^2 c^{\dagger}_{i\alpha\sigma} c_{j\beta\sigma}\right] \ ,\end{aligned} \tag{B.12}$$

where the first and second terms into the sum, in the right side of the Eq. (B.12), are relations to paramagnetic (P) and diamagnetic (D) current contribution, respectively, as will become clear below.

In what follows, the current density operator is obtained from the Hamiltonian as,

$$\mathbf{j}_x(\mathbf{r}) = \frac{\delta \hat{\mathcal{H}}_k(\mathbf{A}_x)}{\delta \mathbf{A}_x} \tag{B.13}$$

Thus, differentiating the Hamiltonian, we have,

$$j_x(\mathbf{r}) = i\frac{e}{\hbar}\sum_{i\alpha j\beta\sigma}\left(r_{i\alpha}-r_{j\beta}\right)_x t_{\alpha\beta}\left(\mathbf{r}_{i\alpha j\beta}\right)c^{\dagger}_{i\alpha\sigma}c_{j\beta\sigma} + \frac{e^2}{\hbar^2}\sum_{i\alpha j\beta\sigma}\left(r_{i\alpha}-r_{j\beta}\right)^2_x t_{\alpha\beta}\left(\mathbf{r}_{i\alpha j\beta}\right)A_x(\mathbf{R}_{i\alpha j\beta})c^{\dagger}_{i\alpha\sigma}c_{j\beta\sigma}\ . \tag{B.14}$$

Applying a Fourier transform to operators, we have,

$$c^{\dagger}_{i\alpha} = \frac{1}{\sqrt{V}}\sum_{\mathbf{k}}\exp\left(-i\mathbf{k}\cdot\mathbf{r}_{i\alpha}\right)c^{\dagger}_{\mathbf{k}\alpha} \tag{B.15}$$

Where V is the volume of the system. So, Eq. (B.14) is rewrite as,

$$j_x(\mathbf{q}) = i\frac{e}{V\hbar}\sum_{\mathbf{k}_1\mathbf{k}_2 i\alpha j\beta\sigma}\left(r_{i\alpha}-r_{j\beta}\right)_x t_{\alpha\beta}\left(\mathbf{r}_{i\alpha j\beta}\right)\exp\left[-i\left(\mathbf{k}_1-\mathbf{k}_2\right)\cdot\mathbf{r}_{i\alpha j\beta}\right]c^{\dagger}_{\mathbf{k}_1\alpha\sigma}c_{\mathbf{k}_2\beta\sigma} + \frac{e^2}{V\hbar^2}\sum_{\mathbf{k}_1\mathbf{k}_2 i\alpha j\beta\sigma}\left(r_{i\alpha}-r_{j\beta}\right)^2_x t_{\alpha\beta}\left(\mathbf{r}_{i\alpha j\beta}\right)A_x(\mathbf{R}_{i\alpha j\beta})\exp\left[-i\left(\mathbf{k}_1-\mathbf{k}_2\right)\cdot\mathbf{r}_{i\alpha j\beta}\right]c^{\dagger}_{\mathbf{k}_1\alpha\sigma}c_{\mathbf{k}_2\beta\sigma} \tag{B.16}$$

Remind that we can rewrite the sum over site index as sum over $\mathbf{r}$, and so, the Fourier transform of hopping matrix element is $t_{\alpha\beta}(\mathbf{k}) = \sum_{\mathbf{r}} t_{\alpha\beta}(\mathbf{r})e^{-i\mathbf{k}\cdot\mathbf{r}}$. Thus, make $\mathbf{k} = \frac{\mathbf{k}_1+\mathbf{k}_2}{2}$ and $\mathbf{q} = \mathbf{k}_1 - \mathbf{k}_2$, the Eq. (B.16) becomes,

$$j_x(\mathbf{q}) = \frac{e}{V\hbar}\sum_{\mathbf{k}\alpha\beta\sigma}\frac{\partial t_{\alpha\beta}(\mathbf{k})}{\partial k_x}c^{\dagger}_{\mathbf{k}+\mathbf{q}/2,\alpha\sigma}c_{\mathbf{k}-\mathbf{q}/2,\beta\sigma} + \frac{e^2}{V\hbar^2}\sum_{\mathbf{k}\alpha\beta\sigma}\frac{\partial^2 t_{\alpha\beta}(\mathbf{k})}{\partial k_x^2}A_x(\mathbf{q})c^{\dagger}_{\mathbf{k},\alpha\sigma}c_{\mathbf{k},\beta\sigma} \tag{B.17}$$

or, in a formal way as,

$$j_x(\mathbf{q}) = j_x^P(\mathbf{q}) + j_x^D(\mathbf{q}) \tag{B.18}$$

where, the P and D index indicate the Paramagnetic and Diamagnetic current contribution, with j_x^P and j_x^D are the first and second terms, in the right side, of the Eq. (B.17).

Let us use the standard linear response theory and Kubo formula to write the response of the current to an external vector potential must be write as,

$$\langle j_x\rangle(\mathbf{q},\omega) = \int dt'\chi_{j_x j_x}(\mathbf{q},t-t')A_x(\mathbf{q},t')\ . \tag{B.19}$$

Where, for a imaginary time notation and taking the static long-wavelength limit, the Eq. (B.19) can be read as,

$$\langle j_x \rangle (\mathbf{q}, \omega = 0) = \frac{-4e^2}{\hbar} \rho_s A_x(\mathbf{q}, \omega = 0) \ , \tag{B.20}$$

with, ρ_s the superfluid stiffness, which is associated with the free-energy cost of distorting the phase of the SC order parameter $|\Delta|e^{i\phi}$ via the Boltzmann factor $\exp\left(-\rho_s \int d\mathbf{r} |\nabla\theta|^2 / 2k_B T\right)$. This quantity can be defined as

$$\rho_s = \tilde{\rho} - \frac{\hbar^2}{4e^2} \Lambda^T_{xx}(\mathbf{q} \to 0, \omega = 0) \ , \tag{B.21}$$

where $\tilde{\rho}$ is proportional to longitudinal current response, due to diamagnetic current contribution, and $\Lambda^T_{xx}(\mathbf{q} \to 0, \omega = 0)$ the transverse paramagnetic current-current correlation function, where

$$\Lambda_{xx}(\mathbf{q} \to 0, \omega_n = 0) = \lim_{\mathbf{q}\to 0} \sum_{\mathbf{r}} \int_0^\beta d\tau \, e^{i\mathbf{q}\cdot\mathbf{r}} e^{i\omega_n \tau} \Lambda_{xx}(\mathbf{r}, \tau) \ . \tag{B.22}$$

where $\omega_n = 2n\pi T$ are the Matsubara frequencies, $\beta = 1/k_B T$ and

$$\Lambda_{xx}(\mathbf{r}, \tau) = \langle j_x(\mathbf{r}, \tau) j_x(0, 0) \rangle \ , \tag{B.23}$$

is the current-current correlation function.

The analysis of the general form of each term in right-hand side of Eq. (B.21) is more complicated; see Ref. [104] for more details. Thus, let us take the simple case of a square lattice system, for instance, for the single-band limit, which enable us write, up to constant factors, an analogous expression to Eq. (2.8),

$$\rho_s = \frac{1}{4\Omega} \sum_{\mathbf{k}\sigma} \frac{\partial^2 \varepsilon(\mathbf{k})}{\partial k_x^2} n(\mathbf{k}) - \frac{1}{4} \Lambda^T_{xx}(\mathbf{q} \to 0, \omega = 0) \ , \tag{B.24}$$

where, $n(\mathbf{k}) = \langle c^\dagger_{\mathbf{k}\sigma} c_{\mathbf{k}\sigma} \rangle$, Ω is the lattice area, and for a square lattice with nearest-neighbor hopping only, $\varepsilon(\mathbf{k}) = -2t\,(\cos k_x + \cos k_y)$. Thus, we must rewrite the Eq. (B.24) as

$$\rho_s = \frac{1}{4} \left[\langle -K_x \rangle - \Lambda^T_{xx}(\mathbf{q} \to 0, \omega = 0) \right] \ , \tag{B.25}$$

where $\langle -K_x \rangle$ is proportional to the kinetic energy in the $\hat{x}$ direction, represents the diamagnetic part of the response.

The parallel between Eq. (2.8) and Eq. (B.25) is complete, noting the fact that

$$\Lambda^L \equiv \lim_{q_x \to 0} \Lambda_{xx}(q_x, q_y = 0, \omega_n = 0) = \langle -K_x \rangle, \tag{B.26}$$

and

$$\Lambda^T_{xx}(\mathbf{q} \to 0, \omega = 0) \to \Lambda^T_{xx} \equiv \lim_{q_y \to 0} \Lambda_{xx}(q_x = 0, q_y, \omega_n = 0). \tag{B.27}$$

See the Ref. [203, 71] for more details.

B.2 Correlation Ratio

In the context of continuous phase transitions, several quantities display singular behavior in the thermodynamic limit at a critical temperature, T_c, characterized by critical exponents. For instance, a generic quantity usually diverges as $X \sim |T - T_c|^{-x}$, where x is the associated critical exponent; in particular, the correlation length behaves as $\xi \sim |T - T_c|^{-\nu}$. However, in systems with finite linear sizes, L, these divergences are rounded, and their limit as $L \to \infty$ is described quite generically by a finite-size scaling (FSS) theory [204, 205, 206], which is based on the fact that the two important length scales are ξ and L, so that X follows a scaling ansatz,

$$X(L, T) = L^{x/\nu} \mathcal{F}(L/\xi),\ T \to T_c,\ L \to \infty. \tag{B.28}$$

In particular, at $T = T_c$ we see that $L^{-x/\nu} X(L, T_c)$ is size-invariant, and could be used to determine T_c, if x and ν were known, which is not usually the case. However, we may use instead a *dimensionless* quantity, $Y(L, T)$, related to X (so that $y = 0$) with which we can estimate T_c without the previous knowledge of x and ν. The quest for such quantity begins with the structure factor associated with the relevant order parameter: in the thermodynamic limit, it diverges at a characteristic ordering wavevector, $\mathbf{q}$, as the critical temperature is approached, i.e., the peak gets narrower and larger. Thus, with

a structure factor, $S(\mathbf{q})$, we may form a dimensionless quantity, the so-called correlation ratio, R_c, which is scale (or size-) invariant at the critical point,

$$R_c(L,\beta) = 1 - \frac{S(\mathbf{q}+\delta\mathbf{q})}{S(\mathbf{q})}, \tag{B.29}$$

where $\mathbf{q}+\delta\mathbf{q}$ is a point in reciprocal space close to $\mathbf{q}$. Equation (B.29) therefore follows the FSS ansatz, Eq. (B.28), with $x = 0$, and can then be used to estimate T_c from plots of $R_c(\beta)$ for different L's. For the case at hand, we use the uniform, $\mathbf{q} = \mathbf{0}$, s-wave pairing structure factor, $P_s(\mathbf{q})$, to calculate $R_c(L,\beta)$.

Appendix C

Cluster Perturbation Theory - CPT

The CPT method is based in partition an original lattice γ into an infinite number of finite clusters formed by L sites. This corresponds to forming a superlattice Γ with L sites in its basis [184, 207]. Within this approach, one can decompose the Hamiltonian of the system as

$$H = H_{\text{cluster}} + T \ , \tag{C.1}$$

where

$$H_{\text{cluster}} = \sum_{\alpha,\beta} t_{\alpha,\beta} c_{\alpha}^{\dagger} c_{\beta} + H_{\text{U,loc}}, \tag{C.2}$$

accounts for the terms of the Hamiltonian that act inside each cluster (intracluster terms), and

$$T = \sum_{\alpha,\beta} V_{\alpha,\beta} c_{\alpha}^{\dagger} c_{\beta} \tag{C.3}$$

is the term that connects different clusters of the superlattice (intercluster terms). In Eq. (C.2) $t_{\alpha,\beta}$ are one-particle matrix-elements of intracluster term. $H_{\text{U,loc}}$ is the term responsible for the many-body nature of the problem. To permit the application of the CPT method it is necessary that $H_{\text{U,loc}}$ involve only on-site bosonic and fermionic operators, i.e., it must be a local interaction term. Two examples of such terms are the Hubbard electron-electron interaction and the Holstein electron-phonon coupling, the latter being

the object of study in the present work. Once we constrain ourselves to local interactions, the intercluster term (Eq. C.3) involves only one-particle operators with matrix elements $V_{\alpha,\beta}$. With this, one can write the Green function of Hamiltonian as

$$\mathbf{G}(\omega)^{-1} = \mathbf{G}'(\omega)^{-1} - \mathbf{V}, \tag{C.4}$$

where, $\mathbf{G}(\omega)$ is the Green function of the complete Hamiltonian, $\mathbf{G}'(\omega)$ is the exact Green function of the intra-cluster term. The cluster superlattice has a reduced Brillouin zone. One can connect any wavevector $\mathbf{k}$ of the original Brillouin zone to a wavevector $\tilde{\mathbf{k}}$ in the reduced one by $\mathbf{k} = \tilde{\mathbf{k}} + \mathbf{K}$ where $\mathbf{K}$ is an element of the reciprocal superlattice. Eq. (C.4) in the reduced Brillouin zone is given by

$$\mathbf{G}(\tilde{\mathbf{k}}, \omega)^{-1} = \mathbf{G}'(\omega)^{-1} - \mathbf{V}(\tilde{\mathbf{k}}). \tag{C.5}$$

One can calculate the CPT Green function by

$$G_{\mathrm{CPT}}(\mathbf{k}, \omega) = \frac{1}{L} \sum_{a,b} e^{-i\mathbf{k}(\mathbf{r}_a - \mathbf{r}_b)} G_{a,b}(\tilde{\mathbf{k}}, \omega) \tag{C.6}$$

where $\mathbf{r}_{a(b)}$ is the position of sites inside the cluster. The CPT Green function takes into account the leading order in the interaction term and allows the evaluation of the variety spectral quantities. Here, we focus on spectral weight, which is read as

$$A_0(\mathbf{k}, \omega) = -\frac{1}{2\pi} \mathrm{Im}[G_{\mathrm{CPT}}(\mathbf{k}, \omega)], \tag{C.7}$$

from which one can compute the density of states (DOS)

$$N(\omega) = \frac{1}{N} \sum_{\mathbf{k}} A_0(\mathbf{k}, \omega). \tag{C.8}$$

We used the DOS in the main text study of the transition from Rashba metal to the gapped CDW phase induced by EPC.

In Eqs. (C.1-C.8), we assume spinless Fermions. In the Holstein-Rashba model, the RSOC generates a spin texture, turning necessary to adapt these equations by including

additional spin indexes on Eqs. (C.1-C.5). The intercluster hopping matrix for Holstein-Rashba Hamiltonian [Eq. (5.1)] is given by,

$$V(\tilde{\mathbf{k}}) = (e^{-2i\tilde{\mathbf{k}}_x})(t\sigma_z + it_R\sigma_y) \otimes \Delta_x + (e^{-2i\tilde{\mathbf{k}}_y})(t\sigma_z - it_R\sigma_x) \otimes \Delta_y + \text{h.c.} \tag{C.9}$$

where Δ_x and Δ_x denotes the $\hat{x}$ and $\hat{y}$ unitary translation operators in the cluster. In the presence of RSOC, the CPT Green function becomes a matrix with dimension 2 with each matrix element $[\mathbf{G}_{\text{CPT}}(\mathbf{k},\omega)]_{\sigma,\sigma'}$ given by Eq. (C.6). Also, one includes an additional trace over spin indices in Eqs. (C.7, C.8). We can also define a spin-polarized spectral weight

$$A_\mu(\omega,\mathbf{k}) = -\frac{1}{2\pi}\text{Im}\left(\text{Tr}[\mathbf{G}_{\text{CPT}}(\mathbf{k},\omega)\cdot\sigma_\mu]\right), \tag{C.10}$$

where $\mu = x, y, z$. This function gives information on spin-polarized electronic excitation spectra.

In the results presented in the main text, we used 2×2 clusters ($L = 4$). The unconstrained size of bosonic Hilbert space turns necessary the use of a cut-off in the number of phonons per site. To reach the convergence of our results, we used a cutoff on the phonon number that varies from 10 to 16 depending on the value of EPC. The study of larger clusters using this method is computationally demanding. As discussed in the main text, the cluster size should not affect the position of critical points on the CPT phase diagram but should affect the pair correlation functions.

Bibliography

[1] Thomas Hartke, Botond Oreg, Carter Turnbaugh, Ningyuan Jia, and Martin Zwierlein. Direct observation of nonlocal fermion pairing in an attractive Fermi-Hubbard gas. *Science*, 381(6653):82–86, 2023.

[2] I. Bloch, J. Dalibard, and W. Zwerger. Many-body physics with ultracold gases. *Rev. Mod. Phys.*, 80:885, Jul 2008.

[3] J. Bardeen, L. N. Cooper, and J. R. Schrieffer. Theory of superconductivity. *Phys. Rev.*, 108:1175–1204, Dec 1957.

[4] Leon N. Cooper. Bound Electron Pairs in a Degenerate Fermi Gas. *Phys. Rev.*, 104:1189–1190, Nov 1956.

[5] J. G. Bednorz and K. A. Müller. Possible high-T_c superconductivity in the BaLaCuO system. *Zeitschrift für Physik B Condensed Matter*, 64(2):189–193, Jun 1986.

[6] A.S. Alexandrov and P.P. Edwards. High-T_c cuprates: a new electronic state of matter? *Physica C: Superconductivity*, 331(2):97–112, 2000.

[7] Kyle M. Shen and J.C. Seamus Davis. Cuprate high-T_c superconductors. *Materials Today*, 11(9):14–21, 2008.

[8] Dale R Harshman, Anthony T Fiory, and John D Dow. Theory of high-T_c superconductivity: transition temperature. *Journal of Physics: Condensed Matter*, 23(29):295701, jul 2011.

[9] Zuo-Dong Yu, Yuan Zhou, Wei-Guo Yin, Hai-Qing Lin, and Chang-De Gong. Phase competition and anomalous thermal evolution in high-temperature superconductors. *Phys. Rev. B*, 96:045110, Jul 2017.

[10] Yuan Cao, Valla Fatemi, Shiang Fang, Kenji Watanabe, Takashi Taniguchi, Efthimios Kaxiras, and Pablo Jarillo-Herrero. Unconventional superconductivity in magic-angle graphene superlattices. *Nature*, 556(7699):43–50, Apr 2018.

[11] Myungchul Oh, Kevin P. Nuckolls, Dillon Wong, Ryan L. Lee, Xiaomeng Liu, Kenji Watanabe, Takashi Taniguchi, and Ali Yazdani. Evidence for unconventional superconductivity in twisted bilayer graphene. *Nature*, 600(7888):240–245, Dec 2021.

[12] Aaron Chew, Yijie Wang, B. Andrei Bernevig, and Zhi-Da Song. Higher-order topological superconductivity in twisted bilayer graphene. *Phys. Rev. B*, 107:094512, Mar 2023.

[13] Maryam Khosravian, Elena Bascones, and Jose L Lado. Moiré-enabled topological superconductivity in twisted bilayer graphene. *2D Materials*, 11(3):035012, apr 2024.

[14] Hualei Sun, Mengwu Huo, Xunwu Hu, Jingyuan Li, Zengjia Liu, Yifeng Han, Lingyun Tang, Zhongquan Mao, Pengtao Yang, Bosen Wang, Jinguang Cheng, Dao-Xin Yao, Guang-Ming Zhang, and Meng Wang. Signatures of superconductivity near 80 k in a nickelate under high pressure. *Nature*, 621(7979):493–498, Sep 2023.

[15] Matthias Hepting. Nickelates join the club of high-temperature superconductors. *Nature*, 621(7979):475–476, September 2023.

[16] Mohit Randeria, Nandini Trivedi, Adriana Moreo, and Richard T. Scalettar. Pairing and spin gap in the normal state of short coherence length superconductors. *Phys. Rev. Lett.*, 69:2001–2004, Sep 1992.

[17] Raimundo R. dos Santos. Spin gap and superconductivity in the three-dimensional attractive Hubbard model. *Phys. Rev. B*, 50:635–638, Jul 1994.

[18] Thereza Paiva, Richard Scalettar, Mohit Randeria, and Nandini Trivedi. Fermions in 2d optical lattices: Temperature and entropy scales for observing antiferromagnetism and superfluidity. *Phys. Rev. Lett.*, 104:066406, Feb 2010.

[19] John A. Wilson. Developments in the negative-U modelling of the cuprate HTSC systems. *Journal of Physics: Condensed Matter*, 13(50):R945–R977, nov 2001.

[20] R. Micnas, J. Ranninger, and S. Robaszkiewicz. Superconductivity in narrow-band systems with local nonretarded attractive interactions. *Rev. Mod. Phys.*, 62:113–171, Jan 1990.

[21] Mohit Randeria. *Bose–Einstein Condensation*, chapter Crossover from BCS Theory to Bose-Einstein Condensation, pages 355–392. Cambridge University Press, Cambridge, 1995.

[22] Qijin Chen, Jelena Stajic, Shina Tan, and K. Levin. BCS-BEC crossover: From high temperature superconductors to ultracold superfluids. *Physics Reports*, 412(1):1 – 88, 2005.

[23] Mohit Randeria and Edward Taylor. Crossover from Bardeen-Cooper-Schrieffer to Bose-Einstein condensation and the unitary Fermi gas. *Annual Review of Condensed Matter Physics*, 5(1):209–232, 2014.

[24] Agnieszka Górecka, Benoît Grémaud, and Christian Miniatura. Synthetic magnetic fluxes on the honeycomb lattice. *Phys. Rev. A*, 84:023604, Aug 2011.

[25] Gyu-Boong Jo, Jennie Guzman, Claire K. Thomas, Pavan Hosur, Ashvin Vishwanath, and Dan M. Stamper-Kurn. Ultracold atoms in a tunable optical kagome lattice. *Phys. Rev. Lett.*, 108:045305, Jan 2012.

[26] Jin-Yu Liu, Guang-Quan Luo, Xiao-Qiong Wang, Andreas Hemmerich, and Zhi-Fang Xu. Experimental realization of a high precision tunable hexagonal optical lattice. *Opt. Express*, 30(25):44375–44384, Dec 2022.

[27] Debayan Mitra, Peter T. Brown, Elmer Guardado-Sanchez, Stanimir S. Kondov, Trithep Devakul, David A. Huse, Peter Schauss, and Waseem S. Bakr. Quantum gas microscopy of an attractive Fermi-Hubbard system. *Nature Physics*, 14(2):173–177, 2018.

[28] Herman Feshbach. Unified theory of nuclear reactions. *Annals of Physics*, 5(4):357–390, 1958.

[29] Cheng Chin, Rudolf Grimm, Paul Julienne, and Eite Tiesinga. Feshbach resonances in ultracold gases. *Rev. Mod. Phys.*, 82:1225–1286, Apr 2010.

[30] T. P. Billam, A. L. Marchant, S. L. Cornish, S. A. Gardiner, and N. G. Parker. *Bright Solitary Matter Waves: Formation, Stability and Interactions*, pages 403–455. Springer Berlin Heidelberg, Berlin, Heidelberg, 2013.

[31] M. Houbiers, H. T. C. Stoof, W. I. McAlexander, and R. G. Hulet. Elastic and inelastic collisions of ^{6}Li atoms in magnetic and optical traps. *Phys. Rev. A*, 57:R1497–R1500, Mar 1998.

[32] J Hecker Denschlag, J E Simsarian, H Häffner, C McKenzie, A Browaeys, D Cho, K Helmerson, S L Rolston, and W D Phillips. A bose-einstein condensate in an optical lattice. *Journal of Physics B: Atomic, Molecular and Optical Physics*, 35(14):3095, jul 2002.

[33] Oliver Morsch and Markus Oberthaler. Dynamics of Bose-Einstein condensates in optical lattices. *Rev. Mod. Phys.*, 78:179–215, Feb 2006.

[34] W. Hofstetter, J. I. Cirac, P. Zoller, E. Demler, and M. D. Lukin. High-temperature superfluidity of fermionic atoms in optical lattices. *Phys. Rev. Lett.*, 89:220407, Nov 2002.

[35] Ehud Altman and Assa Auerbach. Oscillating superfluidity of bosons in optical lattices. *Phys. Rev. Lett.*, 89:250404, Dec 2002.

[36] J. K. Chin, D. E. Miller, Y. Liu, C. Stan, W. Setiawan, C. Sanner, K. Xu, and W. Ketterle. Evidence for superfluidity of ultracold fermions in an optical lattice. *Nature*, 443(7114):961–964, Oct 2006.

[37] C.A. Regal and D.S. Jin. Experimental Realization of the BCS-BEC Crossover with a Fermi Gas of Atoms. volume 54 of *Advances In Atomic, Molecular, and Optical Physics*, pages 1–79. Academic Press, 2007.

[38] Thereza Paiva, Raimundo R. dos Santos, R. T. Scalettar, and P. J. H. Denteneer. Critical temperature for the two-dimensional attractive Hubbard model. *Phys. Rev. B*, 69:184501, May 2004.

[39] Rodrigo A. Fontenele, Natanael C. Costa, Raimundo R. dos Santos, and Thereza Paiva. Two-dimensional attractive Hubbard model and the BCS-BEC crossover. *Phys. Rev. B*, 105:184502, May 2022.

[40] Piotr Magierski, Gabriel Wlazłowski, Aurel Bulgac, and Joaquín E. Drut. Finite-Temperature Pairing Gap of a Unitary Fermi Gas by Quantum Monte Carlo Calculations. *Phys. Rev. Lett.*, 103:210403, Nov 2009.

[41] Piotr Magierski, Gabriel Wlazłowski, and Aurel Bulgac. Onset of a Pseudogap regime in Ultracold Fermi Gases. *Phys. Rev. Lett.*, 107:145304, Sep 2011.

[42] Gabriel Wlazłowski, Piotr Magierski, Joaquín E. Drut, Aurel Bulgac, and Kenneth J. Roche. Cooper Pairing Above the Critical Temperature in a Unitary Fermi Gas. *Phys. Rev. Lett.*, 110:090401, Feb 2013.

[43] Hiroyuki Tajima, Takashi Kashimura, Ryo Hanai, Ryota Watanabe, and Yoji Ohashi. Uniform spin susceptibility and spin-gap phenomenon in the BCS-BEC-crossover regime of an ultracold Fermi gas. *Phys. Rev. A*, 89:033617, Mar 2014.

[44] B. L. Kang, M. Z. Shi, S. J. Li, H. H. Wang, Q. Zhang, D. Zhao, J. Li, D. W. Song, L. X. Zheng, L. P. Nie, T. Wu, and X. H. Chen. Preformed cooper pairs in layered $FeSe$-Based Superconductors. *Phys. Rev. Lett.*, 125:097003, Aug 2020.

[45] Rodrigo A. Fontenele, Natanael C. Costa, Thereza Paiva, and Raimundo R. dos Santos. Increasing superconducting T_c by layering in the attractive Hubbard model. *Phys. Rev. A*, 110:053315, Nov 2024.

[46] Rodrigo Alves Fontenele, Nathan Vasconcelos, Natanael Carvalho Costa, Thereza Paiva, and Raimundo Rocha dos Santos. Second-Neighbor Hopping Effects in the Two-Dimensional Attractive Hubbard Model. *Condensed Matter*, 8(1), 2023.

[47] Rodrigo A. Fontenele, Natanael C. Costa, Thereza Paiva, and Raimundo R. dos Santos. Effects of next-nearest neighbor hopping on the pairing and critical temperatures of the attractive Hubbard model on a square lattice. *arXiv:2503.06753*, 2025.

[48] G. Grüner. The dynamics of charge-density waves. *Rev. Mod. Phys.*, 60:1129–1181, Oct 1988.

[49] L. P. Gorḱov and G. Grüner. *Charge density waves in solids.* Elsevier, Amsterdam, 1989.

[50] Katsuaki Sugawara, Yuki Nakata, Ryota Shimizu, Patrick Han, Taro Hitosugi, Takafumi Sato, and Takashi Takahashi. Unconventional Charge-Density-Wave Transition in Monolayer 1T-$TiSe_2$. *ACS Nano*, 10(1):1341–1345, December 2015.

[51] Dongjing Lin, Shichao Li, Jinsheng Wen, Helmuth Berger, László Forró, Huibin Zhou, Shuang Jia, Takashi Taniguchi, Kenji Watanabe, Xiaoxiang Xi, and Mohammad Saeed Bahramy. Patterns and driving forces of dimensionality-dependent charge density waves in 2H-type transition metal dichalcogenides. *Nature Communications*, 11(1):2406, May 2020.

[52] Rodrigo A Fontenele, Sebastião dos Anjos Sousa Júnior, Tarik P Cysne, and Natanael C Costa. The impact of Rashba spin-orbit coupling in charge-ordered systems. *Journal of Physics: Condensed Matter*, 36(22):225601, mar 2024.

[53] Julián Faúndez, Rodrigo Alves Fontenele, Sebastião dos Anjos Sousa-Júnior, Fakher F. Assaad, and Natanael C. Costa. The two-dimensional Rashba-Holstein model. *arXiv:2411.07119*, 2024.

[54] D. Jaksch and P. Zoller. The cold atom Hubbard toolbox. *Ann. Phys.*, 315(1):52, 2005.

[55] T. Esslinger. Fermi-Hubbard physics with atoms in an optical lattice. *Annu. Rev. Condens. Matter Phys.*, 1(1):129–152, 2010.

[56] D. C. McKay and B. DeMarco. Cooling in strongly correlated optical lattices: prospects and challenges. *Rep. Prog. Phys.*, 74(5):054401, 2011.

[57] R. Jördens, L. Tarruell, D. Greif, T. Uehlinger, N. Strohmaier, H. Moritz, T. Esslinger, L. De Leo, C. Kollath, A. Georges, V. Scarola, L. Pollet, E. Burovski, E. Kozik, and M. Troyer. Quantitative determination of temperature in the ap-

proach to magnetic order of ultracold Fermions in an optical lattice. *Phys. Rev. Lett.*, 104:180401, May 2010.

[58] Florian Schäfer, Takeshi Fukuhara, Seiji Sugawa, Yosuke Takasu, and Yoshiro Takahashi. Tools for quantum simulation with ultracold atoms in optical lattices. *Nature Reviews Physics*, 2(8):411–425, Aug 2020.

[59] Yuji Nakagawa, Yuichi Kasahara, Takuya Nomoto, Ryotaro Arita, Tsutomu Nojima, and Yoshihiro Iwasa. Gate-controlled BCS-BEC crossover in a two-dimensional superconductor. *Science*, 372(6538):190–195, 2021.

[60] M. Keller, W. Metzner, and U. Schollwöck. Dynamical Mean-Field Theory for Pairing and Spin Gap in the Attractive Hubbard model. *Phys. Rev. Lett.*, 86:4612–4615, May 2001.

[61] M. Capone, C. Castellani, and M. Grilli. First-Order Pairing Transition and Single-Particle Spectral Function in the Attractive Hubbard Model. *Phys. Rev. Lett.*, 88:126403, Mar 2002.

[62] B. Kyung, A. Georges, and A.-M. S. Tremblay. Potential-energy-driven (BCS) to kinetic-energy-driven (BEC) pairing in the two-dimensional attractive Hubbard model: Cellular dynamical mean-field theory. *Phys. Rev. B*, 74:024501, Jul 2006.

[63] Robert Peters and Johannes Bauer. Local origin of the pseudogap in the attractive Hubbard model. *Phys. Rev. B*, 92:014511, Jul 2015.

[64] J. E Hirsch. Discrete Hubbard-Stratonovich transformation for fermion lattice models. *Phys. Rev. B*, 28(7):4059, 1983.

[65] J. E. Hirsch. Two-dimensional Hubbard model: Numerical simulation study. *Phys. Rev. B*, 31:4403–4419, Apr 1985.

[66] S. R. White, D. J. Scalapino, R. L. Sugar, E. Y. Loh, J. E. Gubernatis, and R. T. Scalettar. Numerical study of the two-dimensional Hubbard model. *Phys. Rev. B*, 40:506–516, Jul 1989.

[67] Raimundo R. dos Santos. Introduction to quantum Monte Carlo simulations for fermionic systems. *Braz. J. Phys.*, 33:36 – 54, 03 2003.

[68] A. Moreo and D. J. Scalapino. Two-dimensional negative-U Hubbard model. *Phys. Rev. Lett.*, 66:946–948, Feb 1991.

[69] J M Kosterlitz and D J Thouless. Ordering, metastability and phase transitions in two-dimensional systems. *J.Phys. C: Solid State Physics*, 6(7):1181–1203, apr 1973.

[70] B. Berche, A. I. Fariñas-Sanchez, and R. Paredes. Correlations in the low-temperature phase of the two-dimensional XY model. *Europhysics Letters (EPL)*, 60(4):539–545, nov 2002.

[71] D. J. Scalapino, S. R. White, and S. C. Zhang. Superfluid density and the Drude weight of the Hubbard model. *Phys. Rev. Lett.*, 68:2830–2833, May 1992.

[72] Douglas J. Scalapino, Steven R. White, and Shoucheng Zhang. Insulator, metal, or superconductor: The criteria. *Phys. Rev. B*, 47:7995–8007, Apr 1993.

[73] David R. Nelson and J. M. Kosterlitz. Universal jump in the superfluid density of two-dimensional superfluids. *Phys. Rev. Lett.*, 39:1201–1205, Nov 1977.

[74] P. J. H Denteneer, Guozhong An, and J. M. J. van Leeuwen. Optimal Superconducting Critical Temperature in the Two-Dimensional Attractive Hubbard Model. *Europhysics Letters (EPL)*, 16(1):5–10, sep 1991.

[75] P. J. H. Denteneer, Guozhong An, and J. M. J. van Leeuwen. Helicity modulus in the two-dimensional Hubbard model. *Phys. Rev. B*, 47:6256–6272, Mar 1993.

[76] P. J. H. Denteneer. Superfluid density in the two-dimensional attractive Hubbard model: Quantitative estimates. *Phys. Rev. B*, 49:6364–6367, Mar 1994.

[77] A. Toschi, M. Capone, and C. Castellani. Energetic balance of the superconducting transition across the BCS-Bose Einstein crossover in the attractive Hubbard model. *Phys. Rev. B*, 72:235118, Dec 2005.

[78] Sabyasachi Tarat and Pinaki Majumdar. A real space auxiliary field approach to the BCS-BEC crossover. *The European Physical Journal B*, 88(3):68, March 2015.

[79] A. Moreo, D. J. Scalapino, R. L. Sugar, S. R. White, and N. E. Bickers. Numerical study of the two-dimensional Hubbard model for various band fillings. *Phys. Rev. B*, 41:2313–2320, Feb 1990.

[80] Louis-Fran çois Arsenault, Patrick Sémon, and A.-M. S. Tremblay. Benchmark of a modified iterated perturbation theory approach on the fcc lattice at strong coupling. *Phys. Rev. B*, 86:085133, Aug 2012.

[81] K.-S. Chen, Z. Y. Meng, T. Pruschke, J. Moreno, and M. Jarrell. Lifshitz transition in the two-dimensional hubbard model. *Phys. Rev. B*, 86:165136, Oct 2012.

[82] Zi Hong Liu, Xiao Yan Xu, Yang Qi, Kai Sun, and Zi Yang Meng. Itinerant quantum critical point with frustration and a non-Fermi liquid. *Phys. Rev. B*, 98:045116, Jul 2018.

[83] Xiao Yan Xu, Zi Hong Liu, Gaopei Pan, Yang Qi, Kai Sun, and Zi Yang Meng. Revealing fermionic quantum criticality from new Monte Carlo techniques. *Journal of Physics: Condensed Matter*, 31(46):463001, aug 2019.

[84] N. D. Mermin and H. Wagner. Absence of Ferromagnetism or Antiferromagnetism in One- or Two-Dimensional Isotropic Heisenberg Models. *Phys. Rev. Lett.*, 17:1133–1136, Nov 1966.

[85] Yutan Zhang, Philip M. Dee, Benjamin Cohen-Stead, Thomas A. Maier, Steven Johnston, and Richard Scalettar. Optimizing the critical temperature and superfluid density of a metal-superconductor bilayer. *arXiv:2501.15428*, 2025.

[86] Yogeshwar Prasad, Amal Medhi, and Vijay B. Shenoy. Fermionic superfluid from a bilayer band insulator in an optical lattice. *Phys. Rev. A*, 89:043605, Apr 2014.

[87] Yogeshwar Prasad. Finite-temperature study of correlations in a bilayer band insulator. *Phys. Rev. B*, 106:184506, Nov 2022.

[88] Richard T. Scalettar, Joel W. Cannon, Douglas J. Scalapino, and Robert L. Sugar. Magnetic and pairing correlations in coupled Hubbard planes. *Phys. Rev. B*, 50:13419–13427, Nov 1994.

[89] Raimundo R. dos Santos. Magnetism and pairing in Hubbard bilayers. *Phys. Rev. B*, 51:15540–15546, Jun 1995.

[90] Qinpei Zheng, Yuqing Wang, Libo Liang, Qi Huang, Shuai Wang, Wei Xiong, Xiaoji Zhou, Wenlan Chen, Xuzong Chen, and Jiazhong Hu. Dimensional crossover of quantum critical dynamics in many-body phase transitions. *Phys. Rev. Res.*, 5:013136, Feb 2023.

[91] Maciej Lewenstein, Anna Sanpera, Veronica Ahufinger, Bogdan Damski, Aditi Sen(De), and Ujjwal Sen. Ultracold atomic gases in optical lattices: mimicking condensed matter physics and beyond. *Advances in Physics*, 56(2):243–379, 2007.

[92] W. Ketterle and M. W. Zwierlein. Making, probing and understanding ultracold Fermi gases. *La Rivista del Nuovo Cimento*, 31(5):247–422, May 2008.

[93] Michael Köhl, Henning Moritz, Thilo Stöferle, Kenneth Günter, and Tilman Esslinger. Fermionic atoms in a three dimensional optical lattice: Observing Fermi surfaces, dynamics, and interactions. *Phys. Rev. Lett.*, 94:080403, Mar 2005.

[94] Köhl, Michael and Esslinger, Tilman. Fermionic atoms in an optical lattice: a new synthetic material. *Europhysics News*, 37(2):18–21, 2006.

[95] Aslak Sindbjerg Poulsen and Thomas C Killian. Calibration of a 3d optical lattice, 2014.

[96] Leticia Tarruell and Laurent Sanchez-Palencia. Quantum simulation of the Hubbard model with ultracold fermions in optical lattices. *Comptes Rendus Physique*, 19(6):365–393, 2018. Quantum simulation / Simulation quantique.

[97] Eduardo Ibarra-García-Padilla, Rick Mukherjee, Randall G. Hulet, Kaden R. A. Hazzard, Thereza Paiva, and Richard T. Scalettar. Thermodynamics and magnetism in the two-dimensional to three-dimensional crossover of the Hubbard model. *Phys. Rev. A*, 102:033340, Sep 2020.

[98] Naoki Ogawa, Tatsuya Kaneko, and Yukinori Ohta. Dimensional crossover of the superfluid state in the attractive Hubbard model. *Journal of Physics: Conference Series*, 592(1):012103, mar 2015.

[99] R. Blankenbecler, D. J. Scalapino, and R. L. Sugar. Monte Carlo calculations of coupled boson-fermion systems. I. *Phys. Rev. D*, 24:2278–2286, Oct 1981.

[100] Ribhu K. Kaul. Spin nematics, valence-bond solids, and spin liquids in SO(n) quantum spin models on the triangular lattice. *Phys. Rev. Lett.*, 115:157202, Oct 2015.

[101] Toshihiro Sato, Fakher F. Assaad, and Tarun Grover. Quantum Monte Carlo Simulation of Frustrated Kondo Lattice Models. *Phys. Rev. Lett.*, 120:107201, Mar 2018.

[102] Andrew S. Darmawan, Yusuke Nomura, Youhei Yamaji, and Masatoshi Imada. Stripe and superconducting order competing in the Hubbard model on a square

lattice studied by a combined variational Monte Carlo and tensor network method. *Phys. Rev. B*, 98:205132, Nov 2018.

[103] Aleksander Zujev, Richard T Scalettar, George G Batrouni, and Pinaki Sengupta. Pairing correlations in the two-layer attractive Hubbard model. *New Journal of Physics*, 16(1):013004, jan 2014.

[104] Tamaghna Hazra, Nishchhal Verma, and Mohit Randeria. Bounds on the superconducting transition temperature: Applications to Twisted Bilayer Graphene and Cold Atoms. *Phys. Rev. X*, 9:031049, Sep 2019.

[105] Johannes S. Hofmann, Debanjan Chowdhury, Steven A. Kivelson, and Erez Berg. Heuristic bounds on superconductivity and how to exceed them. *npj Quantum Materials*, 7:83, Aug 2022.

[106] Tingting Shi, Wei Zhang, and C A R Sá de Melo. Tighter upper bounds on the critical temperature of two-dimensional superfluids and superconductors from the BCS to the Bose regime. *New J. Phys.*, 26:093001, Sep 2024.

[107] David A. Huse. Ground-state staggered magnetization of two-dimensional quantum heisenberg antiferromagnets. *Phys. Rev. B*, 37:2380–2382, Feb 1988.

[108] J. E. Hirsch and D. J. Scalapino. Enhanced superconductivity in quasi two-dimensional systems. *Phys. Rev. Lett.*, 56:2732–2735, Jun 1986.

[109] Raimundo R. dos Santos. Second-neighbor hopping in the attractive Hubbard model. *Phys. Rev. B*, 46:5496–5498, Sep 1992.

[110] Z. I. Djoufack, J. P. Nguenang, and A. Kenfack-Jiotsa. Next-next-nearest neighbor hopping effects on the MI and on the dynamics of breathers in 2D quantum ultracold atoms loaded in optical lattices. *The European Physical Journal Plus*, 140(2):161, Feb 2025.

[111] Oleg Derzhko, Johannes Richter, and Mykola Maksymenko. Strongly correlated flat-band systems: The route from heisenberg spins to hubbard electrons. *International Journal of Modern Physics B*, 29(12):1530007, 2015.

[112] Murad Tovmasyan, Sebastiano Peotta, Päivi Törmä, and Sebastian D. Huber. Effective theory and emergent SU(2) symmetry in the flat bands of attractive Hubbard models. *Phys. Rev. B*, 94:245149, Dec 2016.

[113] V R Shaginyan, A Z Msezane, V A Stephanovich, G S Japaridze, and E V Kirichenko. Flat bands and strongly correlated Fermi systems. *Physica Scripta*, 94(6):065801, apr 2019.

[114] Edwin W. Huang, Mohammad-Sadegh Vaezi, Zohar Nussinov, and Abolhassan Vaezi. Enhanced correlations and superconductivity in weakly interacting partially flat-band systems: A determinantal quantum Monte Carlo study. *Phys. Rev. B*, 99:235128, Jun 2019.

[115] Jin Yang, Liyu Liu, Jirayu Mongkolkiattichai, and Peter Schauss. Site-resolved imaging of ultracold fermions in a triangular-lattice quantum gas microscope. *PRX Quantum*, 2:020344, Jun 2021.

[116] H. Q. Lin and J. E. Hirsch. Two-dimensional Hubbard model with nearest- and next-nearest-neighbor hopping. *Phys. Rev. B*, 35:3359–3368, Mar 1987.

[117] B. Bucher, P. Steiner, J. Karpinski, E. Kaldis, and P. Wachter. Influence of the spin gap on the normal state transport in $YBa_2Cu_4O_8$. *Phys. Rev. Lett.*, 70:2012–2015, Mar 1993.

[118] T. Valla, A. V. Fedorov, Jinho Lee, J. C. Davis, and G. D. Gu. The ground state of the pseudogap in cuprate superconductors. *Science*, 314(5807):1914–1916, 2006.

[119] A. A. Kordyuk. Pseudogap from arpes experiment: Three gaps in cuprates and topological superconductivity (review article). *Low Temperature Physics*, 41(5):319–341, 05 2015.

[120] Mark Jarrell and J.E. Gubernatis. Bayesian inference and the analytic continuation of imaginary-time quantum Monte Carlo data. *Phys Rep.*, 269(3):133 – 195, 1996.

[121] J. M. Singer, T. Schneider, and P. F. Meier. Spectral properties of the attractive hubbard model. *The European Physical Journal B - Condensed Matter and Complex Systems*, 7(1):37–51, Jan 1999.

[122] Natanael C. Costa, Kazuhiro Seki, Seiji Yunoki, and Sandro Sorella. Phase diagram of the two-dimensional Hubbard-Holstein model. *Communications Physics*, 3(1):80, May 2020.

[123] E. Cappelluti, C. Grimaldi, and F. Marsiglio. Electron-phonon effects on spin-orbit split bands of two-dimensional systems. *Phys. Rev. B*, 76:085334, Aug 2007.

[124] Lucian Covaci and Mona Berciu. Polaron formation in the presence of Rashba Spin-Orbit Coupling: Implications for spintronics. *Phys. Rev. Lett.*, 102:186403, May 2009.

[125] Zhou Li, D. Baillie, C. Blois, and F. Marsiglio. Ground-state properties of the Holstein model near the adiabatic limit. *Phys. Rev. B*, 81:115114, Mar 2010.

[126] Zhou Li, L. Covaci, M. Berciu, D. Baillie, and F. Marsiglio. Impact of spin-orbit coupling on the Holstein polaron. *Phys. Rev. B*, 83:195104, May 2011.

[127] Igor Žutić, Jaroslav Fabian, and S. Das Sarma. Spintronics: Fundamentals and applications. *Rev. Mod. Phys.*, 76:323–410, Apr 2004.

[128] D. Pesin and L. Balents. Mott physics and band topology in materials with strong spin-orbit interaction. *Nature Physics*, 6(5):376–381, 2010.

[129] W. Witczak-Krempa, G. Chen, Y.B. Kim, and L. Balents. Correlated quantum phenomena in the strong spin-orbit regime. *Annual Review of Condensed Matter Physics*, 5(1):57–82, 2014.

[130] J.G. Rau, E.K.-H. Lee, and H.-Y. Kee. Spin-orbit physics giving rise to novel phases in correlated systems: Iridates and related materials. *Annual Review of Condensed Matter Physics*, 7:195–221, 2016.

[131] José A. Riera. Spin polarization in the Hubbard model with Rashba spin-orbit coupling on a ladder. *Phys. Rev. B*, 88:045102, Jul 2013.

[132] Manuel Laubach, Johannes Reuther, Ronny Thomale, and Stephan Rachel. Rashba spin-orbit coupling in the Kane-Mele-Hubbard model. *Phys. Rev. B*, 90:165136, Oct 2014.

[133] Fadi Sun, Jinwu Ye, and Wu-Ming Liu. Fermionic Hubbard model with Rashba or Dresselhaus spin–orbit coupling. *New Journal of Physics*, 19(6):063025, jun 2017.

[134] Welberth Kennedy, Sebastião dos Anjos Sousa-Júnior, Natanael C. Costa, and Raimundo R. dos Santos. Magnetism and metal-insulator transitions in the Rashba-Hubbard model. *Phys. Rev. B*, 106:165121, Oct 2022.

[135] Masataka Kawano and Chisa Hotta. Phase diagram of the square-lattice Hubbard model with Rashba-type antisymmetric spin-orbit coupling. *Phys. Rev. B*, 107:045123, Jan 2023.

[136] Jacob Beyer, Jonas B. Hauck, Lennart Klebl, Tilman Schwemmer, Dante M. Kennes, Ronny Thomale, Carsten Honerkamp, and Stephan Rachel. Rashba spin-orbit coupling in the square-lattice hubbard model: A truncated-unity functional renormalization group study. *Phys. Rev. B*, 107:125115, Mar 2023.

[137] Maria N. Gastiasoro, Maria Eleonora Temperini, Paolo Barone, and José Lorenzana. Generalized Rashba electron-phonon coupling and superconductivity in strontium titanate. *Phys. Rev. Res.*, 5:023177, Jun 2023.

[138] Y. Liu, D. F. Shao, L. J. Li, W. J. Lu, X. D. Zhu, P. Tong, R. C. Xiao, L. S. Ling, C. Y. Xi, L. Pi, H. F. Tian, H. X. Yang, J. Q. Li, W. H. Song, X. B. Zhu, and Y. P. Sun. Nature of charge density waves and superconductivity in $1T - TaSe_{2-x}Te_x$. *Phys. Rev. B*, 94:045131, Jul 2016.

[139] S. Manzeli, D. Ovchinnikov, D. Pasquier, O.V. Yazyev, and A. Kis. 2D transition metal dichalcogenides. *Nature Reviews Materials*, 2:17033, 2017.

[140] Wenjun Zhang, Quan Zhuang, Xiang-Long Yu, and Jiansheng Wu. The coexistence and competition of charge-density wave and superconductivity in the electron-doped H-MX2 (M = Mo, W and X=S, Se). *Surfaces and Interfaces*, 49:104391, 2024.

[141] Yizhi Ge and Amy Y. Liu. Effect of dimensionality and spin-orbit coupling on charge-density-wave transition in 2H-$TaSe_2$. *Phys. Rev. B*, 86:104101, Sep 2012.

[142] Chao-Sheng Lian, Christoph Heil, Xiaoyu Liu, Chen Si, Feliciano Giustino, and Wenhui Duan. Intrinsic and doping-enhanced superconductivity in monolayer $1H-TaS_2$: Critical role of charge ordering and spin-orbit coupling. *Phys. Rev. B*, 105:L180505, May 2022.

[143] R. Heid, K.-P. Bohnen, I. Yu. Sklyadneva, and E. V. Chulkov. Effect of spin-orbit coupling on the electron-phonon interaction of the superconductors Pb and Tl. *Phys. Rev. B*, 81:174527, May 2010.

[144] Paul C. Snijders and Hanno H. Weitering. Colloquium: Electronic instabilities in self-assembled atom wires. *Rev. Mod. Phys.*, 82:307–329, Feb 2010.

[145] Wujun Shi, Benjamin J Wieder, Holger L Meyerheim, Yan Sun, Yang Zhang, Yiwei Li, Lei Shen, Yanpeng Qi, Lexian Yang, Jagannath Jena, et al. A charge-density-wave topological semimetal. *Nature Physics*, 17(3):381–387, 2021.

[146] Yang Zhang, Ling-Fang Lin, Adriana Moreo, Shuai Dong, and Elbio Dagotto. First-principles study of the low-temperature charge density wave phase in the quasi-one-dimensional Weyl chiral compound $(TaSe_4)_2I$. *Phys. Rev. B*, 101:174106, May 2020.

[147] T Holstein. Studies of polaron motion. *Annals of Physics*, 8(3):325–342, November 1959.

[148] Shaozhi Li, E. A. Nowadnick, and S. Johnston. Quasiparticle properties of the nonlinear Holstein model at finite doping and temperature. *Phys. Rev. B*, 92:064301, Aug 2015.

[149] N. C. Costa, T. Blommel, W.-T. Chiu, G. Batrouni, and R. T. Scalettar. Phonon Dispersion and the Competition between Pairing and Charge Order. *Phys. Rev. Lett.*, 120:187003, May 2018.

[150] P. M. Dee, K. Nakatsukasa, Y. Wang, and S. Johnston. Temperature-filling phase diagram of the two-dimensional Holstein model in the thermodynamic limit by self-consistent Migdal approximation. *Phys. Rev. B*, 99:024514, Jan 2019.

[151] Y.-X. Zhang, W.-T. Chiu, N. C. Costa, G. G. Batrouni, and R. T. Scalettar. Charge Order in the Holstein Model on a Honeycomb Lattice. *Phys. Rev. Lett.*, 122:077602, Feb 2019.

[152] Chuang Chen, Xiao Yan Xu, Zi Yang Meng, and Martin Hohenadler. Charge-density-wave transitions of Dirac Fermions Coupled to Phonons. *Phys. Rev. Lett.*, 122:077601, Feb 2019.

[153] B. Cohen-Stead, N. C. Costa, E. Khatami, and R. T. Scalettar. Effect of strain on charge density wave order in the Holstein model. *Phys. Rev. B*, 100:045125, Jul 2019.

[154] Philip M. Dee, Jennifer Coulter, Kevin G. Kleiner, and Steven Johnston. Relative importance of nonlinear electron-phonon coupling and vertex corrections in the Holstein model. *Communications Physics*, 3(1):145, Aug 2020.

[155] Owen Bradley, George G. Batrouni, and Richard T. Scalettar. Superconductivity and charge density wave order in the two-dimensional Holstein model. *Phys. Rev. B*, 103:235104, Jun 2021.

[156] B. Xiao, N. C. Costa, E. Khatami, G. G. Batrouni, and R. T. Scalettar. Charge density wave and superconductivity in the disordered Holstein model. *Phys. Rev. B*, 103:L060501, Feb 2021.

[157] Natanael C. Costa, Kazuhiro Seki, and Sandro Sorella. Magnetism and Charge Order in the Honeycomb Lattice. *Phys. Rev. Lett.*, 126:107205, Mar 2021.

[158] Maykon V. Araújo, José P. de Lima, Sandro Sorella, and Natanael C. Costa. Two-dimensional $t - t^{'}$ Holstein model. *Phys. Rev. B*, 105:165103, Apr 2022.

[159] Manuel Weber and James K. Freericks. Real-time evolution of static electron-phonon models in time-dependent electric fields. *Phys. Rev. E*, 105:025301, Feb 2022.

[160] Sebastião dos Anjos Sousa-Júnior, Raimundo R. dos Santos, and Natanael C. Costa. Magnetic impurities in a charge-ordered background. *Phys. Rev. B*, 107:075140, Feb 2023.

[161] Xiangyu Zhang, Da Wang, and Congjun Wu. Quantum phonon dynamics induced spontaneous spin-orbit coupling. *arXiv:2410.16944*, 2024.

[162] Ho-Kin Tang, Xiaosen Yang, Jinhua Sun, and Hai-Qing Lin. Berezinskii-Kosterlitz-Thoules phase transition of spin-orbit coupled Fermi gas in optical lattice. *Europhysics Letters*, 107(4):40003, aug 2014.

[163] Peter Rosenberg, Hao Shi, and Shiwei Zhang. Ultracold Atoms in a Square Lattice with Spin-Orbit Coupling: Charge Order, Superfluidity, and Topological Signatures. *Phys. Rev. Lett.*, 119:265301, Dec 2017.

[164] Yu-Feng Song, Youjin Deng, and Yuan-Yao He. Nature of the mixed-parity pairing of attractive fermions with spin-orbit coupling in an optical lattice. *Phys. Rev. B*, 109:094504, Mar 2024.

[165] Paul Z. Hanakata, A. S. Rodin, Alexandra Carvalho, Harold S. Park, David K. Campbell, and A. H. Castro Neto. Two-dimensional square buckled Rashba lead chalcogenides. *Phys. Rev. B*, 96:161401, Oct 2017.

[166] Paul Z. Hanakata, A. S. Rodin, Harold S. Park, David K. Campbell, and A. H. Castro Neto. Strain-induced gauge and Rashba fields in ferroelectric Rashba lead chalcogenide PbX monolayers (X = S, Se, Te). *Phys. Rev. B*, 97:235312, Jun 2018.

[167] Junsaku Nitta, Tatsushi Akazaki, Hideaki Takayanagi, and Takatomo Enoki. Gate Control of Spin-Orbit Interaction in an Inverted $In_{0.53}Ga_{0.47}As/In_{0.52}Al_{0.48}As$ Heterostructure. *Phys. Rev. Lett.*, 78:1335–1338, Feb 1997.

[168] Christian R. Ast, Jürgen Henk, Arthur Ernst, Luca Moreschini, Mihaela C. Falub, Daniela Pacilé, Patrick Bruno, Klaus Kern, and Marco Grioni. Giant Spin Splitting through Surface Alloying. *Phys. Rev. Lett.*, 98:186807, May 2007.

[169] Eli Rotenberg, J. W. Chung, and S. D. Kevan. Spin-Orbit Coupling Induced Surface Band Splitting in Li/W(110) and Li/Mo(110). *Phys. Rev. Lett.*, 82:4066–4069, May 1999.

[170] S. LaShell, B. A. McDougall, and E. Jensen. Spin Splitting of an Au(111) Surface State Band Observed with Angle Resolved Photoelectron Spectroscopy. *Phys. Rev. Lett.*, 77:3419–3422, Oct 1996.

[171] Manuel Weber and Martin Hohenadler. Two-dimensional Holstein-Hubbard model: Critical temperature, Ising universality, and bipolaron liquid. *Phys. Rev. B*, 98:085405, Aug 2018.

[172] M. Hohenadler and G. G. Batrouni. Dominant charge density wave correlations in the Holstein model on the half-filled square lattice. *Phys. Rev. B*, 100:165114, Oct 2019.

[173] Eric Jeckelmann, Chunli Zhang, and Steven R. White. Metal-insulator transition in the one-dimensional Holstein model at half filling. *Phys. Rev. B*, 60:7950–7955, Sep 1999.

[174] Martin Hohenadler and Holger Fehske. Density waves in strongly correlated quantum chains. *The European Physical Journal B*, 91:1–14, 2018.

[175] E. Berger, P. Valášek, and W. von der Linden. Two-dimensional Hubbard-Holstein model. *Phys. Rev. B*, 52:4806–4814, Aug 1995.

[176] Katsunori Kubo. Weyl Semimetallic state in the Rashba–Hubbard model. *Journal of the Physical Society of Japan*, 93(2):024708, 2024.

[177] R. M. Noack, D. J. Scalapino, and R. T. Scalettar. Charge-density-wave and pairing susceptibilities in a two-dimensional electron-phonon model. *Phys. Rev. Lett.*, 66:778–781, Feb 1991.

[178] Chen Ning Yang and S. C. Zhang. SO(4) symmetry in a Hubbard model. *Modern Physics Letters B*, 04(11):759–766, 1990.

[179] Zhou Li, D. Baillie, C. Blois, and F. Marsiglio. Ground-state properties of the Holstein model near the adiabatic limit. *Phys. Rev. B*, 81:115114, Mar 2010.

[180] A. S. Alexandrov, V. V. Kabanov, and D. K. Ray. From electron to small polaron: An exact cluster solution. *Phys. Rev. B*, 49:9915–9923, Apr 1994.

[181] Nei Lopes, Daniel Reyes, Natanael C. Costa, Mucio A. Continentino, and Christopher Thomas. Incommensurate charge density wave in multiband intermetallic systems exhibiting competing orders. *Phys. Rev. B*, 107:205141, May 2023.

[182] Martin Hohenadler, Markus Aichhorn, and Wolfgang von der Linden. Spectral function of electron-phonon models by cluster perturbation theory. *Phys. Rev. B*, 68:184304, Nov 2003.

[183] D. Sénéchal, D. Perez, and M. Pioro-Ladrière. Spectral Weight of the Hubbard Model through Cluster Perturbation Theory. *Phys. Rev. Lett.*, 84:522–525, Jan 2000.

[184] David Sénéchal. An introduction to quantum cluster methods. *arXiv:0806.2690*, 2010.

[185] Xin Zhang, Wei Wu, Gang Li, Lin Wen, Qing Sun, and An-Chun Ji. Phase diagram of interacting Fermi gas in spin–orbit coupled square lattices. *New Journal of Physics*, 17(7):073036, jul 2015.

[186] Valentina Brosco and Massimo Capone. Rashba-metal to Mott-insulator transition. *Phys. Rev. B*, 101:235149, Jun 2020.

[187] Xuanlan Wang and Wei Zhu. Intertwined charge and spin orders through the exchange-interaction on a square lattice. *Physics Letters A*, 461:128652, 2023.

[188] Erik Wegner Hodt, Jabir Ali Ouassou, and Jacob Linder. Transient dynamics and quantum phase diagram for the square lattice Rashba-Hubbard model at arbitrary hole doping. *Phys. Rev. B*, 107:224427, Jun 2023.

[189] Andrzej Ptok, Karen Rodríguez, and Konrad Jerzy Kapcia. Superconducting monolayer deposited on substrate: Effects of the spin-orbit coupling induced by proximity effects. *Phys. Rev. Mater.*, 2:024801, Feb 2018.

[190] G. G. Batrouni and Richard T. Scalettar. Langevin simulations of a long-range electron-phonon model. *Phys. Rev. B*, 99:035114, Jan 2019.

[191] Thereza Paiva, R. T. Scalettar, W. Zheng, R. R. P. Singh, and J. Oitmaa. Ground-state and finite-temperature signatures of quantum phase transitions in the half-filled Hubbard model on a honeycomb lattice. *Phys. Rev. B*, 72:085123, Aug 2005.

[192] S. Sorella, Y. Otsuka, and S. Yunoki. Absence of a spin liquid phase in the Hubbard model on the Honeycomb lattice. *Sci Rep*, 2, Dec 2012.

[193] Fakher F. Assaad and Igor F. Herbut. Pinning the order: The nature of quantum criticality in the Hubbard model on Honeycomb Lattice. *Phys. Rev. X*, 3:031010, Aug 2013.

[194] Yuichi Otsuka, Seiji Yunoki, and Sandro Sorella. Universal quantum criticality in the metal-insulator transition of two-dimensional interacting Dirac electrons. *Phys. Rev. X*, 6:011029, Mar 2016.

[195] Francesco Parisen Toldin, Martin Hohenadler, Fakher F. Assaad, and Igor F. Herbut. Fermionic quantum criticality in honeycomb and π-flux Hubbard models: Finite-size scaling of renormalization-group-invariant observables from quantum Monte Carlo. *Phys. Rev. B*, 91:165108, Apr 2015.

[196] Jiajia Chen, Kai Wu, Wei Hu, and Jinlong Yang. Spin–Orbit Coupling in 2D Semiconductors: A Theoretical Perspective. *The Journal of Physical Chemistry Letters*, 12(51):12256–12268, December 2021.

[197] Igor F. Herbut, Vladimir Juričić, and Oskar Vafek. Relativistic Mott criticality in graphene. *Phys. Rev. B*, 80:075432, Aug 2009.

[198] Emilie Huffman and Shailesh Chandrasekharan. Fermion-bag inspired Hamiltonian lattice field theory for fermionic quantum criticality. *Phys. Rev. D*, 101:074501, Apr 2020.

[199] . A.l. fetter and j.d. walecka: Quantum theory of many-particle systems, McGraw-Hill Book Co., New York, 1971, 601, 15×23cm, 7,800. 1971.

[200] Zi-Xiang Li, Yi-Fan Jiang, and Hong Yao. Majorana-time-reversal symmetries: A Fundamental Principle for Sign-Problem-Free Quantum Monte Carlo Simulations. *Phys. Rev. Lett.*, 117:267002, Dec 2016.

[201] E. Y. Loh, J. E. Gubernatis, R. T. Scalettar, S. R. White, D. J. Scalapino, and R. L. Sugar. Sign problem in the numerical simulation of many-electron systems. *Phys. Rev. B*, 41:9301–9307, May 1990.

[202] Matthias Troyer and Uwe-Jens Wiese. Computational Complexity and Fundamental Limitations to Fermionic Quantum Monte Carlo Simulations. *Phys. Rev. Lett.*, 94:170201, May 2005.

[203] Nandini Trivedi and Mohit Randeria. Deviations from Fermi-Liquid Behavior above T_c in 2D Short Coherence Length Superconductors. *Phys. Rev. Lett.*, 75:312–315, Jul 1995.

[204] M. E. Fisher. Critical Phenomena. In M. S. Green, editor, *Proceedings of the Enrico Fermi International School of Physics*, volume 51. Academic Press, New York, 1971.

[205] R. R. dos Santos and L. Sneddon. Finite-size rescaling transformations. *Phys. Rev. B*, 23:3541–3546, Apr 1981.

[206] M. N. Barber. Finite-size scaling. In Cyril Domb and Joel L. Lebowitz, editors, *Phase Transitions and Critical Phenomena*, volume 8, page 145. Academic Press, New York, 1983.

[207] David Sénéchal, Danny Perez, and Dany Plouffe. Cluster perturbation theory for Hubbard models. *Phys. Rev. B*, 66:075129, Aug 2002.